University of California, Merced

Ph.D. Dissertation

Modeling diffuse reflectance measurements of light scattered by layered tissues

A dissertation submitted
in partial fulfillment of the requirements for the degree

Doctor of Philosophy in Applied Mathematics

by

Shelley B. Rohde

Committee in charge:
Professor Arnold D. Kim, Chair
Professor Boaz Ilan
Professor Roummel Marcia

2014

University of California, Merced
Graduate Division

This is to certify that I have examined a copy of a dissertation by

Shelley B. Rohde

and found it satisfactory in all respects, and that any and all revisions required by the examining committee have been made. It is approved, and it is acceptable in quality and form for publication on microfilm and electronically:

Boaz Ilan

Roummel Marcia

Arnold D. Kim (Chair)

University of California, Merced
2014

Contents

List of Figures

List of Tables

List of Symbols

Symbol	Units	Description
I	$W/(\mathrm{m}^2)$	radiance/intensity
μ_s	1/mm	scattering coefficient
μ_a	1/mm	absorption coefficient
ℓ_s	mm	mean scattering length
ℓ_a	mm	characteristic absorption length
g		anisotropy factor
μ_s'	1/mm	reduced scattering coefficient
θ	degrees or radians	angle with respect to z-axis
φ	degrees or radians	azimuthal angle
μ		cosine of θ
$\hat{\mathbf{s}}$		unit vector denoting direction of propagation, $\langle \cos\varphi \sin\theta, \sin\varphi \sin\theta, \cos\theta \rangle$
$\mathbf{r}$	mm	position vector $\langle x, y, z \rangle$
w	mm	beam width
α		nondimensional small parameter
β		nondimensional small parameter
κ	mm	diffusion coefficient
$r(\mu)$		Fresnel reflection coefficient
$t(\mu)$		Fresnel transmission coefficient
Δx	mm	spatial shift

Acknowledgements

First and foremost, I would like to thank my advisor, Arnold D. Kim. He has been a supportive and encouraging mentor, and his influence was crucial in the completion of this work. I am extremely grateful, and indebted to him for all these years of guidance and support.

I would also like to thank my committee members Boaz Ilan and Roummel Marcia for all of their support and guidance in my graduate career. My thanks to Michael Sprague for his guidance and encouragement in my early years at UCM, and François Blanchette for his guidance and feedback in my early teaching years. I am appreciative of Mayya Tokman for being an inspirational teacher and mentor in my early years at UCM. I am grateful for the support of Arnold Kim, Boaz Ilan, Orkan Umurhan, and Karin Leiderman in obtaining a faculty position at an undergraduate university. I am also grateful to Suzanne Sindi, Lei, Yue, Anne Zanzucchi, and Harish Bhat for their helpful discussions during that process. My thanks to the wonderful staff members Carrie King, Katherine Brown, and Tammy Johnson for their support. I would also like to acknowledge Julia Clark, Stephen Minter, Korana Burke, Nitesh Kumar, Haik Stepanian, and Jane Hyojin Lee for their engaging discussions and mutual support in graduate school. Finally, I am grateful to have a loving and supportive husband and family who always encouraged me.

In Chapters 2, 3, and 4 we acknowledge use of the Virtual Photonics software resources in the Laser Microbeam and Medical Program (LAMMP), a NIH National Biomedical Technology Resource, NIH-P41-RR01192. I would like to thank Carole Hayakawa, Lisa Malenfant, Janaka Ranasinghesagara, David Cuccia, Adam Gardner, and Vasan Venugopalan for their assistance in using the Virtual Tissue Simulator software.

The work in Chapter 2 was supported by the National Science Foundation (NSF), grant $\#DMS-0806039$. The work in Chapter 2 was published in Journal of the Optical Society of America A, and is rewritten here as consistent with their author posting policy. The work in Chapter 3 was published in Optics Letters, and is rewritten here as consistent with their author posting policy. The coauthor listed in both publications directed and supervised research which forms the basis of this dissertation.

Curriculum Vitae

Shelley B. Rohde

School of Natural Sciences
University of California, Merced
Merced, CA 95343

srohde@ucmerced.edu
http://www.shelleyrohde.com

Teaching Interests

Calculus, Differential Equations, Numerical Analysis, Mathematical Modeling, and Linear Algebra

Research Interests

Light propagation in biological tissues, numerical analysis, differential equations, asymptotic and perturbation analysis, biomedical optics, and photonics

Education

University of California, Merced
PhD Candidate in Applied Mathematics
Dissertation Title: Modeling diffuse reflectance measurements of light scattered by layered tissues
Expected PhD: May 2014
Advisor: Arnold D. Kim

B.S. 2007 in Applied Mathematics
California State University, Chico
Minors in Physics and Theatre
Awards: Dean's List, Graduated with Honors in General Education

---

Academic Honors During Graduate Studies

Dean's Distinguished Fellowship January 2014 - May 2014
SREB-State Doctoral Scholars AGEP Scholar at the 20th Annual Institute on Teaching and Mentoring (2013)
Graduate Research Assistant May 2013 - August 2013, May 2011-January 2012, August 2009-January 2011, and December 2008-June 2009
GRC Graduate Student Summer Research Fellowship (2012)
Spring 2012 Graduate Division General Fellowship
Certificate of Achievement in Research and Teaching (2012)
Sacramento Graduate Advocacy Day Student Representative (2012)

Teaching Experience

Lead Instructor

Vector Calculus January 2012 - May 2012

Teaching Fellow, Advanced Teaching Assistant

Calculus II August 2013 - December 2013

Partial Differential Equations January 2013 - May 2013

Vector Calculus August 2012 - December 2012, additional duties: held one lecture

Vector Calculus January 2011 - May 2011

Teaching Assistant

Numerical Analysis II January 2010 - May 2010, additional duties: held 3 lectures

Numerical Analysis I August 2009 - December 2009

Calculus II June 2009 - August 2009

Introductory Physics II for Biological Sciences January 2009 - May 2009

Numerical Analysis I August 2008 - December 2008

Calculus I June 2008 - August 2008, additional duties: prepared all discussion worksheets and quizzes

Vector Calculus January 2008 - May 2008

Differential Equations and Linear Algebra August 2007 - December 2007

Assistant Facilitator, Teaching Assistant

Physics course in B A STAR program June 2007 - August 2007

Training

Completed one year of Teaching Assistant training coursework

Attended workshops for continuing professional development

Research Experience

Doctoral Research: Applied Mathematics Unit, University of California, Merced
Advisor: Arnold D. Kim, 2007-Present

Modeling diffuse reflectance measurements due to near infrared light propagation in biological tissues

Undergraduate Research: Department of Mathematics and Statistics, California State University, Chico
Advisor: Thomas McCready, 2006-2007

Fluid dynamics and viscous fluid flow

Undergraduate Research: Department of Physics, California State University, Chico
Advisor: Eric Ayars, 2006-2007

Experimental work studying phonons with a designed lattice structure

Undergraduate Research: Department of Mathematics and Statistics, California State University, Chico
Advisor: Thomas Mattman, 2004

Summer REU on knot theory

Publications

S. B. Rohde and A. D. Kim, "Modeling the diffuse reflectance due to a narrow beam incident on a turbid medium," J. Opt. Soc. Am. A **29**, 231-238 (2012).

S. B. Rohde and A. D. Kim, "A convolution model of the diffuse reflectance for layered tissues," Opt. Lett. **39**, 154-157 (2014).

Presentations

Invited Talks

1. March 15, 2013. *The Corrected Diffusion Approximation* at California State University, Chico. A presentation of my research for the Physics faculty and students.
2. May 29, 2012. *Corrected Diffusion Approximation in Layered Tissues* in Portland, OR for the Optics Group held jointly by OHSU and Portland State University. A presentation of my current research.
3. September 30, 2011. *Modeling Light Propagation in Tissue* at California State University, Chico. A presentation of my research for the Mathematics faculty and students.
4. November 5, 2010. *Modeling Light Propagation in Tissue* at California State University, Chico. A presentation of my research for the Physics faculty and students.
5. March 31, 2010. *Foundations for using the Radiative Transport Equation to scan tissue for early-stage cancer cells* at University of California, Merced for the SAMPLe Seminar Series.
6. November 10, 2009. *Applied Mathematics Graduate Studies* at California State University, Chico. A presentation about our faculty and Applied Mathematics graduate program for the Mathematics faculty and students. I also sat on a panel with other graduate students to discuss my experience as a graduate student at UC Merced.
7. November 2005. *Dancing Mathematics* at California State University, Chico. A fun presentation about math and dance for the faculty and students interested in mathematics.

Contributed Talks

1. May 20, 2012. *Corrected Diffusion Approximation in Layered Tissues* at SIAM Imaging Science conference in Philadelphia, PA.

Poster Presentations

1. May 1, 2012. *Corrected Diffusion Approximation in Layered Tissues* at OSA BIOMED conference in Miami, FL.

Conferences and Workshops

Joint Mathematics Meetings, January 2014
20th Annual Institute on Teaching and Mentoring, October-November 2013
SIAM Imaging Science Conference, May 2012
OSA BIOMED Conference, May 2012
Sacramento Graduate Advocacy Day, March 2012
Virtual Photonics Workshop, August 2011
CBST Retreat, July 2011
Virtual Photonice Workshop, September 2010
MSRI introductory workshop on inverse problems, August 2010
Women in Physics Conference, January 2007

Professional Activities and Memberships

Student Membership:

Society of Industrial and Applied Mathematics (SIAM), Optical Society of America (OSA), Association for Women in Mathematics (AWM), and Women in Science and Engineering (WiSE)

Committees:

Graduate student representative on selection committee for new dean of the School of Natural Sciences at UC Merced (2011), and undergraduate representative on selection committee for the "book in common" for the incoming freshmen at CSU, Chico (2006).

Founding president of UCM WiSE chapter (2010)
Board member for CSU, Chico Math Club (2005 - 2007)
Tutored privately for college and high school students (2004 - 2007)

ABSTRACT OF THE DISSERTATION

Modeling diffuse reflectance measurements of light scattered by layered tissues

by

Shelley B. Rohde

Doctor of Philosophy in Applied Mathematics

University of California, Merced, 2014

Prof. Arnold D. Kim, Chair

Abstract

In this dissertation, we first present a model for the diffuse reflectance due to a continuous beam incident normally on a half space composed of a uniform scattering and absorbing medium. This model is the result of an asymptotic analysis of the radiative transport equation for strong scattering, weak absorption and a defined beam width. Through comparison with the diffuse reflectance computed using the numerical solution of the radiative transport equation, we show that this diffuse reflectance model gives results that are accurate for small source-detector separation distances.

We then present an explicit model for the diffuse reflectance due to a collimated beam of light incident normally on layered tissues. This model is derived using the corrected diffusion approximation applied to a layered medium, and it takes the form of a convolution with an explicit kernel and the incident beam profile. This model corrects the standard diffusion approximation over all source-detector separation distances provided the beam is sufficiently wide compared to the scattering mean-free path. We validate this model through comparison with Monte Carlo simulations. Then we use this model to estimate the optical properties of an epithelial layer from Monte Carlo simulation data. Using measurements at small source-detector separations and this model, we are able to estimate the absorption coefficient, scattering coefficient and anisotropy factor of epithelial tissues efficiently with reasonable accuracy.

Finally, we present an extension of the corrected diffusion approximation for an obliquely incident beam. This model is formed through a Fourier Series representation in the azimuthal angle which allows us to exhibit the break in axisymmetry when combined with the previous analysis. We validate this model with Monte Carlo simulations. This model can also be written in the form of a convolution of an explicit kernel with the incident beam profile. Additionally, it can be used to improve computation of the optical properties.

Chapter 1

Introduction

Cancer is an ever-present disease all over the world. It seems that every person knows of someone who has battled, or is battling cancer. Of course, this is purely anecdotal - but the sentiment has propelled numerous researchers to work toward a solution. In my work, we study light propagation in tissues to improve detection of early stage cancer cells. In the following section, I will outline some of the data regarding cancer cases in the United States and the biology of cancer. I then expand upon the study of light propagation in tissues, and discuss many works which lead to the analysis discussed in this dissertation.

In Chapter 2, I outline our work deriving the corrected diffusion approximation (CDA) as presented in [52]. This is an approximation derived systematically from the radiative transport equation (RTE) as a diffusion approximation plus a boundary layer solution. It is defined by a scaling with the beam width through asymptotic analysis of a perturbation solution using small parameter defined by the length scales in the problem. The diffusion approximation is slightly modified from the standard diffusion approximation, and the boundary layer solution is determined through the solution of a one dimensional RTE. In Chapter 3, I expand upon the analysis done in Chapter 2 to a layered tissue system, and rewrite the reflectance in the form of a convolution of an explicit kernel and the incident beam profile. This expands upon the work in [53]. In Chapter 4, I extend the analysis in Chapter 3 to compute reflectance due to an obliquely incident beam. By applying an obliquely incident beam we are able to compare reflectance with respect to the angle of the incident beam and determine the epithelial optical properties.

1.1 Cancer biology and detection

In 2013 there were an estimated 580,350 deaths due to cancer in the United States [58]. More startling is the estimated number of new cancer cases, which was over 1.6 million for 2013 [58]. Cancer is the general term used for a malignant tumor [10], which is typically denoted by an abnormal mass of tissue composed of altered cells. Of these cases, approximately 80% of the deaths and over 85% of the new incidence cases in 2013 were due to carcinomas.

1.1.1 Carcinomas

Carcinomas are specified as cancer which originates in the epithelial cells lining organs [10]. Epithelial cells form the protective lining of organs, typically the superficial tissue layer. Epithelial tissues are frequently exposed to environmental factors, which are known to impact cancer formation [10]. For example, our skin is exposed to UV rays, the digestive lining is exposed to various consumables, our lungs are exposed to air irritants, etc. Thus, it is intuitive that these linings are more likely to undergo cell changes during division.

Cells in the human body are regularly dividing to maintain healthy tissues, as older cells die to maintain a healthy cell population [10]. Cancerous cells essentially stop following the rules to maintain healthy tissues. Cancer in epithelial tissue forms in three main stages. During the first stage, hyperplasia, the cells undergo rapid division and increase their total number in an area. This is primarily due to changes that do not induce and/or allow for normal cell death (apoptosis). In the second stage, dysplasia, the cells begin to genetically mutate. This leads to abnormal growth and/or changes in the cell structure. At this stage the cells change enough that the optical properties of the tissue will change markedly. Third, carcinoma *in situ*, is a premalignant condition in which the cells continue to grow and change to form a mass, but have not grown beyond the tissue in which they currently reside. This is depicted in Figure 1.1.

Once the cancer spreads beyond the original tissue, it becomes malignant and is known as an invasive carcinoma. Once the cancer reaches blood supply it metastasizes [10]. Metastatic cancer is significantly harder to treat, and decreases the chances

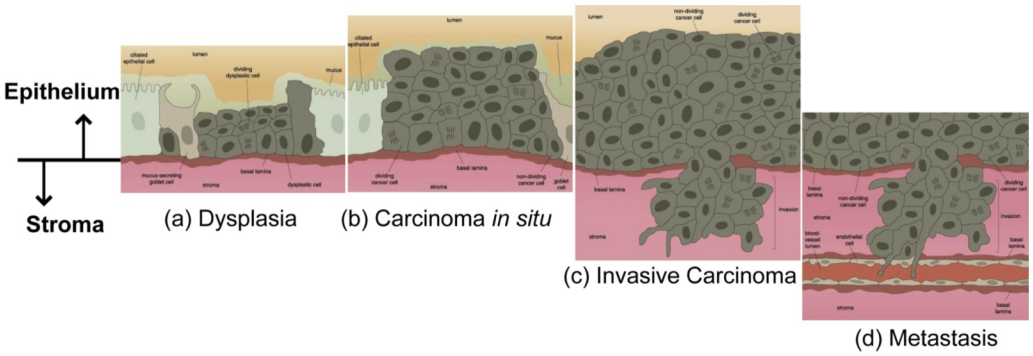

Figure 1.1: Image from article on Metastasis *Van Noorden et al. American Scientist 86(2), (1998)* [47], depicting stages of cancer formation in the epithelial layer.

of patient survival. The changes in cell structure during stages two and three provide an opportunity to locate the abnormality before it metastasizes. However, Carcinoma *in situ* may exhibit these characteristics and is not considered cancerous, nor malignant. The distinction arises in the agressiveness of these cells. Carcinoma *in situ* does not leave the tissue of origin, while a cancerous invasive carcinoma will invade nearby tissue. This aspect of carcinomas, missing the distinction between tissues, can complicate treatment immensely. When a carcinoma is removed, much of the surrounding healthy tissue is also removed to prevent any undetectable invasion of cancerous cells

from growing in the remaining healthy tissue [10]. Thus, a conundrum arises because we know the tissue is cancerous once it spreads, but it is significantly harder to treat after it spreads. This is why better imaging to improve early detection is important.

1.1.2 Detection

Due to the prevalence of cases and death rates due to these cancers, early detection is key to patient survival. Many imaging techniques are used today to screen for cancer. Computed Tomography (CT), Magnetic Resonance Imaging (MRI), x-ray, nuclear scan, and ultrasound are some of the most common imaging options [57]. Additionally, for some areas of the body there are endoscopy options, which is essentially imaging inside the body. CT and MRI can construct 3 dimensional images of the area of concern, and the images are more detailed than other options. However, CT and MRI require very large machines, and the scans are expensive for the patient. MRI and Nuclear Scans have the ability to determine some additional properties of the tissue (MRI uses information about the polarization of the hydrogen atoms, and Nuclear Scans provide information about the absorption of the radiative material inserted into the area of concern). X-ray, CT, and Nuclear Scans all expose the patients to ionizing radiation, which is known to cause tissue damage. X-ray and Ultrasound are relatively inexpensive, but the image quality is not as detailed when compared to other options available. Endoscopy uses a tube comprised of a camera with a light, and typically presents a visual exam of the inside of the body. The downside to this technology is that it is invasive and merely a visual representation, thus in order to detect cancer it must be large enough to be seen by the eye.

Some newer techniques are Diffuse Optical Tomography (DOT) and Diffuse Optical Spectroscopy (DOS). DOT is a medical imaging technique which illuminates tissue with near-infrared light, and uses measurements of scattered light by the tissue boundary to determine the optical properties (scattering and absorption coefficients) of the tissue [4]. DOS uses the near-infrared backscattered light to determine chemical properties based on changes in the backscattered data with changes in wavelength of the light source [4]. Near-infrared light is used because it has a better penetration depth when used for tissue than those with shorter or longer wavelengths (in and near the visual range). It has also been shown that water, oxygenated hemoglobin, and deoxygenated hemoglobin are some of the most absorptive components of biological tissue, but in near-infrared light they all have relatively weak absorption. This allows for the data to include information about the construction of the tissue at centimeter depths [4]. This is extremely useful in tissue because the epithelial layers are generally less than 0.5mm deep.

DOT and DOS systems have the potential to be a safe, portable, and affordable option for patients [4]. CT, X-ray, and Nuclear Scans all expose the patient to ionizing radiation, whereas DOT and DOS use near-infrared light which is non-ionizing radiation, and not linked to tissue damage. CT and MRI require large and expensive machines, but near-infrared light is relatively cheap and easy to produce [4]. This allows for small, inexpensive machines which will increase availability for screening in places that current methods may not be practical or possible. For example, combining DOT/DOS with endoscopy is a viable option for improving endoscopy results. DOT/DOS systems have potential to be very affordable for patients, which would allow for more frequent testing. There is also potential for use in a variety of situations ranging from ambulances

to bedside monitoring [4]. These benefits give DOT and DOS the potential to be very useful additions to the current imaging techniques.

Most cancer is currently diagnosed by a visual inspection of the surface, or one of the listed imaging techniques, and followed by taking a sample of the tissue (biopsy) for further inspection (histology). Since many of the current imaging techniques require the use of large machines (CT and MRI especially), this can be inconvenient for the patient and the doctor, and is not easy nor efficient if it needs to be repeated. DOT and DOS would not replace current imaging techniques, but would allow for an efficient way to check on progress and/or determine if a biopsy is necessary, with less reliance on these larger machines. This is especially useful because DOT/DOS should be relatively easy and affordable to repeat when necessary, allowing for better assessment of progress. We will focus on DOT, because it is the method for which we intend the work in this dissertation to apply.

In order to understand the diagnostic information determined by DOT measurements, it is important to discuss the optical properties of tissue. There have been a number of studies determining the optical properties of tissue, and experimental methods using tissue phantoms designed to model biological tissues, scatterers, and absorbers. Cheong *et al* [8] published a review of determined optical properties for a range of human and animal tissues. Since that publication, Hornung *et al.* [22] determined optical properties and physiological properties of cervical tissue for normal and dysplastic cervical tissues. Later, Collier *et al.* [9] studied the optical properties of epithelial tissue using confocal microscopy. They compiled a table of values for cervical, uterine, breast, lung, and skin epithelial tissues which can be used as reference. Cerussi *et al.* studied malignant breast tumors physiological properties, and optical properties. They found a significant increase in the absorption of tumor tissue compared to normal tissue in the near-infrared range. Kortun *et al.* [42] studied the optical properties of layered tissues and presented values for epithelium and stroma. Recently, Jacques [24] presented data sets and developed a model of the optical properties of tissue with respect to wavelength and variable amounts of absorbing chromophores. The compilation of these publications allowed us to study relevant values for tissue optical properties.

1.2 Diffuse reflectance by biological tissues

In DOT, diffuse reflectance measurements are taken at the boundary to study the properties of tissue [68]. The diffuse reflectance is a non-invasive measurement of scattered light which provides diagnostic information about the absorption and scattering properties of tissues, see the visual representation in Figure 1.2. These optical properties, in turn, provide valuable insight into tissue health. Imaging and spectroscopy modalities based on diffuse reflectance measurements have been applied to a broad variety of tissue systems (see the review in [75]). Modeling the diffuse reflectance is critical for interpreting measurements and extracting information contained in them. To be useful practically, models for the diffuse reflectance need to be accurate over a broad range of spatial, temporal and frequency scales to investigate adequately the scattering medium. Moreover, they need to be intuitive and easy to implement.

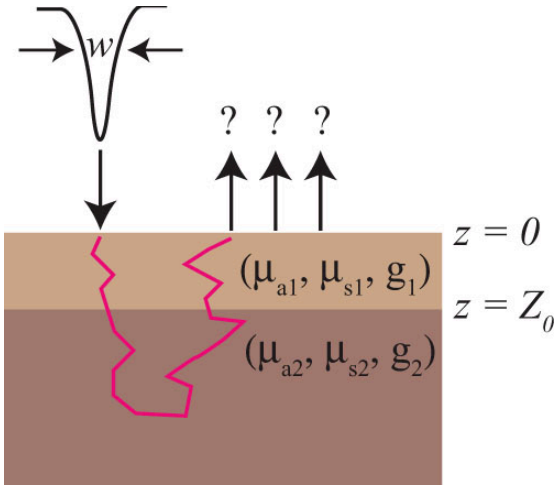

Figure 1.2: This is a depiction of the physical system with a normally incident Gaussian beam on a two-layer tissue system. In this image, the top layer represents the thin epithelial layer while the lower layer represents a semi-infinite half space as the stromal tissue layer. The optical properties are shown where μ_{a1} and μ_{a2} are the absorption coefficients of the respective layers, μ_{s1} and μ_{s2} are the scattering coefficients of the respective layers, g_1 and g_2 are the anisotropy factors of the respective layers, Z_0 is the thickness of the top layer, and w is the width of the Gaussian beam.

1.2.1 Modeling Light Propagation in Tissues

To implement techniques of DOT, we must model light propagation in tissues. Light is modeled as electromagnetic radiation, and thus is ultimately governed by Maxwell's equations. For applications in biological tissues, it is important to understand the length scales considered [62]. Maxwell's equations are used for microscopic light scattering problems. Although Maxwell's equations provide a rigorous model for electromagnetic wave propagation, they are also extremely computationally expensive. This restricts the problems which are feasible to solve using Maxwell's equations. Essentially, this is for problems of similar size to the wavelength of light used which restricts the problems to individual cells. For example, if the wavelegth used is 900nm, and the typical cell size is 10μm [10], then a single cell is orders of magnitude larger than the wavelength of light. Considering most tumors detected are closer to 10^9 cells total [10], approximating the mass of cells using Maxwell's equations is prohibitive.

The radiative transport equation (RTE) provides a model for light propagation as the transport of particles [23]. The RTE is derived from Maxwell's Equations for cases when particles are in the far-field region of each other, and there are no correlations between particle position [51]. The far-field region is the region outside the near-field region, in which the angular field distribution is essentially independent of distance from the source. The RTE models problems in the mesoscopic scale [62], which is defined in terms of the scattering mean free path. We define the scattering mean free path through the scattering coefficient of the medium, $\ell_s = 1/\mu_s$ [23, 68]. The scattering coefficient of a medium is defined by the probability of photon scattering per unit path length [68]. In biological tissue, the size of ℓ_s is similar to 100μm [68], which is more similar to the size of the tumor listed earlier. Thus, since the goal is to detect tumors earlier - and thus smaller - than before, the RTE models light propagation for the appropriate scale of problem. There are two styles of solving for diffuse reflectance measurements using the RTE typically, discrete ordinates and Monte Carlo simulations. Discrete ordinates solves the RTE numerically and is described in [23, 6]. However, solving the RTE using discrete ordinates is still computationally expensive, and thus impractical for normal application. Monte Carlo simulations use the governing equation and model the photon propagation stochastically [68]. Monte Carlo simulations are used widely for experimental verification of other models, but due to their format are not invertible and thus are imperfect when attempting to determine optical properties from reflectance measurements. There has been work to improve the computation of optical properties from matched Monte Carlo data [76, 27, 46]. However, Monte Carlo simulations are also computationally expensive which coupled with their invertibility limits their application.

The RTE is very computationally expensive for larger, macroscopic cases [62]. The diffusion approximation (DA) is an approximation to the RTE for a high-albedo scattering medium which assumes near-isotropic scattering after sufficient scatters, and is composed of an expansion in Legendre Polynomials [68, 71]. The result is a simpler model, which provides reasonable accuracy for deeper tissues. However, due to the assumptions it is not valid close to the boundary, or light source. The DA is commonly used due to its form, as it is much easier to solve and provides an easily invertible form to determine the optical properties of tissues for DOT applications. Unfortunately, for detection of early stage cancer cells in the epithelial layer of organs the DA cannot be used because it is invalid so close to the boundary.

It is also important to study layered tissue systems; many biological organs are

composed of a thin epithelial layer above a thick stroma. These layers are composed of different cell structures and thus have different optical properties. We model layered tissues as a two-layer system composed of a thin, top layer representing the epithelium above a semi-infinite half space representing the stroma, as in Figure 1.2. This same system was used by Kienle *et al.* [30] with the DA. Also, there is a correlation between measurements of the diffuse reflectance at small source-detector separation distances and the optical properties of superficial tissues [30, 1, 60]. Thus, in order to determine the optical properties of epithelial tissues we must form an accurate model of reflectance data close to the source.

The diffusion equation is much simpler to solve than the radiative transport equation. Consequently, models of the diffuse reflectance using the DA have found widespread use for many practical problems. Some examples are Groenhius *et al.* [19], who compared reflectance measurements using the DA and Monte Carlo simulations to determine an appropriate range of optical properties which are valid for the DA. Kienle *et al.* [26] provided a method of collecting spatially dependent reflectance measurements to determine optical properties using the DA and Monte Carlo simulations. Farrell and Patterson [13], use a photon dipole source to solve for reflectance measurements using the DA while satisfying the tissue boundary conditions. Kienle and Patterson [29] applied improved solutions using multiple boundary condition variations to improve upon reflectance calculation for the DA. Kienle and Patterson [28] also investigated the errors of frequency domain reflectance calculations by the DA close to the source. Kienle *et al.* [30] developed a two layer model using the DA and the extrapolated boundary condition to approximate the reflectance and compared with Monte Carlo simulations. Kienle *et al.* [3] studied the angular dependence of the detector in measurements used to determine optical properties for cylindrical and spherical scatterers using the DA. Schmitt *et al.* [54] developed a multilayer model for skin (epidermis, dermis, and subcutaneous tissues) to approximate the reflectance using the DA. Yoon *et al.* [72] examined the accuracy of the DA compared with the discrete ordinates method outlined in [61]. Franceschini *et al.* [14] studied the effect of the superficial layer on the optical properties computed using the DA.

Using the DA to model the diffuse reflectance leads to substantial errors at small source-detector separation distances [19, 29, 28]. This lack of accuracy becomes prohibitive when one seeks to investigate the optical properties of superficial tissue regions. Thus, many approaches have attempted to improve upon the reflectance calculations by the DA. One of the most frequently used is the $\delta - P_1$ approximation which comes from an approximation to the scattering phase function introduced by Joseph *et al.* [25]. Carp *et al.* [5] developed analytic solutions for both planar and Gaussian beam irradiation of a homogeneous semi-infinite half space using the $\delta - P_1$ approximation. Hayakawa *et al.* [20] introduced a method to recover optical properties using $\delta - P_1$ with an increased range of optical properties using spatially resolved data. You *et al.* [73] developed a $\delta - P_1$ approximation used in the frequency domain and compared with the standard DA and Monte Carlo simulations. Seo *et al.* [55] developed an analytical solution for the spatially resolved diffuse reflectance using the $\delta - P_1$ approximation, and used it to determine optical properties of tissue phantoms. Additionally, Venugopalan *et al.* [63] introduced a generalized diffusion model which allowed for smaller source detector separation, and extended the range of scattering albedo accessible.

Other techniques have also been applied to improve upon the range of the DA. For example, Wang and Jacques [65] applied a hybrid model that combines Monte Carlo

simulations for distances near the source with the DA at large distances from the source. Later, Wang [67] extended this for an infinitely narrow beam. Tarvainen *et al.* [59] use a finite element method that couples the RTE with the DA. Vitkin *et al.* [64] introduced a phase function corrected diffusion approximation in which the phase function is decomposed into delta-isotropic phase function and a relatively smooth remainder. Heino *et al.* [21] developed an anisotropic diffusion model which allows efficient calculation of simple anisotropic scattering cases. However, these cannot provide the same accuracy and efficacy of the RTE.

1.3 Mathematical analysis and challenges

The RTE and the DA are established models for modeling light propagation in tissue. However, the RTE is too computationally expensive and the diffusion approximation is invalid for studying epithelial tissues. Thus, we seek a solution which combines the accuracy and validity of the RTE with the efficiency of the DA for modeling reflectance measurements and determining optical properties.

1.3.1 Radiative Transport

The RTE is given by

$$\mu\partial_z I + \sqrt{1-\mu^2}\,(\cos\varphi\partial_x I + \sin\varphi\partial_y I) + \mu_a I + \mu_s(I - \int_{\mathbb{S}^2} p(\hat{\mathbf{s}}\cdot\hat{\mathbf{s}}')I(\hat{\mathbf{s}}',\mathbf{r})d\hat{\mathbf{s}}') = 0. \quad (1.1)$$

In this integro-partial-differential equation, $\mathbf{r}$ is the position vector $\langle x, y, z\rangle$, $\hat{\mathbf{s}}$ is the direction of propagation determined by $\mu = \cos\theta$ where θ is defined in spherical coordinates as the angle with respect to z, and φ is the azimuthal angle. I is the radiance, μ_a is the absorption coefficient of the medium, μ_s is the scattering coefficient of the medium, and $p(\hat{\mathbf{s}}\cdot\hat{\mathbf{s}}')$ is the scattering phase function of the medium which defines the anisotropy factor, g. Computing the solution to the RTE has been a formidable problem approached by many to determine an effective and efficient model. Elaloufi *et al.* [12] solved for intensity using a discrete ordinates method due to a collimated beam in a multilayer tissue slab. Dunn and Boas [11] computed solutions using the first Born approximation to the RTE. Prahl *et al.* [49] computed reflectance and transmission data using the adding-doubling method [69], and the one dimensional RTE. Chang and Ishimaru [7] presented a numerical solution to the RTE in the spatial frequency domain. Asadzadeh [2] derived the Fokker-Planck operator, which is used for forward peaked scattering to approximate the scattering operator. A. D. Kim [32] solved the RTE using discrete ordinates and the Fokker-Planck scattering operator for biological tissues. González-Rodríquez and A. D. Kim [18] used discrete ordinates to solve the RTE and then reconstructed the interior to detect absorber in the epithelial layer using the first Born approximation. A. D. Kim and Moscoso [39] solved the RTE in a two layer tissue structure developing an equivalent slab form which studies the epithelial layer. They previously computed three dimensional solutions for narrow optical beams [36] using Chebyshev spectal methods which were compared with Monte Carlo simulations. Kim and Moscoso also solved the RTE numerically with multiple scattering operators to compare their effectiveness [38]. Additionally, they solved the RTE using the Fokker-Planck approximation to define a backscattered ring formed by forward-peaked scattering me-

dia [37]. A. D. Kim and Keller [35] solved the RTE numerically for the reflectance and transmission of a slab using multiple scattering operators to compare their effectiveness. González-Rodríguez and A. D. Kim [16] developed the Fokker-Planck-Eddington and generalized Fokker-Planck-Eddington scattering operator approximations to solve problems with both forward-peaked and large angle scattering with the RTE. They also compared a number of methods solving the RTE to find the best to use for reconstruction of absorption and scattering properties of tissues [17]. A. D. Kim and Schotland [40] studied a nonhomogeneous absorption coefficient problem solving for an analytic expression of the specific intensity due to single and multiple absorbers. A. D. Kim *et al.* [34] recovered optical properties of the top layer of a two-layer tissue sample using the Born approximation of the RTE.

One of the mechanisms that can be solved using RTE which the DA cannot account for directly is oblique incidence. RTE maintains the angular dependence of the source term and scattering, while the DA reduces the radiance to a function solely based on position due to the assumption of isotropic scattering. There has been work to study obliquely incident beams due to the additional degree of freedom which could be used to determine optical properties at specific depths. Wang and Jacques [66] developed a modification to diffusion to approximate the change in reflectance due to an oblique incident beam. This was represented by a spatial shift which was used by later authors to determine optical properties with an obliquely incident beam [44, 45]. Kim *et al.* [41] studied the physiological properties of rats and tissue models using Mie theory with angular and spectral measurements. Zemp [74] introduced a phase function corrected diffusion model for applying the obliquely incident beam. Gardner *et al.* [15] developed a RTE solution for an obliquely incident beam applying a spherical harmonics expansion. Solving the oblique incidence problem lends well to improving detection by using information from the break in axisymmetry.

1.3.2 The Corrected Diffusion Approximation

The corrected diffusion approximation (CDA) is the basis of this dissertation. We developed CDA in an effort to bridge the gap in efficiency and accuracy between the RTE and the DA models. Yielding a result which maintains spatial and angular dependence of the radiance, while simplifying the computational requirements of the full RTE. This method was originally derived by A. D. Kim in [33], and has been extended in [52, 53, 43]. Ideally, this method will be used experimentally to improve recovery of optical properties of epithelial tissues due to its improved accuracy and explicit form.

The CDA is formed as the sum of an interior solution, Φ, and a boundary layer solution, Ψ derived systematically from the RTE. The interior solution is derived using the same scaling assumptions as in the diffusion approximation, and results in a diffusion equation. The boundary layer solution "corrects" the interior solution at the boundary and is asymptotically matched to ensure consistency. The RTE is an integro-partial-differential equation with 5 degrees of freedom, and after the following analysis the CDA is an elliptic partial differential equation with a Robin boundary condition added with a 1-D RTE. Additionally, the CDA of reflectance measurements can be written in the form of a convolution of an explicit kernel and the incident beam profile. Thus, CDA is computationally efficient and invertible. In this dissertation we will use the convolution form of CDA to determine optical properties using data from Monte Carlo simulations to validate its efficacy.

Chapter 2

Corrected Diffusion Approximation

The corrected diffusion approximation (CDA) was formulated to study diffuse reflectance measurements close to the source with an efficient and accurate method. It is composed of a diffusion approximation which is denoted as the interior solution and a boundary layer solution, both of which are derived systematically from the radiative transport equation (RTE). Results shown here are published in [52].

2.1 Formulation of the Problem

The RTE is given by

$$\mu\partial_z I + \sqrt{1-\mu^2}(\cos\varphi\partial_x I + \sin\varphi\partial_y I) + \mu_a I + \mu_s L I = 0, \quad \text{in } z > 0. \tag{2.1}$$

It is given in terms of specific intensity $I = I(\mu, \varphi, x, y, z)$ and represents the intensity flowing in direction $\hat{\mathbf{s}} = \hat{\mathbf{s}}(\mu, \varphi)$ at position $\mathbf{r} = \langle x, y, z\rangle$. Here, $\mu = \cos\theta$, φ is the azimuthal angle, μ_a is the absorption coefficient of the medium, μ_s is the scattering coefficient of the medium, and L is the operator:

$$LI = I - \iint_{S^2} p(\hat{\mathbf{s}}\cdot\hat{\mathbf{s}}')I(\hat{\mathbf{s}}', \mathbf{r})d\hat{\mathbf{s}}'. \tag{2.2}$$

We assume scattering is spherically symmetric, such that $p(\hat{\mathbf{s}}\cdot\hat{\mathbf{s}}') = p(\mu, \mu', \varphi - \varphi')$. Thus, we rewrite (2.2) as

$$LI = I - \int_{-\pi}^{\pi}\int_{-1}^{1} p(\mu, \mu', \varphi - \varphi')I(\mu', \varphi', x, y, z)d\mu' d\varphi'. \tag{2.3}$$

Here, p is the scattering phase function of the medium. In this work, we use the Henyey-Greenstein scattering phase function [50]. Due to the spherical symmetry of the scattering phase function, we know that for an isotropic vector $\vec{A}$

$$\iint_{S^2} p(\hat{\mathbf{s}}\cdot\hat{\mathbf{s}}')\hat{\mathbf{s}}'\cdot\vec{A}d\hat{\mathbf{s}}' = g\hat{\mathbf{s}}\cdot\vec{A}. \tag{2.4}$$

Thus, $L[\hat{\mathbf{s}}'\cdot\vec{A}] = (1-g)\hat{\mathbf{s}}'\cdot\vec{A}$.

We solve (2.1) subject to the boundary condition

$$I(\mu,\varphi,x,y,0) - r(\mu)I(-\mu,\varphi,x,y,0) = \frac{\delta(\mu-1)}{2\pi} f(x,y). \tag{2.5}$$

Where $r(\mu)$ is the Fresnel reflection coefficient for the relative refractive index of the medium, and $f(x,y)$ is the beam profile incident on the half space. Here, we set f to a Gaussian beam,

$$f(x,y) = \frac{F_0}{2\pi w^2} \exp\left(-\frac{(x^2+y^2)}{2w^2}\right). \tag{2.6}$$

Thus, there is a natural scaling in the incident beam with our spatial variables x and y, and the beam width w. We can rewrite (2.6) as

$$\bar{f}\left(\frac{x}{w},\frac{y}{w}\right) = \frac{F_0}{2\pi} \exp\left(-\frac{1}{2}\left(\left(\frac{x}{w}\right)^2 + \left(\frac{y}{w}\right)^2\right)\right) \tag{2.7}$$

We rescale $\mathbf{r}$ with respect to w, according to $\vec{r} = w\vec{\bar{r}}$.

If we substitute this scaling with respect to w into (2.1) and (2.5), we obtain the resulting non-dimensionalized equation

$$\frac{\mu}{w}\partial_{\bar{z}}\bar{I} + \frac{1}{w}\sqrt{1-\mu^2}(\cos\varphi\partial_{\bar{x}}\bar{I} + \sin\varphi\partial_{\bar{y}}\bar{I}) + \mu_a\bar{I} + \mu_s L\bar{I} = 0, \tag{2.8}$$

with the boundary condition

$$\bar{I}(\mu,\varphi,\bar{x},\bar{y},0) - r(\mu)\bar{I}(-\mu,\varphi,\bar{x},\bar{y},0) = \frac{\delta(\mu-1)}{2\pi}\bar{f}(\bar{x},\bar{y}). \tag{2.9}$$

These equations define the scaling for our analysis. We use the assumption for modeling tissues that is also used in diffusion, $\mu_s \gg \mu_a$. If we divide (2.8) by μ_s we have two nondimensional parameters that are known to be small, given the beam width is sufficiently sized. We define the first to be $\alpha = \mu_a/\mu_s$, for the absorption parameter, and the second to be $\beta = 1/(w\mu_s)$, for the beam width parameter. We require both parameters be small, $\alpha, \beta \ll 1$, and for tissues we know $\alpha \ll \beta$ generally.

We now study the nondimensionalized problem

$$\beta\mu\partial_{\bar{z}}\bar{I} + \beta\sqrt{1-\mu^2}(\cos\varphi\partial_{\bar{x}}\bar{I} + \sin\varphi\partial_{\bar{y}}\bar{I}) + \alpha\bar{I} + L\bar{I} = 0, \tag{2.10}$$

with the boundary condition (2.9). To solve this problem, we seek the asymptotic solution of (2.10) as $\alpha, \beta \to 0^+$. Note that this is a singular perturbation problem, as there is small parameter β as a coefficient before the derivatives in $\bar{x}$, $\bar{y}$, and $\bar{z}$.

2.2 Derivation of Interior Solution

We write the solution of (2.10) and (2.9) as the sum of an interior solution, Φ, and a boundary layer solution, Ψ, such that $\bar{I} = \Phi + \Psi$. We solve for Φ by seeking a perturbation solution of the form $\sum_{n=0}^{\infty}\beta^n\phi_n$ as $\beta \to 0^+$. Upon substituting this form into (2.10), and collecting like-powers of β, we obtain to the $O(1)$ that

$$L\phi_0 = 0. \tag{2.11}$$

This equation is an eigenvalue problem where ϕ_0 is an eigenfunction of L with eigenvalue 0. For this equation to hold, ϕ_0 must have no dependence on $\hat{\mathbf{s}}$. Thus, we write $\phi_0 = \phi_0(\mathbf{r})$. To $O(\beta)$ we obtain

$$L\phi_1 = -\mu\partial_{\bar{z}}\phi_0 - \sqrt{1-\mu^2}(\cos\varphi\partial_{\bar{x}}\phi_0 + \sin\varphi\partial_{\bar{y}}\phi_0). \tag{2.12}$$

Here, we can define ϕ_1 in terms of ϕ_0 due to our knowledge of the operator L. Given property (2.4), and that $\nabla\phi_0$ is an isotropic vector, we seek a solution for ϕ_1 in the form $\phi_1 = C\hat{\mathbf{s}}\cdot\nabla\phi_0$. Substituting this ansatz into (2.12) yields

$$(1-g)C\hat{\mathbf{s}}\cdot\nabla\phi_0 = -\hat{\mathbf{s}}\cdot\nabla\phi_0. \tag{2.13}$$

Thus, $C = -1/(1-g)$ and $\phi_1 = -1/(1-g)\hat{\mathbf{s}}\cdot\nabla\phi_0$. To $O(\beta^2)$, we obtain

$$L\phi_2 = \hat{\mathbf{s}}\cdot\nabla(\hat{\mathbf{s}}\cdot 3\kappa\nabla\phi_0) - \frac{\alpha}{\beta^2}\phi_0, \quad \kappa = 1/[3(1-g)]. \tag{2.14}$$

For (2.14) to have a solution, we must apply the solvability condition

$$\iint_{S^2}[\hat{\mathbf{s}}\cdot\nabla(\hat{\mathbf{s}}\cdot 3\kappa\nabla\phi_0) - \frac{\alpha}{\beta^2}\phi_0]d\hat{\mathbf{s}} = 0. \tag{2.15}$$

Consequently, we find that ϕ_0 satisfies the diffusion equation

$$\nabla\cdot(\kappa\nabla\phi_0) - \frac{\alpha}{\beta^2}\phi_0 = 0. \tag{2.16}$$

With the terms ϕ_0 and ϕ_1 determined, we have

$$\Phi = \phi_0 - \frac{1}{(1-g)}\hat{\mathbf{s}}\cdot\nabla\phi_0 + O(\beta^2) + O(\alpha). \tag{2.17}$$

2.3 Derivation of Boundary Layer Solution

To compute the boundary layer solution we introduce stretched variable $\bar{z} = \beta\zeta$, and let $\bar{\Psi}(\mu,\varphi,\bar{x},\bar{y},\zeta) = \Psi(\mu,\varphi,\bar{x},\bar{y},\beta\zeta)$. With this scaling $\bar{\Psi}$ satisfies

$$\mu\partial_\zeta\bar{\Psi} + \beta\sqrt{1-\mu^2}(\cos\varphi\partial_{\bar{x}}\bar{\Psi} + \sin\varphi\partial_{\bar{y}}\bar{\Psi}) + \alpha\bar{\Psi} + L\bar{\Psi} = 0. \tag{2.18}$$

We seek a solution of the form $\sum_{n=0}^{\infty}\beta^n\psi_n$ as $\beta\to 0^+$. Substituting this expansion into (2.18), and collecting like-powers of β yields the following to $O(1)$:

$$\mu\partial_\zeta\psi_0 + L\psi_0 = 0. \tag{2.19}$$

To $O(\beta)$, we obtain

$$\mu\partial_\zeta\psi_1 + L\psi_1 = -\sqrt{1-\mu^2}(\cos\varphi\partial_{\bar{x}}\psi_0 + \sin\varphi\partial_{\bar{y}}\psi_0). \tag{2.20}$$

Substituting the asymptotic expansions into boundary condition (2.9), we find to $O(1)$ that

$$\psi_0 - r(\mu)\psi_0 = \frac{\delta(\mu-1)}{2\pi}\bar{f}(\bar{x},\bar{y}) - [1-r(\mu)]\phi_0(\bar{x},\bar{y},0), \quad \text{on } 0<\mu\le 1, \tag{2.21}$$

and to $O(\beta)$ that

$$\psi_1 - r(\mu)\psi_1 = 3\kappa[1+r(\mu)]\mu\partial_{\bar{z}}\phi_0(\bar{x},\bar{y},0)$$
$$-3\kappa[1-r(\mu)]\sqrt{1-\mu^2}(\cos\varphi\partial_{\bar{x}}\phi_0(\bar{x},\bar{y},0)+\sin\varphi\partial_{\bar{y}}\phi_0(\bar{x},\bar{y},0)), \quad \text{on } 0<\mu\leq 1. \quad (2.22)$$

Additionally, we impose that $\bar{\Psi}\to 0$ as $\zeta\to\infty$ to ensure asymptotic matching between the boundary layer solution and the interior solution. We ensure this asymptotic matching using Green's function in the same manner described in [31, 33]. Details of this analysis are outlined in Appendices A and B. Because the beam is incident normally on the boundary $z=0$, we may apply the analysis used to compute boundary conditions for the corrected diffusion approximation (see [33], Section 2B]). The result of this analysis leads to boundary conditions for the interior solution and the boundary layer solution. We do not redo this analysis here. Rather, we summarize the results of this analysis applied to this particular problem below.

2.4 Boundary Conditions

To compute the boundary layer solution, we must ensure it satisfies boundary conditions (2.21) and (2.22). However, these conditions require knowledge of our interior solution at the boundary. We first determine boundary conditions for ϕ_0. Note that a constant solves (2.19). All other solutions vanish as $\zeta\to\infty$. To ensure the asymptotic matching condition is satisfied, we must set the constant solution to zero. Let us define the operator P

$$P[s(\mu)] = \int_0^1 [U_1(\mu') + \sum_{k>0} c_{1k}V_k(\mu')]s(\mu')\mu' d\mu'. \quad (2.23)$$

This operator maps boundary data, $s(\mu)$, to the constant solution. It is given in terms of plane wave solutions discussed in Appendix A. Note that P is related to the half space Green's function given in (B.18), but only the slowest decaying plane wave solution is retained. We determine a boundary condition for ϕ_0 by integrating (2.21) and (2.22) with respect to φ and then applying P to that result which yields

$$\frac{1}{2\pi}P[\delta(\mu-1)]\bar{f}(\bar{x},\bar{y}) - P[1-r(\mu)]\phi_0(\bar{x},\bar{y},0) + 3\beta\kappa P[\mu+\mu r(\mu)]\partial_{\bar{z}}\phi_0(\bar{x},\bar{y},0) = 0. \quad (2.24)$$

Consequently, ϕ_0 satisfies the Robin condition

$$a\phi_0(\bar{x},\bar{y},0) - b\partial_{\bar{z}}\phi_0(\bar{x},\bar{y},0) = c\bar{f}(\bar{x},\bar{y}), \quad (2.25)$$

with

$$a = P[1-r(\mu)], \quad (2.26)$$

$$b = 3\beta\kappa P[\mu+\mu r(\mu)], \quad (2.27)$$

$$c = \frac{1}{2\pi}P[\delta(\mu-1)]. \quad (2.28)$$

2.5 Computation of Diffuse Reflectance Measurements

We use the half space Green's function given in (B.18) to compute the boundary layer solution according to

$$\psi_n(\mu,\zeta) = \int_0^\infty \int_{-1}^1 G^H(\mu,\zeta;\mu',\zeta')Q(\mu',\zeta')d\mu' d\zeta' + \int_0^1 G^H(\mu,\zeta;\mu',0)s(\mu')\mu' d\mu'. \quad (2.29)$$

In (2.29), $Q(\mu,\zeta)$ is the interior source term, and $s(\mu)$ is the boundary source term. Thus, we find that

$$\psi_0(\mu,\zeta) = \int_0^1 G^H(\mu,\zeta;\mu',0)\left[\frac{\delta(\mu'-1)}{2\pi}\bar{f}(\bar{x},\bar{y}) - [1-r(\mu')]\phi_0(\bar{x},\bar{y},0)\right]\mu' d\mu'. \quad (2.30)$$

We are ultimately computing reflectance, which is determined through an integral over the full range of φ.

$$R(x,y) = -\int_{-\pi}^{\pi}\int_{-1}^{-\mu_{NA}} t(\mu)\bar{I}(\mu,\varphi,\bar{x},\bar{y},0)\mu d\mu d\varphi, \quad (2.31)$$

where $t(\mu)$ is the Fresnel transmission coefficient due to the refractive index mismatch at $z=0$, and $-\mu_{NA}$ is determined by the numerical aperture of the detector used. Due to the symmetry of $-\pi \le \varphi \le \pi$, source terms containing $\cos\varphi$ and $\sin\varphi$ will vanish in this computation of reflectance. Thus, we find that

$$\psi_1(\mu,\zeta) = \int_0^1 G^H(\mu,\zeta;\mu',0)[3\kappa[1+r(\mu')]\mu'\partial_{\bar{z}}\phi_0(\bar{x},\bar{y},0)\mu' d\mu'. \quad (2.32)$$

To complete the analysis of these integrals we must compute the interior solution.

Fourier transforming (2.16) and (2.25), we obtain

$$-\xi^2\hat{\phi}_0 - \eta^2\hat{\phi}_0 + \partial_{\bar{z}}^2\hat{\phi}_0 - \frac{\alpha}{\kappa\beta^2}\hat{\phi}_0 = 0, \quad (2.33)$$

and

$$a\hat{\phi}_0 - b\partial_{\bar{z}}\hat{\phi}_0 = cF(\xi,\eta), \quad (2.34)$$

respectively. In this we define the Fourier transform as

$$F(\xi,\eta) = \frac{1}{(2\pi)^2}\iint \bar{f}(\bar{x},\bar{y})e^{-i\xi\bar{x}-i\eta\bar{y}}d\bar{x}d\bar{y}. \quad (2.35)$$

The solution of (2.33) subject to (2.34) is

$$\phi_0(\bar{x},\bar{y},\bar{z}) = \iint \frac{cF(\xi,\eta)}{a+b\gamma}e^{-\gamma\bar{z}+i\xi\bar{x}+i\eta\bar{y}}d\xi d\eta. \quad (2.36)$$

Consequently,

$$\partial_{\bar{z}}\phi_0(\bar{x},\bar{y},\bar{z}) = \iint \frac{-\gamma cF(\xi,\eta)}{a+b\gamma}e^{-\gamma\bar{z}+i\xi\bar{x}+i\eta\bar{y}}d\xi d\eta. \quad (2.37)$$

In (2.36) and (2.37),

$$\gamma = \sqrt{\frac{\alpha}{\kappa\beta^2} + \xi^2 + \eta^2}, \tag{2.38}$$

which is found by solving (2.33) for the decay rate in $\bar{z}$ associated with the derivative.

We solve for Ψ using the Green's function relations in (2.30) and (2.32) of the form

$$\Psi(\mu, \bar{x}, \bar{y}, \zeta) = H_a(\mu, \zeta)\bar{f}(\bar{x}, \bar{y}) - H_b(\mu, \zeta)\phi_0(\bar{x}, \bar{y}, \bar{z}) + H_c(\mu, \zeta)3\beta\kappa\partial_{\bar{z}}\phi_0(\bar{x}, \bar{y}, \bar{z}). \tag{2.39}$$

We simplify to solve for H_a, H_b, and H_c

$$H_a(\mu, \zeta) = \frac{1}{2\pi}G^H(\mu, \zeta; 1, 0), \tag{2.40}$$

$$H_b(\mu, \zeta) = \int_0^1 G^H(\mu, \zeta; \mu', 0)[1 - r(\mu')]\mu' d\mu', \tag{2.41}$$

$$H_c(\mu, \zeta) = \int_0^1 G^H(\mu, \zeta; \mu', 0)[\mu' + r(\mu')]\mu' d\mu'. \tag{2.42}$$

Therefore, the radiance $I = \Phi + \Psi$ at $\bar{z} = 0$ is given by

$$\bar{I}(\mu, \bar{x}, \bar{y}, 0) = H_a(\mu, 0)\bar{f}(\bar{x}, \bar{y}) + [1 - H_b(\mu, 0)]\phi_0(\bar{x}, \bar{y}, 0) - 3\beta\kappa[\mu - H_c(\mu, 0)]\partial_{\bar{z}}\phi_0(\bar{x}, \bar{y}, 0) + O(\beta^2) + O(\alpha). \tag{2.43}$$

Substituting (2.43) into (2.31), we obtain

$$R(\bar{x}, \bar{y}) = R_a\bar{f}(\bar{x}, \bar{y}) + R_b\phi_0(\bar{x}, \bar{y}, 0) - R_c\partial_{\bar{z}}\phi_0(\bar{x}, \bar{y}, 0) + O(\beta^2) + O(\alpha). \tag{2.44}$$

The constants R_a, R_b, and R_c are given by

$$R_a = -2\pi \int_{-1}^{-\mu_{NA}} t(\mu)H_a(\mu, 0)\mu d\mu, \tag{2.45}$$

$$R_b = -2\pi \int_{-1}^{-\mu_{NA}} t(\mu)[1 - H_b(\mu, 0)]\mu d\mu, \tag{2.46}$$

$$R_c = -2\pi(3\beta\kappa) \int_{-1}^{-\mu_{NA}} t(\mu)[\mu - H_c(\mu, 0)]\mu d\mu. \tag{2.47}$$

In the next section we compare this model of the diffuse reflectance given in (2.44) to that computed using the full numerical solution of the radiative transport equation. The full numerical solution is computed using plane wave modes for the full radiative transport equation. The beam profile used in this comparison is

$$\bar{f}(\bar{x}, \bar{y}) = \frac{F_0}{2\pi} \exp\left(-\frac{1}{2}(\bar{x}^2 + \bar{y}^2)\right), \tag{2.48}$$

with F_0 denoting the incident flux.

2.6 Numerical Results and Comparisons

To compute the solution of radiative transport equation, we use the numerical method described in [38]. This method involves computing plane wave solutions of the radiative transport equation in the spatial frequency domain and then inverting that result into the physical domain using a quasi fast Hankel transform [56]. This method has been shown to agree with Monte Carlo simulations as well as the Chebyshev spectral method [36].

For the numerical solution of the radiative transport equation, we have replaced the scattering operator defined in (2.2) by the generalized Fokker-Planck-Eddington scattering operator [16]. This scattering operator requires far less angular resolution for numerical computations than (2.2). Moreover, this scattering operator has been shown to agree well with the radiative transport equation for sharply peaked forward scattering.

A comparison of results computed using Monte Carlo simulations and this numerical method appears in Fig. 2.1. The results from the Monte Carlo simulations are plotted as circle symbols. The results from the numerical method described above are plotted as a solid curve. For the results shown in Fig. 2.1, the optical properties are $\mu_s = 100\,\mathrm{mm}^{-1}$, $\mu_a = 0.01\,\mathrm{mm}^{-1}$, and $g = 0.8$. The ratio of the refractive index inside the half space over that outside of the half space is $n_{\mathrm{rel}} = 1.4$. The beam width is $w = 0.4247\,\mathrm{mm}$. We have set $\mu_{\mathrm{NA}} = 0$ so that the detectors collect the light over all directions exiting the medium. For the Monte Carlo result, we have used the single Monte Carlo approach using non-uniform rational B-splines [46] available at http://www.virtualphotonics.org. In particular, we used 10^6 photons to obtain the Monte Carlo result shown in Fig. 2.1.

Figure 2.1 shows excellent agreement between the two methods. We observe differences in the results only for small source-detector separation distances. This discrepancy may be due to an inadequate number of photons used for the Monte Carlo simulations or due to errors inherent in the generalized Fokker-Planck-Eddington scattering operator. Nonetheless, we find that this agreement is satisfactory and so we use this numerical method for evaluating the accuracy of the asymptotic model in the results below. One feature of the quasi fast Hankel transform is that it is computed over a logarithmic grid in the radial distance variable $\rho = \sqrt{x^2 + y^2}$. Consequently, we are able to evaluate the diffuse reflectance model over a large range of source-detector distances using this method.

In the results discussed below, we compare the diffuse reflectances computed using this numerical method, the asymptotic model given in (2.44) and the standard diffusion approximation. We use the same logarithmic grid to compute the quasi fast Hankel transform for all three of these models. In doing so, we are able to investigate the accuracy of the diffuse reflectance models over a large range of source-detector separation distances.

In Fig. 2.2, we show results for $\mu_s = 500\,\mathrm{mm}^{-1}$, $\mu_a = 0.01\,\mathrm{mm}^{-1}$ and $w = 0.5\,\mathrm{mm}$ so that $\alpha = 2 \times 10^{-5}$ and $\beta = 4 \times 10^{-3}$. We have set $g = 0.8$ and the ratio of the refractive index inside the medium to outside the medium to be $n_{\mathrm{rel}} = 1.4$. We have set $\mu_{\mathrm{NA}} = 0$ so that the detectors collect the light over all directions exiting the medium. For the asymptotic model, we have used also the generalized Fokker-Planck-Eddington scattering operator. We use this comparison as an indicator for the validity of the model given very highly scattering media. With these parameter values, the constants in the

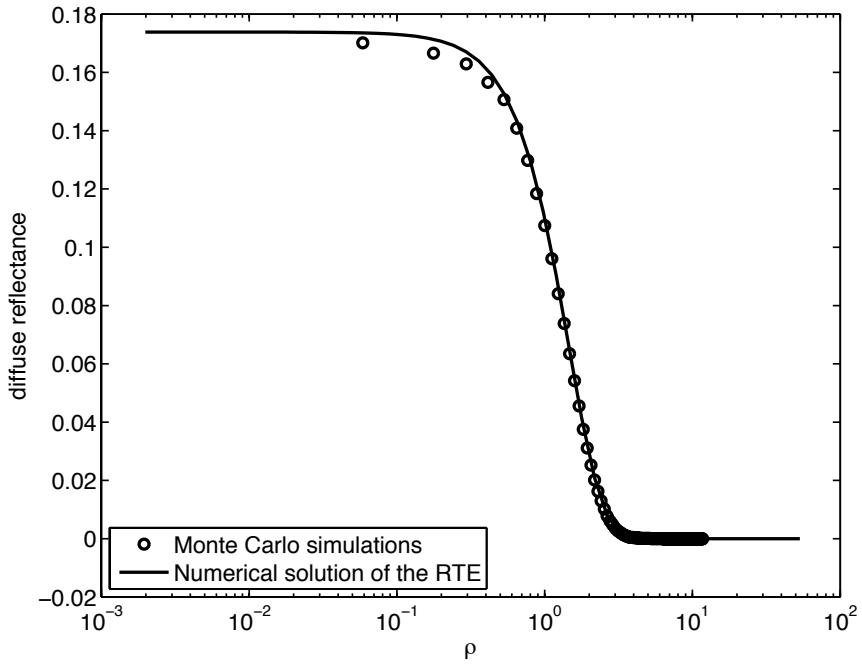

Figure 2.1: Comparison of the diffuse reflectance (normalized by the incident flux F_0) computed using Monte Carlo simulations (circle symbols) and the numerical method to solve the radiative transport equation described in [38] (solid curve). Here, the optical properties for these results are $\mu_s = 100\,\mathrm{mm}^{-1}$, $\mu_a = 0.01\,\mathrm{mm}^{-1}$, $g = 0.8$ and $n_{\mathrm{rel}} = 1.4$. The beam width for these simulations is $w = 0.4247\,\mathrm{mm}$.

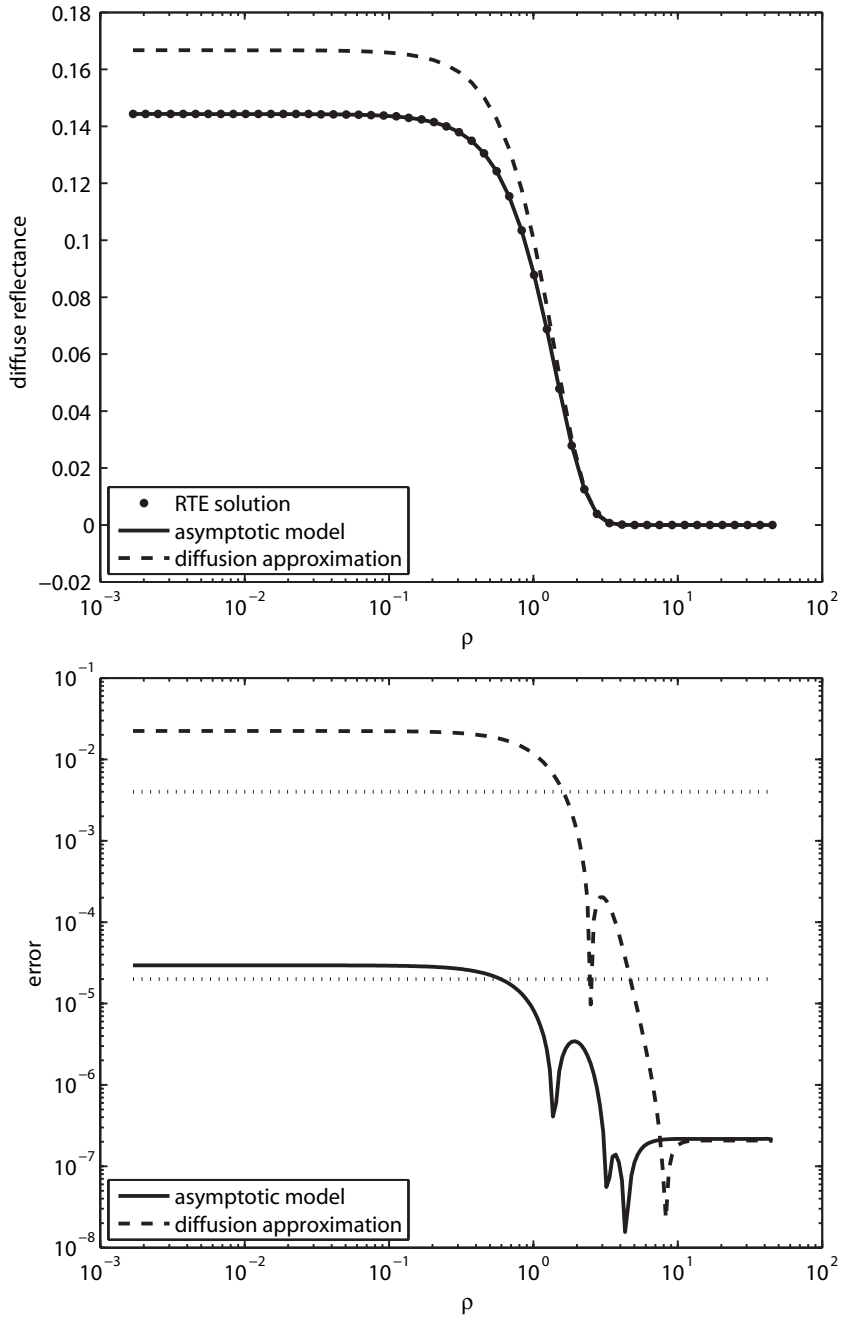

Figure 2.2: The upper plot shows a comparison of the diffuse reflectance (normalized by the incident flux F_0) computed using the numerical solution of the radiative transport equation (circle symbols), the asymptotic model (solid curve) and the diffusion approximation (dashed curve). The lower plot shows the absolute errors of the diffuse reflectance computed using the asymptotic model and the diffusion approximation made with respect to the diffuse reflectance computed using the numerical solution of the radiative transport equation. The optical properties are $\mu_s = 500\,\mathrm{mm}^{-1}$, $\mu_a = 0.01\,\mathrm{mm}^{-1}$, $g = 0.8$ and $n_{\mathrm{rel}} = 1.4$. The beam width is $w = 0.5\,\mathrm{mm}$. Therefore, $\alpha = 2 \times 10^{-5}$, $\beta = 4 \times 10^{-3}$.

asymptotic model given in (2.44) are $a = 0.0227$, $b = 0.0040$, $c = 0.0151$, $R_a = 0.0016$, $R_b = -4.1859$ and $R_c = 0.9883$.

The upper plot of Fig. 2.2 shows results for the diffuse reflectance as a function of ρ, the source-detector separation distance scaled with respect to the beam width. The circle symbols correspond to the diffuse reflectance computed using the numerical solution of the radiative transport equation, the solid curve corresponds to the diffuse reflectance computed using asymptotic model given in (2.44) and the dashed curve corresponds to the diffuse reflectance computed using the diffusion approximation as described in [70]. The asymptotic model and the results from the numerical solution of the radiative transport equation are indistinguishable from one another over the entire range of source-detector separation distances that spans nearly four orders of magnitude. On the other hand, the reflectance computed using the diffusion approximation is inaccurate for small source-detector separation distances. For large source-detector separation distances, both the asymptotic model and the reflectance computed using the diffusion approximation agree with the diffuse reflectance computed using the numerical solution of the radiative transport equation.

To study the accuracy of this model more closely, we show in the lower plot of Fig. 2.2 the absolute error of the asymptotic model and the diffuse reflectance computed using the diffusion approximation with respect to the diffuse reflectance computed using the numerical solution of the radiative transport equation. For reference, we have plotted as dotted curves the magnitude of β (top dotted curve) and α (bottom dotted curve) since $\alpha > \beta^2$. The error of the asymptotic model is on the order of 10^{-5} and lies between β and α consistent with the order of the error predicted by the asymptotic theory. The diffuse reflectance computed using the diffusion approximation produces a much larger error, especially for $\rho \leq 1$. Both models show a dramatic decrease in the error for $\rho \geq 1$.

In Fig. 2.3, we show results when we decrease scattering to $\mu_s = 100\,\mathrm{mm}^{-1}$. It follows that $\alpha = 10^{-4}$ and $\beta = 2 \times 10^{-2}$. In the lower plot of Fig. 2.2, we have plotted as dotted curves the magnitude of β (top dotted curve) and β^2 (bottom dotted curve) since $\beta^2 > \alpha$. Again, the asymptotic model agrees very well with the diffuse reflectance computed using the numerical solution of the radiative transport equation over the entire range of source-detector separation distances.

In Fig. 2.4, we show results when we decrease scattering further and increase absorption. In particular, we set $\mu_s = 50\,\mathrm{mm}^{-1}$ and $\mu_a = 0.1\,\mathrm{mm}^{-1}$ so that $\alpha = 2\times10^{-3}$ and $\beta = 4 \times 10^{-2}$. Here, we observe a noticeable error in the upper plot made by the asymptotic model for short source-detector separation distances. Nonetheless, the lower plot of the error shows that the order of the error is consistent with error estimate produced by the asymptotic analysis. In addition, the error is significantly less than that produced by the diffusion approximation at small source-detector separation distances.

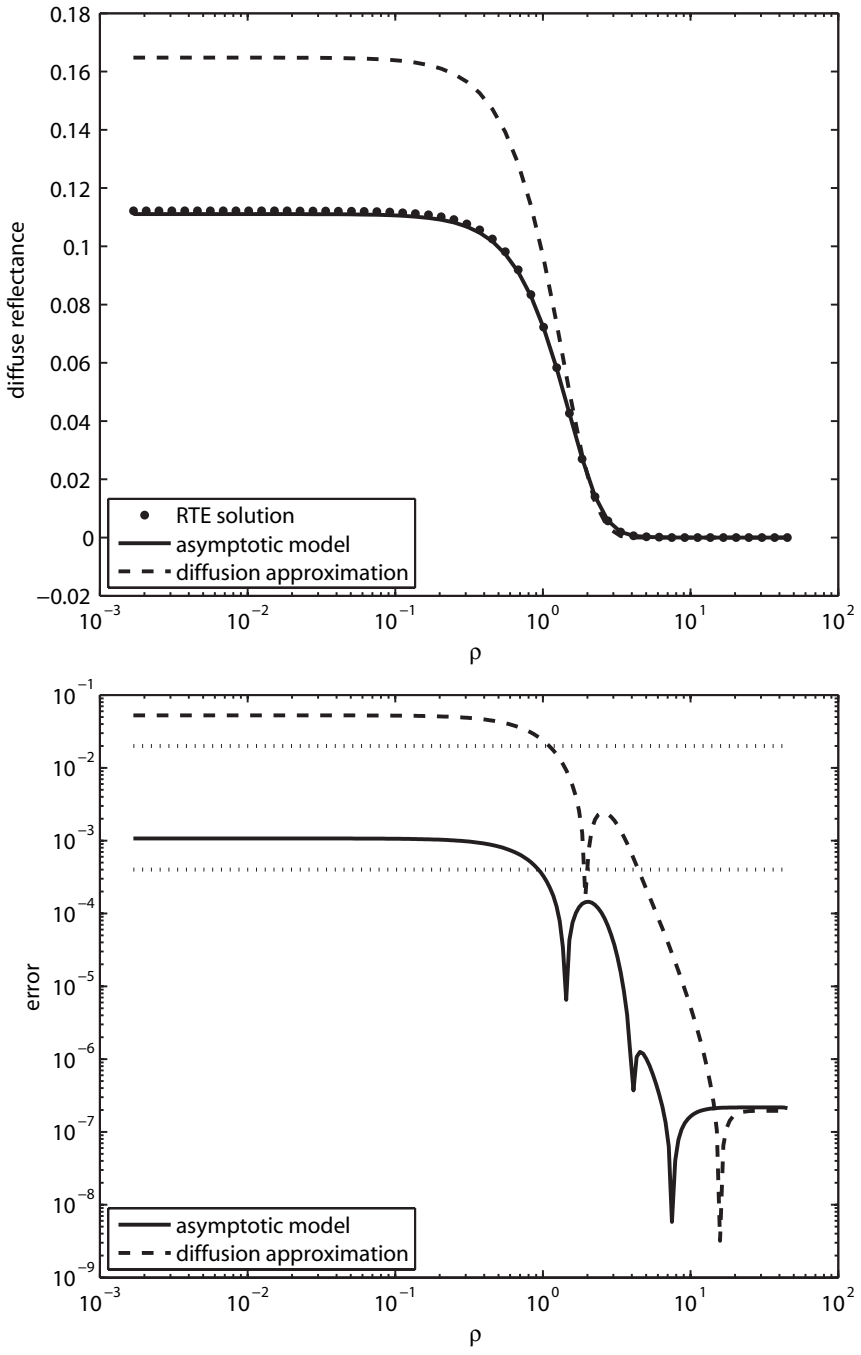

Figure 2.3: The same as Fig. 2.2, except that $\mu_s = 100\,\mathrm{mm}^{-1}$ so that $\alpha = 10^{-4}$ and $\beta = 2 \times 10^{-2}$.

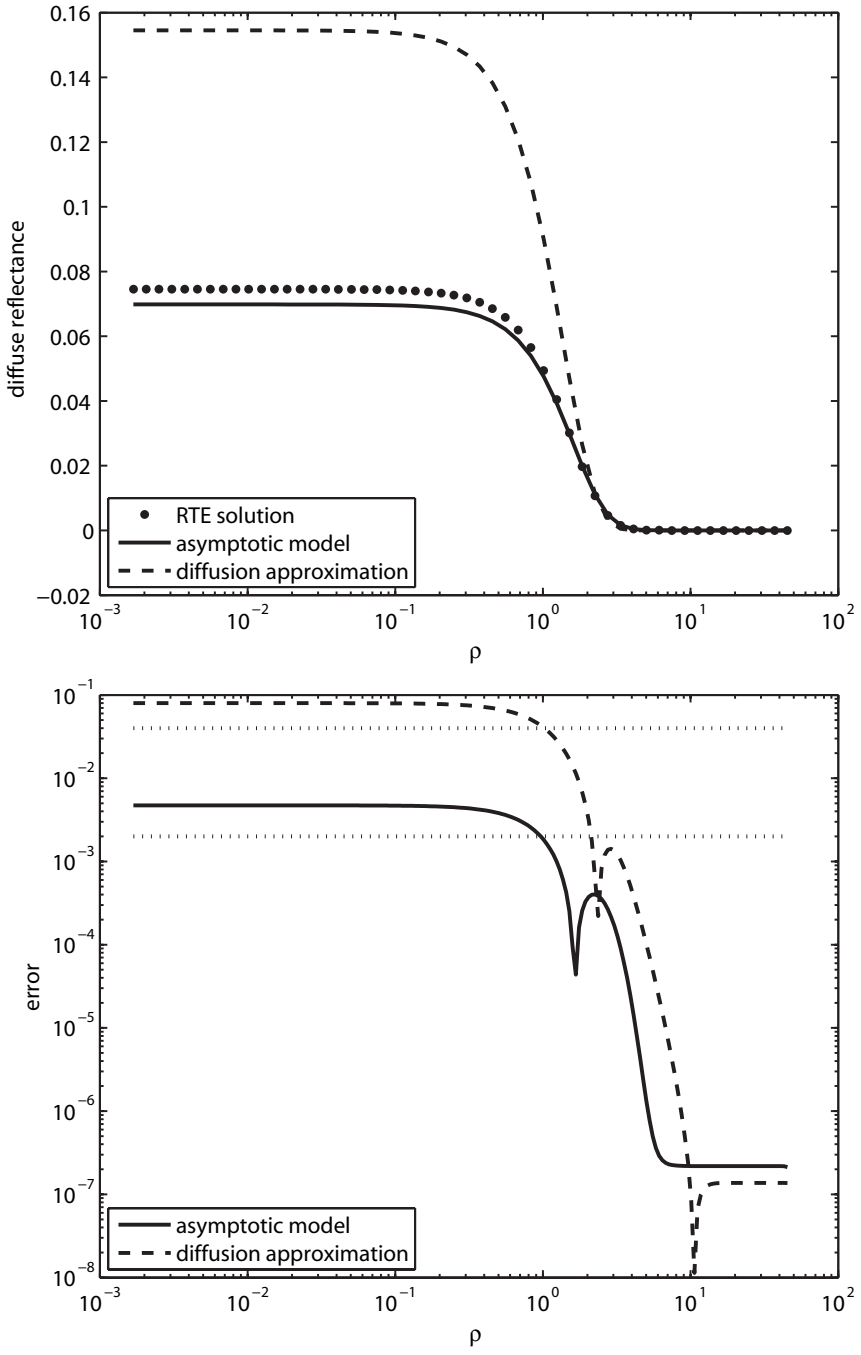

Figure 2.4: The same as Fig. 2.2, except that $\mu_s = 50\,\mathrm{mm}^{-1}$ and $\mu_a = 0.1\,\mathrm{mm}^{-1}$ so that $\alpha = 2 \times 10^{-3}$ and $\beta = 4 \times 10^{-2}$.

Chapter 3

Extending the Corrected Diffusion Approximation to Estimate the Optical Properties of Layered Tissues

We seek to recover optical properties of tissue from the diffuse reflectance to detect early stage cancer cells. To appropriately solve this problem, we must extend our analysis to layered tissues because biological tissue is not strictly homogenous. In fact, biological tissues are inherently layered with a thin epithelium situated above a thick stroma. Thus, we extend the previously described model for a layered medium represented by a thin slab above a semi-infinite half space. Additionally, to solve for the optical properties directly, we must write our solution in a form which can be used easily within an optimization algorithm. We write the diffuse reflectance as a convolution of an explicit kernel with the incident beam profile. We use this convolution model to recover optical properties of epithelial tissues from diffuse reflectance data computed using Monte Carlo simulations. The results in this chapter are published in [53].

3.1 Formulation of the Layered CDA Problem

We examine the form of the diffuse reflectance given in (2.44), and the respective components in (2.36) and (2.37). All of these terms are written in Fourier space as a product with the Fourier Transform of the incident beam profile, $F(\xi, \eta)$. Thus, we can write our reflectance in the form of a convolution

$$R(x, y) = K * f(x, y). \tag{3.1}$$

For the half space problem, K is the kernel whose Fourier transform, $\hat{K}$, is given by

$$\hat{K} = R_a + \frac{c(R_a + \gamma R_b)}{a + b\gamma}. \tag{3.2}$$

The form of R in (3.1) will remain when we extend to a layered system. However $\hat{K}$ will change to include the differing conditions in the respective layers.

We use three length scales in our analysis: the scattering mean free path of the top layer ℓ_{s1}, the characteristic absorption length of the top layer ℓ_{a1}, and the beam width w. We relate the scattering and absorption coefficients of both layers, and use the above length scales to perform similar analysis as the halfspace problem to solve for the radiance and reflectance measurements [52]. We solve for a boundary layer solution within the top layer because the boundary layer is $O(\ell_{s1})$ which is typically much smaller than the thickness of the top layer. We then solve for the radiance in the lower layer solely in the form of the interior solution, resulting in a diffusion approximation for each of the two layers matched at the interface on $z = z_0$. We will show there is great improvement over the standard diffusion approximation for small source-detector separation distances with this model.

We model the layered problem as a thin slab $0 < z < z_0$, above a halfspace $z > z_0$. The boundary value problem for the radiative transport equation is given in (2.1) - (2.3). However in this problem, the radiance is defined in the top layer as I_1, and in the lower half space as I_2. Consequently, we solve the following system of equations:

$$\mu\partial_z I_1 + \sqrt{1-\mu^2}(\cos\varphi\partial_x I_1 + \sin\varphi\partial_y I_1) + \mu_{a1}I_1 + \mu_{s1}L_1 I_1 = 0, \quad \text{in } 0 < z < z_0, \tag{3.3}$$

$$\mu\partial_z I_2 + \sqrt{1-\mu^2}(\cos\varphi\partial_x I_2 + \sin\varphi\partial_y I_2) + \mu_{a2}I_2 + \mu_{s2}L_2 I_2 = 0, \quad \text{in } z_0 < z, \tag{3.4}$$

subject to the following boundary conditions,

$$I_1(\mu,\varphi,x,y,0) - r(\mu)I_1(-\mu,\varphi,x,y,0) = \frac{1}{2\pi}\delta(\mu-1)f(x,y), \quad \text{on } 0 < \mu \le 1, \tag{3.5}$$

$$I_1(\mu,\varphi,x,y,z_0) = I_2(\mu,\varphi,x,y,z_0), \quad -1 \le \mu \le 1, -\pi \le \varphi \le \pi, \tag{3.6}$$

$$I_2(\mu,\varphi,x,y,z) \to 0, \quad \text{as } z \to \infty. \tag{3.7}$$

The interface condition in (3.6) defines that the radiance in the top layer and lower half space are matched for all directions defined on the sphere with respect to μ and φ. This condition ensures consistency of solution between the layers. We also assume that the refractive indices of the two layers is matched due to similarities in biological tissue composition. The boundary condition in (3.7) ensures that the radiance decays to zero, which is consistent for tissues which contain non-zero absorption.

3.2 Rescaling

We rescale $\mathbf{r} = w\bar{\mathbf{r}}$, as before and let $\bar{I}(\mu,\varphi,\bar{x},\bar{y},\bar{z}) = I(\mu,\varphi,x,y,z)$. We define $\ell_{s1} = \dfrac{1}{\mu_{s1}}$, $\ell_{a1} = \dfrac{1}{\mu_{a1}}$, $\ell_{s2} = b_r\ell_{s1}$, $\ell_{a2} = \dfrac{b_r}{a_r}\ell_{a1}$, $\beta = \dfrac{\ell_{s1}}{w}$, $\alpha = \dfrac{\ell_{s1}}{\ell_{a1}}$, where a_r and b_r are defined constants which are $O(1)$. We seek the solution in the limit as α, $\beta \to 0^+$ of

$$\beta\mu\partial_{\bar{z}}\bar{I}_1 + \beta\sqrt{1-\mu^2}(\cos\varphi\partial_{\bar{x}}\bar{I}_1 + \sin\varphi\partial_{\bar{y}}\bar{I}_1) + \alpha\bar{I}_1 + L_1\bar{I}_1 = 0, \quad 0 < \bar{z} < \bar{z}_0, \tag{3.8}$$

$$b_r\beta\mu\partial_{\bar{z}}\bar{I}_2 + b_r\beta\sqrt{1-\mu^2}(\cos\varphi\partial_{\bar{x}}\bar{I}_2 + \sin\varphi\partial_{\bar{y}}\bar{I}_2) + a_r\alpha\bar{I}_2 + L_2\bar{I}_2 = 0, \quad \bar{z} > \bar{z}_0, \tag{3.9}$$

Subject to the boundary conditions

$$\bar{I}_1(\mu,\varphi,\bar{x},\bar{y},0) - r(\mu)\bar{I}_1(-\mu,\varphi,\bar{x},\bar{y},0) = \frac{\delta(\mu-1)}{2\pi}\bar{f}(\bar{x},\bar{y}), \quad \text{on } 0 < \mu \le 1, \tag{3.10}$$

$$\bar{I}_1(\mu,\varphi,\bar{x},\bar{y},\bar{z}_0) = \bar{I}_2(\mu,\varphi,\bar{x},\bar{y},\bar{z}_0), \quad -1 \le \mu \le 1, -\pi \le \varphi \le \pi, \tag{3.11}$$

$$\bar{I}_2(\mu,\varphi,\bar{x},\bar{y},\bar{z}) \to 0 \quad \text{as} \quad \bar{z} \to \infty. \tag{3.12}$$

3.3 Top Layer Analysis

We represent $\bar{I}_1$ as the sum of an interior solution and a boundary layer solution $\bar{I}_1 = \Phi + \Psi$. Using similar analysis as in [52], and chapter 2 in (2.11) - (2.17), we find

$$\Phi = \phi - 3\beta\kappa_1 \hat{\mathbf{s}} \cdot \nabla\phi + O(\beta^2) + O(\alpha), \quad \kappa_1 = 1/[3(1-g_1)]. \tag{3.13}$$

Note that (3.13) is the same as (2.17), but with ϕ_0 replaced by ϕ, which satisfies

$$\nabla \cdot (\kappa_1 \nabla\phi) - \frac{\alpha}{\beta^2}\phi = 0, \quad \text{in } 0 < \bar{z} < \bar{z}_0. \tag{3.14}$$

To examine the boundary layer solution, we introduce $\bar{z} = \beta\zeta$ and let $\bar{\Psi}(\mu,\varphi,\bar{x},\bar{y},\zeta) = \Psi(\mu,\varphi,\bar{x},\bar{y},\beta\zeta)$. We seek solution of the form $\bar{\Psi} \sim \sum_{n=0}^{\infty} \beta^n \psi_n$, as $\beta \to 0^+$, substitute this expansion into (3.8) and collect like-powers of β to obtain to $O(1)$

$$\mu\partial_\zeta\psi_0 + L_1\psi_0 = 0. \tag{3.15}$$

To $O(\beta)$ we find that ψ_1 satisfies

$$\mu\partial_\zeta\psi_1 + L_1\psi_1 = -\sqrt{1-\mu^2}(\cos\varphi\partial_{\bar{x}}\psi_0 + \sin\varphi\partial_{\bar{y}}\psi_0). \tag{3.16}$$

Note that we have obtained the same problem defined in (2.19) - (2.20). Substituting $I_1 = \Phi + \bar{\Psi}$ into the boundary condition we have

$$\begin{aligned}\bar{\Psi}(\mu,\varphi,\bar{x},\bar{y},0) - r(\mu)\bar{\Psi}(-\mu,\varphi,\bar{x},\bar{y},0) = \frac{\delta(\mu-1)}{2\pi}\bar{f}(\bar{x},\bar{y}) \\ - \Phi(\mu,\varphi,\bar{x},\bar{y},0) + r(\mu)\Phi(-\mu,\varphi,\bar{x},\bar{y},0), 0 < \mu \le 1.\end{aligned} \tag{3.17}$$

The boundary condition on ϕ is found through the same projection operator defined in (2.23), resulting in (2.25) - (2.28) again, which, after integrating with respect to φ yields

$$a\phi(\bar{x},\bar{y},0) - b\partial_{\bar{z}}\phi(\bar{x},\bar{y},0) = c\bar{f}(\bar{x},\bar{y}). \tag{3.18}$$

In this boundary condition, we compute a, b, and c by evaluating

$$a = P[1 - r(\mu)], \tag{3.19}$$

$$b = 3\beta\kappa_1 P[\mu + \mu r(\mu)], \tag{3.20}$$

$$c = \frac{1}{2\pi}P[\delta(\mu-1)]. \tag{3.21}$$

We apply similar analysis as in [52]. Fourier transforming (3.14) with respect to x and y yields

$$-\xi^2\hat{\phi} - \eta^2\hat{\phi} + \partial_{\bar{z}}^2\hat{\phi} - \frac{\alpha}{\kappa_1\beta^2}\hat{\phi} = 0, \tag{3.22}$$

where ξ and η are the Fourier dual variables to x and y, respectively. The general solution of (3.22) is

$$\hat{\phi} = A(\xi,\eta)e^{-\gamma_1 \bar{z}} + B(\xi,\eta)e^{\gamma_1(\bar{z}-\bar{z}_0)}, \tag{3.23}$$

Where γ_1 is defined as

$$\gamma_1^2 = \xi^2 + \eta^2 + \frac{\alpha}{\kappa_1 \beta^2}. \tag{3.24}$$

Upon substituting (3.23) into the Fourier transform of boundary condition (3.18), we find

$$a[A(\xi,\eta) + B(\xi,\eta)e^{-\gamma_1 \bar{z}_0}] - b[-\gamma_1 A(\xi,\eta) + \gamma_1 B(\xi,\eta)e^{-\gamma_1 \bar{z}_0}] = cF(\xi,\eta), \tag{3.25}$$

where $F(\xi,\eta)$ is the Fourier transform of $\bar{f}(\bar{x},\bar{y})$. To solve for A and B we must evaluate the boundary condition at $\bar{z} = \bar{z}_0$, which requires analysis of the half space which we discuss below.

3.4 Half Space Analysis

The boundary layer solution is designed to decay to zero outside the boundary layer of thickness $O(\beta)$, and because $\bar{z}_0 \gg \beta$ we can assume the contribution from $\bar{\Psi}$ is negligible at $\bar{z} = \bar{z}_0$. We compute I_2 in the same manner as the interior solution for the top layer, with $\bar{I}_2 \sim \sum_{n=0}^{\infty} \beta^n \mathscr{I}_n$, as $\beta \to 0^+$. Substituting this expansion into (3.9), and collecting terms in like-powers of β, we find to $O(1)$ that

$$L_2 \mathscr{I}_0 = 0. \tag{3.26}$$

To $O(\beta)$, we find that

$$L_2 \mathscr{I}_1 = -b_r \mu \partial_{\bar{z}} \mathscr{I}_0 - b_r \sqrt{1-\mu^2}(\cos\varphi \partial_{\bar{x}} \mathscr{I}_0 + \sin\varphi \partial_{\bar{y}} \mathscr{I}_0). \tag{3.27}$$

Solving (3.26), we find that $\mathscr{I}_0 = \mathscr{I}_0(\mathbf{r})$. We then apply the same methods used in (2.11) - (2.13) to find that

$$\bar{I}_2 = \mathscr{I} - 3b_r \beta \kappa_2 \mathbf{s} \cdot \nabla \mathscr{I} + O(\beta^2) + O(\alpha), \quad \kappa_2 = 1/[3(1-g_2)]. \tag{3.28}$$

We will henceforth use $\mathscr{I}$ in place of $\mathscr{I}_0$.

Following similar analysis of the interior solution we used in Chapter 2, we apply the solvability condition to the $O(\beta^2)$ equation:

$$L_2 \mathscr{I}_2 = -b_r \mu \partial_{\bar{z}} \mathscr{I}_1 - b_r \sqrt{1-\mu^2}(\cos\varphi \partial_{\bar{x}} \mathscr{I}_1 + \sin\varphi \partial_{\bar{y}} \mathscr{I}_1) - \frac{a_r \alpha}{\beta^2} \mathscr{I}, \tag{3.29}$$

where

$$\mathscr{I}_1 = -\frac{1}{(1-g_2)} \hat{\mathbf{s}} \cdot \nabla \mathscr{I}, \tag{3.30}$$

to determine that $\mathscr{I}$ satisfies

$$b_r^2 \nabla \cdot (\kappa_2 \nabla \mathscr{I}) - \frac{a_r \alpha}{\beta^2} \mathscr{I} = 0. \tag{3.31}$$

Upon Fourier transforming (3.30), we find that $\hat{\mathscr{I}}$ is given by

$$\hat{\mathscr{I}} = D(\xi,\eta)e^{-\gamma_2(\bar{z}-\bar{z}_0)}, \quad \bar{z} > \bar{z}_0, \tag{3.32}$$

where γ_2 is defined as

$$\gamma_2^2 = \xi^2 + \eta^2 + \frac{a_r\alpha}{b_r^2\beta^2\kappa_2}. \tag{3.33}$$

3.5 Interior Boundary Condition

Rather than perform a formal boundary layer analysis for boundary condition (3.11), we set $\phi = \mathscr{I}$ and $\kappa_1\hat{z}\cdot\nabla\phi = b_r\kappa_2\hat{z}\cdot\nabla\mathscr{I}$ on $z = z_0$. Fourier transforming these two equations yields $\hat{\phi} = \hat{\mathscr{I}}$ and $\kappa_1\partial_z\hat{\phi} = b_r\kappa_2\partial_z\hat{\mathscr{I}}$ on $z = z_0$. Substituting (3.23) and (3.32) into these boundary conditions yields

$$A(\xi,\eta)e^{-\gamma_1 z_0} + B(\xi,\eta) = D(\xi,\eta), \tag{3.34}$$

$$3\kappa_1(-\gamma_1 A(\xi,\eta)e^{-\gamma_1 z_0} + \gamma_1 B(\xi,\eta)) = -3b_r\kappa_2\gamma_2 D(\xi,\eta). \tag{3.35}$$

Solving (3.35) for $D(\xi,\eta)$, and setting it equal to the left side of (3.34), we find

$$B(\xi,\eta) = \chi A(\xi,\eta)e^{\gamma_1\bar{z}_0}, \tag{3.36}$$

where

$$\chi = \frac{\kappa_1\gamma_1 - b_r\kappa_2\gamma_2}{\kappa_1\gamma_1 + b_r\kappa_2\gamma_2}e^{-2\gamma_1\bar{z}_0}. \tag{3.37}$$

Substituting (3.36) into (3.25) and solving for A, we find that

$$A(\xi,\eta) = \frac{cF(\xi,\eta)}{a(1+\chi) + b\gamma_1(1-\chi)}. \tag{3.38}$$

Therefore, ϕ is given by

$$\phi(\bar{x},\bar{y},\bar{z}) = \iint (A(\xi,\eta)e^{-\gamma_1\bar{z}} + B(\xi,\eta)e^{\gamma_1(\bar{z}-\bar{z}_0)})e^{i\xi\bar{x}+i\eta\bar{y}}d\xi d\eta, \tag{3.39}$$

and consequently

$$\partial_{\bar{z}}\phi(\bar{x},\bar{y},\bar{z}) = \iint (-\gamma_1 A(\xi,\eta)e^{-\gamma_1\bar{z}} + \gamma_1 B(\xi,\eta)e^{\gamma_1(\bar{z}-\bar{z}_0)})e^{i\xi\bar{x}+i\eta\bar{y}}d\xi d\eta. \tag{3.40}$$

With (3.39) and (3.40), we have the results needed to compute the interior solution's contribution to the diffuse reflectance.

3.6 Computing the Boundary Layer Solution

We compute the Boundary Layer Solution in the same manner as we have done to obtain (2.29) - (2.32). Using the half space Green's Function given in (B.17), we write

$$\bar{\Psi}|_{\zeta=0} = \frac{H_1(\mu,0)\bar{f}(\bar{x},\bar{y})}{2\pi} - H_2(\mu,0)\phi(\bar{x},\bar{y},0) + 3\beta\kappa_1 H_3(\mu,0)\partial_{\bar{z}}\phi(\bar{x},\bar{y},0), \tag{3.41}$$

with

$$H_1(\mu,\zeta) = \int_0^1 G(\mu,\zeta;\mu',0)\delta(\mu'-1)\mu' d\mu', \tag{3.42}$$

$$H_2(\mu,\zeta) = \int_0^1 G(\mu,\zeta;\mu',0)(1-r(\mu'))\mu' d\mu', \tag{3.43}$$

$$H_3(\mu,\zeta) = \int_0^1 G(\mu,\zeta;\mu',0)(\mu'+r(\mu')\mu')\mu' d\mu'. \tag{3.44}$$

Combining all of our results, we find that the intensity at $z=0$ is given by

$$\tilde{I}_1(\mu,\bar{x},\bar{y},0) = \frac{H_1(\mu,0)\bar{f}(\bar{x},\bar{y})}{2\pi} + [1-H_2(\mu,0)]\phi(\bar{x},\bar{y},0) - 3\beta\kappa_1[\mu - H_3(\mu,0)]\partial_{\bar{z}}\phi(\bar{x},\bar{y},0) + O(\beta^2) + O(\alpha). \tag{3.45}$$

3.7 Diffuse Reflectance due to Layered Medium

We compute the diffuse reflectance by integrating the radiance over the range of angles exiting the media collected by a detector with numerical aperture defined by μ_{NA}.

$$R(\bar{x},\bar{y}) = -2\pi \int_{-1}^{-\mu_{NA}} t(\mu)\tilde{I}_1(\mu,\bar{x},\bar{y},0)\mu d\mu. \tag{3.46}$$

By substituting (3.45) into (3.46), we obtain

$$R(\bar{x},\bar{y}) = R_a\bar{f}(\bar{x},\bar{y}) + R_b\phi(\bar{x},\bar{y},0) - R_c\partial_{\bar{z}}\phi(\bar{x},\bar{y},0) + O(\beta^2) + O(\alpha), \tag{3.47}$$

with

$$R_a = -2\pi \int_{-1}^{-\mu_{NA}} t(\mu)H_1(\mu,0)\mu d\mu, \tag{3.48}$$

$$R_b = -2\pi \int_{-1}^{-\mu_{NA}} t(\mu)(1-H_2(\mu,0))\mu d\mu, \tag{3.49}$$

and

$$R_c = -6\pi\beta\kappa_1 \int_{-1}^{-\mu_{NA}} t(\mu)(\mu - H_3(\mu,0))\mu d\mu. \tag{3.50}$$

3.8 Convolution CDA for Layered Medium

By substituting (3.38) - (3.40) into the Fourier Transform of (3.47), and simplifying the result. we can write the reflectance as a convolution in the same form as (3.1), but with the kernel whose Fourier transform, $\hat{K}$, is given by

$$\hat{K} = R_a + \frac{c[R_b(1+\chi) + 3\kappa_1\gamma_1 R_c(1-\chi)]}{a(1+\chi) + 3\kappa_1 b\gamma_1(1-\chi)}. \tag{3.51}$$

In this equation, χ is as defined in (3.37). This equation is in the form which has been nondimensionalized by rescaling with respect to the beam width in the derivation of CDA.

3.9 Redimensionalization of the CDA Reflectance Computation

In biomedical optics applications, researchers prefer to work with dimensionalized models. For this reason, we redimensionalize the CDA. After doing so, we compare our results with Monte Carlo simulations, which are an accepted standard test in the field of biomedical optics. We revert back to $\mathbf{r} = w\bar{\mathbf{r}}$, $\beta = 1/(w\mu_{s1})$, $\alpha = \mu_{a1}/\mu_{s1}$, and $\kappa_1 = 1/(3\mu_{s1}(1-g_1))$, substituting these into our interior solution (3.14) yields the redimensionalized diffusion equation

$$\nabla \cdot [\kappa_1 \nabla \phi(\mathbf{r})] - \mu_{a1}\phi(\mathbf{r}) = 0, \quad 0 < z < z_0. \tag{3.52}$$

We determine redimensionalized boundary condition (3.19) to be

$$a\phi(x,y,0) - \tilde{b}\partial_z \phi(x,y,0) = cf(x,y), \tag{3.53}$$

$$\tilde{b} = \frac{3\kappa_1}{w} P[\mu + \mu r(\mu)]. \tag{3.54}$$

In this, the projection operator P is as defined in (2.23).

We solve for the redimensionalized interior solution by Fourier transforming (3.52)

$$\partial_z^2 \hat{\phi} - \left[\frac{\mu_{a1}}{\kappa_1} + k_x^2 + k_y^2\right] \hat{\phi} = 0, \tag{3.55}$$

where (k_x, k_y) are the Fourier dual variables of (x, y). Using the same form of exponential decay in z as (3.23), $Ae^{-k_{z1}z} + Be^{k_{z1}(z-z_0)}$, we find the relation

$$k_{z1}^2 = \frac{\mu_{a1}}{\kappa_1} + k_x^2 + k_y^2. \tag{3.56}$$

Similarly,

$$k_{z2}^2 = \frac{\mu_{a2}}{\kappa_2} + k_x^2 + k_y^2. \tag{3.57}$$

By applying the same analysis for the interior boundary condition (3.33) - (3.38), we solve for A and B and find that

$$A(k_x, k_y) = \frac{cF(k_x, k_y)}{a(1+\Xi) + \tilde{b}k_{z1}(1-\Xi)}, \tag{3.58}$$

and

$$B(k_x, k_y) = \Xi A(k_x, k_y) e^{k_{z1}z_0}, \tag{3.59}$$

where

$$\Xi = \frac{\mu_{s2}(1-g_2)k_{z1} - \mu_{s1}(1-g_1)k_{z2}}{\mu_{s2}(1-g_2)k_{z1} + \mu_{s1}(1-g_1)k_{z2}} e^{-2k_{z1}z_0}. \tag{3.60}$$

Using (3.58) - (3.60), we determine the redimensionalized interior solution is

$$\phi(x,y,z) = \iint \frac{c(e^{-k_{z1}z} + \Xi e^{k_{z1}z})}{a(1+\Xi) + \tilde{b}k_{z1}(1-\Xi)} e^{\mathrm{i}k_x x + \mathrm{i}k_y y} \mathrm{d}k_x \mathrm{d}k_y. \tag{3.61}$$

Consequently,

$$\partial_z\phi(x,y,z) = -\iint \frac{ck_{z1}(-e^{-k_{z1}z} + \Xi e^{k_{z1}z})}{a(1+\Xi) + \tilde{b}k_{z1}(1-\Xi)} e^{\mathrm{i}k_x x + \mathrm{i}k_y y} \mathrm{d}k_x \mathrm{d}k_y. \tag{3.62}$$

We now redimensionalize the boundary layer solution. We redefine $\zeta = \mu_{s1} z$ so that (3.16) becomes

$$\mu\partial_z\psi_0 + \mu_{s1}L_1\psi_0 = 0. \tag{3.63}$$

Similarly, the redimensionalization changes (3.17) to

$$\mu\partial_z\psi_1 + \mu_{s1}L_1\psi_1 = -\sqrt{1-\mu^2}(\cos\varphi\partial_x\psi_0 + \sin\varphi\partial_y\psi_0). \tag{3.64}$$

The boundary condition (3.18) is also modified to be

$$\Psi(\mu,x,y,0) - r(\mu)\Psi(-\mu,x,y,0) = \frac{\delta(\mu-1)}{2\pi} f(x,y) - [1-r(\mu)]\phi_(x,y,0) + 3\kappa_1\mu[1+r(\mu)]\partial_z\phi_(x,y,0) \quad 0 < \mu \le 1. \tag{3.65}$$

Let $G(\mu, z; \mu', z')$ denote the solution of

$$\mu\partial_z G + \mu_{s1}G - \mu_{s1}\int_{-1}^{1} h(\mu,\mu')G(\mu,z;\mu',z')\mathrm{d}\mu' = \delta(\mu-\mu')\delta(z-z'), \tag{3.66}$$

where $h(\mu,\mu')$ is the scattering phase function after integration in φ, subject to

$$G(\mu,0;\mu',z') - r(\mu)G(-\mu,0;\mu',z') = 0, \quad 0 < \mu \le 1. \tag{3.67}$$

Then, the solution of (3.63) and (3.64) subject to (3.65) is given by

$$\Psi(\mu,x,y,z) = H_1(\mu,z)f(x,y) - H_2(\mu,z)\phi(x,y,z) + 3\kappa_1 H_3(\mu,z)\partial_z\phi(x,y,z), \tag{3.68}$$

where

$$H_1(\mu,z) = \frac{1}{2\pi}G(\mu,z;1,0), \tag{3.69}$$

$$H_2(\mu,z) = \int_0^1 G(\mu,z;\mu',0)[1-r(\mu')]\mu'\mathrm{d}\mu', \tag{3.70}$$

$$H_3(\mu,z) = \int_0^1 G(\mu,z;\mu',0)[\mu'+\mu' r(\mu')]\mu'\mathrm{d}\mu', \tag{3.71}$$

According to the results above, the diffuse reflectance is given by

$$R(x,y) = -2\pi\int_{-1}^{-\mu_{NA}} \left[\Psi(\mu,x,y,0) + \phi(x,y,0) - 3\kappa_1\mu\partial_z\phi(x,y,0)\right] t(\mu)\mu\mathrm{d}\mu. \tag{3.72}$$

Substituting (3.68) into (3.72), we find that

$$R(x,y) = R_a f(x,y) + R_b\phi(x,y,0) - \frac{R_c}{\mu_{s1}(1-g_1)}\partial_z\phi(x,y,0), \tag{3.73}$$

with

$$R_a = -2\pi \int_{-1}^{-\mu_{\rm NA}} t(\mu) H_1(\mu, 0) \mu \mathrm{d}\mu, \tag{3.74}$$

$$R_b = -2\pi \int_{-1}^{-\mu_{\rm NA}} t(\mu)[1 - H_2(\mu, 0)] \mu \mathrm{d}\mu, \tag{3.75}$$

$$R_c = -6\pi\kappa_1 \int_{-1}^{-\mu_{\rm NA}} t(\mu)[\mu - H_3(\mu, 0)] \mu \mathrm{d}\mu. \tag{3.76}$$

Using (3.61) and (3.62), we can write the diffuse reflectance as

$$R(x, y) = \iint \left[R_a + \frac{c(R_b(1 + \Xi) - R_c k_{z1}(1 - \Xi)}{a(1 + \Xi) + \tilde{b} k_z (1 - \Xi)} \right] \hat{F}(k_x, k_y) e^{\mathrm{i}k_x x + \mathrm{i}k_y y} \mathrm{d}k_x \mathrm{d}k_y. \tag{3.77}$$

This presents the form of the kernel for the layered problem upon redimensionalization as

$$\hat{K} = R_a + \frac{c(R_b(1 + \Xi) - R_c k_{z1}(1 - \Xi))}{a(1 + \Xi) + \tilde{b} k_{z1}(1 - \Xi)}. \tag{3.78}$$

The distinctive feature of the model is that the first term in the kernel, given in (3.78), is proportional to the incident beam profile, f. This term comes from the boundary layer analysis, and provides a more accurate approximation for small source-detector separation distances.

In [52], the diffusion coefficient κ is defined as $3\kappa = \mu_s'^{-1}$, where $\mu_s' = \mu_s(1 - g)$. This particular form of the diffusion equation comes about from the assumption that $\mu_a \ll \mu_s$. Consequently, any contribution of μ_a to κ is negligibly small. Alternatively, Pomraning [48] provided a different scaling of the governing radiative transport equation, which does not require as severe an assumption on μ_a. With that scaling, the asymptotic analysis of the radiative transport equation yields the more standard diffusion coefficient, which we denote by D, in which $3D = (\mu_s' + \mu_a)^{-1}$. Therefore, we modify (3.78) by replacing each $\kappa_{1,2}$ with $D_{1,2}$ for the respective layer.

3.10 Comparison of Convolution CDA and Monte Carlo Simulations

In Figure 3.1, we show comparisons of the diffuse reflectance computed using Monte Carlo simulations (circle symbols), the convolution model (solid curve), and the standard diffusion approximation (dashed curve) described in [70], extended to a two-layer system. For the Monte Carlo simulations, we used the method described in [46] available at http://www.virtualphotonics.org with 10^6 photons. We have taken values for the optical properties from the paper by Kienle *et al.* [30]. In particular, the optical properties of the top, epithelial layer are $\mu_{a1} = 0.02\,\mathrm{mm}^{-1}$, $\mu_{s1} = 6.5\,\mathrm{mm}^{-1}$, and $g_1 = 0.80$. The optical properties of the bottom, stromal layer are $\mu_{a2} = 0.01\,\mathrm{mm}^{-1}$, $\mu_{s2} = 6\,\mathrm{mm}^{-1}$, and $g_2 = 0.80$. The layer thickness is $z_0 = 0.25\,\mathrm{mm}$, and the air-tissue refractive index is set to $n_{rel} = 1.4$. The numerical aperture (NA) is set to NA $= 1$ which corresponds to the full range of μ exiting the medium, $\mu_{NA} = 0$. The beam profile, f, corresponds to a collimated Gaussian beam, $f(x, y) = \exp[-(x^2 + y^2)/w^2]/(2\pi w^2)$ with $w = \mathrm{FWHM}/\sqrt{2\log 2}$, and FWHM $= 5\,\mathrm{mm}$ denoting the full width at half maximum of the beam. One could change the beam profile easily just by changing f.

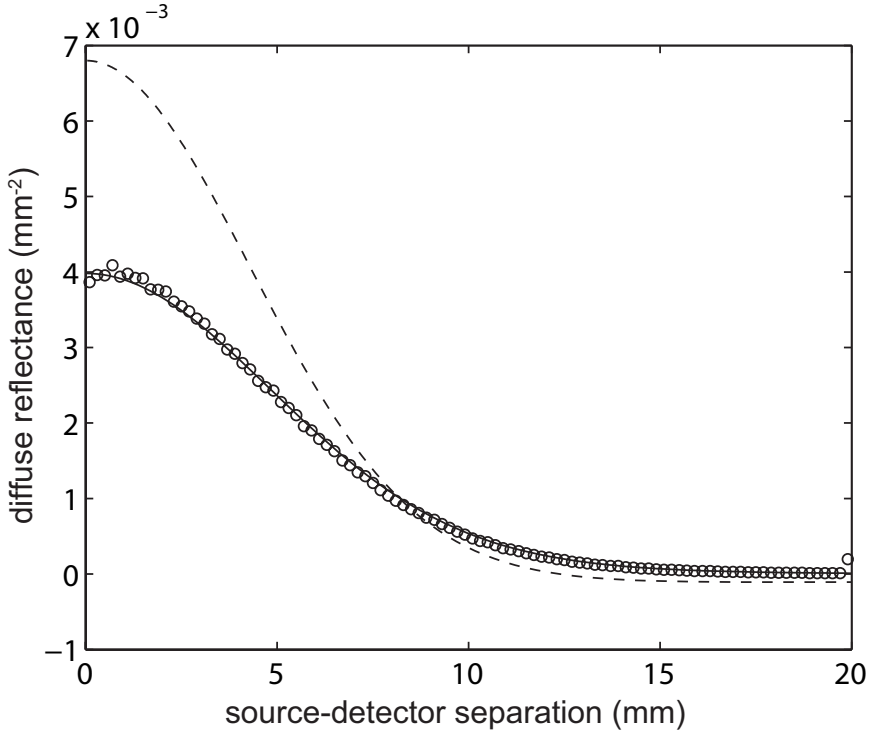

Figure 3.1: Comparison of the diffuse reflectance by Monte Carlo simulations (circle symbols), the convolution model (solid curve), and the standard diffusion approximation (dashed curve). The optical properties, taken from Kienle *et al.* [30], for the top layer are $\mu_{a1} = 0.02\,\mathrm{mm}^{-1}$, $\mu_{s1} = 6.5\,\mathrm{mm}^{-1}$, and $g_1 = 0.80$, and the optical properties for the bottom layer are $\mu_{a2} = 0.01\,\mathrm{mm}^{-1}$, $\mu_{s2} = 6\,\mathrm{mm}^{-1}$, and $g_2 = 0.80$. The layer thickness is $z_0 = 0.25\,\mathrm{mm}$, the refractive index is $n_{rel} = 1.4$, and NA $= 1$.

Fig. 3.1 shows that the convolution model is significantly more accurate than the standard diffusion approximation when compared to Monte Carlo simulations, especially for small source-detector separation distances. These results are consistent with those of the corrected diffusion approximation [52], and show an increase in accuracy over the standard diffusion approximation. This accuracy, coupled with the simplicity of the model, provides a fast and accurate model for predicting measurements of the diffuse reflectance.

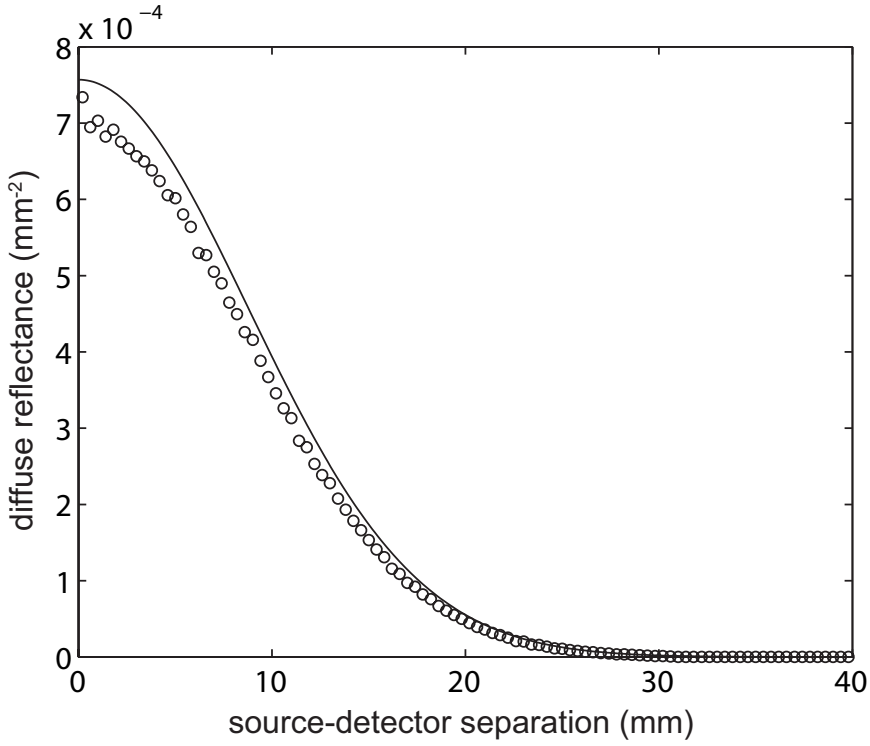

Figure 3.2: Comparison of the diffuse reflectance by Monte Carlo simulations (circle symbols) and the convolution model (solid curve). The optical properties, taken from Kortun *et al.* [42], for the top layer are $\mu_{a1} = 0.12\,\mathrm{mm}^{-1}$, $\mu_{s1} = 1.644\,\mathrm{mm}^{-1}$, and $g_1 = 0.80$, and the optical properties for the bottom layer are $\mu_{a2} = 0.097\,\mathrm{mm}^{-1}$, $\mu_{s2} = 10.32\,\mathrm{mm}^{-1}$, and $g_2 = 0.80$. The layer thickness is $z_0 = 0.25\,\mathrm{mm}$, the refractive index is $n_{rel} = 1.4$, and NA = 1.

In Figure 3.2, we show comparisons for optical properties we have taken from the paper by Kortun *et al.* [42]. In using these values, we maintained the same values of the reduced scattering coefficients: $\mu'_{s1,2} = \mu_{s1,2}(1 - g_{1,2})$, but changed the scattering coefficients, $\mu_{s1,2}$, so that $g_{1,2} = 0.8$ since the value of the anisotropy factor when $0.8 \leq g < 1$ does not significantly change the reflectance [30]. In particular, the optical properties of the top, epithelial layer are $\mu_{a1} = 0.12\,\mathrm{mm}^{-1}$, $\mu_{s1} = 1.644\,\mathrm{mm}^{-1}$, and $g_1 = 0.80$. The optical properties of the bottom, stromal layer are $\mu_{a2} = 0.097\,\mathrm{mm}^{-1}$, $\mu_{s2} = 10.32\,\mathrm{mm}^{-1}$, and $g_2 = 0.80$. Notice that the scattering coefficient of the epithelium for this case is much smaller than the former one. To maintain the condition that $w\mu_{s1}(1 - g_1) \gg 1$, we increase the width of the collimated Gaussian beam to have FWHM = 10 mm. All other parameters are the same as for Fig. 3.1.

Despite the fact that scattering is not very strong in the epithelium, Fig. 3.2 shows that the convolution model provides a good approximation to the diffuse reflectance computed using Monte Carlo simulations. We do not include a curve for the standard diffusion approximation in Fig. 3.2 because it does not yield a physically consistent solution, *i.e.* a negative diffuse reflectance.

3.11 Computation of Optical Properties

We now turn our attention to using the convolution model to estimate the optical properties of epithelial tissues. To do so, we assume *a priori* knowledge of the layer thickness, z_0, the relative refractive index, n_{rel}, and the optical properties of the lower layer: μ_{a2}, μ_{s2}, and g_2. Suppose we have measured the diffuse reflectance for a finite set of source-detector separation distances, *e.g.* $R_i = R(\rho_i)$ for $i = 1, \cdots, N$. Let $\mathbf{d} = (R_1, \cdots, R_N)$ denote a data vector whose entries are these individual diffuse reflectance measurements. Given the optical properties of the top layer: μ_{a1}, μ_{s1}, and g_1, we can compute the model vector $\mathbf{m} = (M_1, \cdots, M_N)$ whose entries are evaluations of the convolution model given by (3.77). We seek to estimate the optical properties of the top layer through solution of the nonlinear least-squares problem:

$$\min_{\mu_{a1},\mu_{s1},g_1} \frac{1}{2}||\mathbf{d} - \mathbf{m}||_2^2. \tag{3.79}$$

To solve (3.79), we use *lsqnonlin* implemented in MATLAB (Mathworks, Inc., Natick, Massachusetts). For this problem, we set upper and lower bounds for each optical property sought. In particular, we set $10^{-4}\,\mathrm{mm}^{-1} \leq \mu_{a1} \leq 1\,\mathrm{mm}^{-1}$, $10^{-1}\,\mathrm{mm}^{-1} \leq \mu_{s1} \leq 10\,\mathrm{mm}^{-1}$, and $0.70 \leq g_1 \leq 0.99$. This minimization problem is sensitive to the initial guess for the optical properties due to the existence of many local minima.

The key here is that $\hat{K}$ given in (3.78) depends on $R_{a,b,c}$ which, in turn, depends non-trivially on μ_{a1}, μ_{s1}, and g_1. Hence, we may be able to recover these parameters through solution of (3.79). In contrast, by using just the standard diffusion approximation, one is not able to separate μ_{s1} and g_1 easily since those optical properties appear in the diffusion approximation only through $\mu'_{s1} = \mu_{s1}(1 - g_1)$.

We first solve (3.79) to recover the top (epithelial) layer optical properties corresponding to the parameter values taken from Kienle *et al.* [30]. Hence, the values we seek to recover are $\mu_{a1} = 0.02\,\mathrm{mm}^{-1}$, $\mu_{s1} = 6.5\,\mathrm{mm}^{-1}$, and $g_1 = 0.80$. In other words, we seek the top (epithelial) layer optical properties, μ_{a1}, μ_{s1}, and g_1, by fitting the convolution model for the diffuse reflectance to the diffuse reflectance computed using Monte Carlo simulations shown in Fig. 3.1. The collimated Gaussian beam incident on the medium has FWHM = 5 mm. We compared values of the diffuse reflectance at four source-detector separation distances: $\rho_1 = 2.5\,\mathrm{mm}$, $\rho_2 = 6.5\,\mathrm{mm}$, $\rho_3 = 10.5\,\mathrm{mm}$, and $\rho_4 = 14.5\,\mathrm{mm}$. To start the nonlinear least-squares solver, we set the initial guess for the epithelial optical properties to be $\tilde{\mu}_{a1}^0 = 0.1\,\mathrm{mm}^{-1}$, $\tilde{\mu}_{s1}^0 = 2.0\,\mathrm{mm}^{-1}$, and $\tilde{g}_1^0 = 0.72$. The results from this computation are $\tilde{\mu}_{a1} = 0.0164\,\mathrm{mm}^{-1}$ (18.00% error), $\tilde{\mu}_{s1} = 7.7687\,\mathrm{mm}^{-1}$ (19.52% error), and $\tilde{g}_1 = 0.7026$ (12.17% error).

Next, we solve (3.79) to recover the top (epithelial) layer optical properties corresponding to the parameter values taken from Kortun *et al.* [42] corresponding to the diffuse reflectances shown in Fig. 3.2. Hence, the values we seek to recover are $\mu_{a1} = 0.12\,\mathrm{mm}^{-1}$, $\mu_{s1} = 1.644\,\mathrm{mm}^{-1}$, and $g_1 = 0.80$. For this problem, the collimated

Gaussian beam incident on the medium has FWHM = 10 mm, and we consider the diffuse reflectance at four source-detector separation distances: $\rho_1 = 5\,\text{mm}$, $\rho_2 = 13\,\text{mm}$, $\rho_3 = 21\,\text{mm}$, and $\rho_4 = 29\,\text{mm}$. To start the nonlinear least-squares solver, we set the initial guess for the epithelial optical properties to be $\tilde{\mu}_{a1}^0 = 0.1\,\text{mm}^{-1}$, $\tilde{\mu}_{s1}^0 = 1.0\,\text{mm}^{-1}$, and $\tilde{g}_1^0 = 0.72$. The results from this computation are $\tilde{\mu}_{a1} = 0.1314\,\text{mm}^{-1}$ (9.5% error), $\tilde{\mu}_{s1} = 1.2376\,\text{mm}^{-1}$ (24.72% error), and $\tilde{g}_1 = 0.7185$ (10.19% error).

Across both of these rather different cases, we find that using the convolution model for relatively small source-detector separations yields recovered epithelial optical properties with less than 25% error overall. Although the boundary layer correction requires solution of the one dimensional radiative transport equation (3.63), that equation is readily solved. Consequently, this convolution model is fast to evaluate allowing for the efficient recovery of optical properties.

We have modified our result for the diffuse reflectance calculated using the corrected diffusion approximation to obtain a more accurate model that takes into account layered tissues and larger absorption coefficients. This model is given as a simple convolution with an explicit kernel. This model produces an accurate approximation for the diffuse reflectance, especially for small source-detector separation distances. Moreover, it is extremely fast to implement. Thus, it is useful for modeling the diffuse reflectance close to the source and estimating the scattering properties of superficial depths of a turbid medium.

Chapter 4

Corrected Diffusion Approximation for an Obliquely Incident Beam

To apply the CDA appropriately for detecting early stage cancer cells, we must study the epithelial layer. We derive a model for reflectance due to an obliquely incident beam by extending the analysis used for CDA in Chapters 3 and 4. Through this break in axi-symmetry, we can better examine the epithelial layer through our boundary layer solution. The boundary layer solution contains full angular dependence and is contained in the epithelial layer, thus changes due to this break in axisymmetry are primarily measured from the boundary layer. We study the two-layer tissue problem with a thin slab, representing the epithelium, above a semi-infinite half space, representing the stroma. Below we will show the analysis for an obliquely incident beam on a semi-infinite half space, and then extend the analysis to the two layered tissue system used in Chapter 3. We validate the reflectance computation due to an obliquely incident beam with Monte Carlo simulations, and then use the same Monte Carlo data to determine optical properties of the epithelial layer for specified angles using the convolution form of our reflectance due to an obliquely incident beam for CDA. We also examine the spatial shift in the peak of our reflectance data with respect to the optical properties of the tissue layers, and use it to determine the scattering coefficient of the epithelium.

4.1 Formulation of the Oblique Problem for a Semi-Infinite Half Space

We solve the same RTE (2.1), with the top boundary condition modified for an obliquely incident beam. We seek the solution satisfying

$$\mu\partial_z I + \sqrt{1-\mu^2}(\cos\varphi\partial_x I + \sin\varphi\partial_y I) + \mu_a I + \mu_s L I = 0, \quad \text{in } 0 < z, \tag{4.1}$$

$$I(\mu,\varphi,x,y,0) - r(\mu)I(-\mu,\varphi,x,y,0) = \delta(\mu-\mu_0)\delta(\varphi-\varphi_0)f^o(x,y), \quad \text{on } 0 < \mu \leq 1, \tag{4.2}$$

where

$$f^o(x,y) = \frac{F_0}{2\pi w^2}\exp\left(\frac{-(x^2\mu_0^2+y^2)}{2w^2}\right). \tag{4.3}$$

In (4.3), $\mu_0 = \cos\theta_0$ where θ_0 is the angle with respect to normal, and normal is $\theta = 0$. Note that (4.2) has changed to include a δ-function in φ due to the break in axisymmetry. For a normally incident beam this was not necessary due to the axisymmetry; however, for an obliquely incident beam the choice of azimuthal angle defines the axis along which the symmetry is broken. For our purposes we select $\varphi_0 = 0$ to correspond with the x-axis to exhibit the break in axisymmetry. Using the same scaling with respect to the beam width, $\mathbf{r} = w\bar{\mathbf{r}}$, defined in (2.7), we obtain

$$\beta\mu\partial_{\bar{z}}\bar{I} + \beta\sqrt{1-\mu^2}(\cos\varphi\partial_{\bar{x}}\bar{I} + \sin\varphi\partial_{\bar{y}}\bar{I}) + \alpha\bar{I} + L\bar{I} = 0, \tag{4.4}$$

$$\bar{I}(\mu,\varphi,\bar{x},\bar{y},0) - r(\mu)\bar{I}(-\mu,\varphi,\bar{x},\bar{y},0) = \delta(\mu-\mu_0)\delta(\varphi-\varphi_0)\bar{f}^o(\bar{x},\bar{y}). \tag{4.5}$$

In (4.4), $\alpha = \mu_a/\mu_s$ and $\beta = 1/(w\mu_s)$. Again, we assume $\mu_s \gg \mu_a$ and $w\mu_s \gg 1$, thus $\alpha \ll 1$ and $\beta \ll 1$. Furthermore, we assume $\alpha \ll \beta$. We seek solution to this system as $\bar{I} = \bar{\Psi} + \bar{\Phi}$, where $\bar{\Psi}$ is the boundary layer solution and $\bar{\Phi}$ is the interior solution, as before.

4.1.1 Interior Solution

Substituting $\bar{\Phi} \sim \sum_{n=0}^{\infty} \beta^n \bar{\phi}_n$ in the limit as $\beta \to 0^+$ and collecting like-powers of β, we find to $O(1)$ that

$$L\bar{\phi}_0 = 0, \tag{4.6}$$

and to $O(\beta)$ that

$$L\bar{\phi}_1 = -\mu\partial_{\bar{z}}\bar{\phi}_0 - \sqrt{1-\mu^2}(\cos\varphi\partial_{\bar{x}}\bar{\phi}_0 + \sin\varphi\partial_{\bar{y}}\bar{\phi}_0). \tag{4.7}$$

As in (2.11) - (2.13) we find that $\bar{\phi}_0 = \bar{\phi}_0(\mathbf{r})$, and that

$$\bar{\phi}_1 = -1/(1-g)\hat{\mathbf{s}}\cdot\nabla\bar{\phi}_0. \tag{4.8}$$

We determine the governing equation for $\bar{\phi}_0$ from the $O(\beta^2)$ equation, which yields the diffusion equation:

$$\nabla\cdot\left(\frac{1}{3(1-g)}\nabla\bar{\phi}_0\right) - \frac{\alpha}{\beta^2}\bar{\phi}_0 = 0. \tag{4.9}$$

Thus,

$$\bar{\Phi} = \bar{\phi}_0 - \frac{1}{(1-g)}\hat{\mathbf{s}}\cdot\nabla\bar{\phi}_0 + O(\beta^2) + O(\alpha) \tag{4.10}$$

Upon redimensionalizing (4.10), and dropping the subscript "0", we obtain

$$\Phi \approx \phi - 3\kappa\hat{\mathbf{s}}\cdot\nabla\phi, \quad \text{where } \kappa = 1/(3\mu_s(1-g)). \tag{4.11}$$

where ϕ satisfies

$$\nabla\cdot[\kappa\nabla\phi(\mathbf{r})] - \mu_a\phi(\mathbf{r}) = 0, \quad 0 < z. \tag{4.12}$$

To derive a modified boundary condition for (4.12), we must determine the form of our boundary layer solution.

4.1.2 Boundary Layer Solution

Applying the same analysis used to obtain (2.18) - (2.20), we arrive at the following equations governing the redimensionalized boundary layer solution

$$\mu\partial_z\psi_0 + \mu_s L\psi_0 = 0, \tag{4.13}$$

$$\mu\partial_z\psi_1 + \mu_s L\psi_1 = -\sqrt{1-\mu^2}(\cos\varphi\partial_x\psi_0 + \sin\varphi\partial_y\psi_0), \tag{4.14}$$

We use (4.2) and (4.11) to determine the boundary conditions for ψ_0 and ψ_1:

$$\begin{aligned}\psi_0(\mu,\varphi,x,y,0) - r(\mu)\psi_0(-\mu,\varphi,x,y,0) &= \delta(\mu-\mu_0)\delta(\varphi-\varphi_0)f^o(x,y)\\ &\quad - [1-r(\mu)]\phi(x,y,0), \quad \text{on } 0<\mu\le 1,\end{aligned} \tag{4.15}$$

and

$$\begin{aligned}&\psi_1(\mu,\varphi,x,y,0) - r(\mu)\psi_1(-\mu,\varphi,x,y,0) = 3\kappa([1+r(\mu)]\mu\partial_z\phi(x,y,0)\\ &\quad + [1-r(\mu)]\sqrt{1-\mu^2}(\cos\varphi\partial_x\phi(x,y,0) + \sin\varphi\partial_y\phi(x,y,0))), \quad \text{on } 0<\mu\le 1.\end{aligned} \tag{4.16}$$

We cannot integrate out the φ-dependence as we did previously since (4.2) is not axisymmetric. Hence, we must consider the dependence on φ in what follows. We write ψ_0 and ψ_1 as Fourier series in φ:

$$\psi_0(\mu,\varphi,x,y,z) = \sum_{m=-\infty}^{\infty} a_m(\mu,x,y,z)e^{im\varphi}, \tag{4.17}$$

$$\psi_1(\mu,\varphi,x,y,z) = \sum_{m=-\infty}^{\infty} b_m(\mu,x,y,z)e^{im\varphi}. \tag{4.18}$$

The coefficients a_m and b_m are determined as

$$a_m(\mu,x,y,z) = \frac{1}{2\pi}\int_{-\pi}^{\pi}\psi_0(\mu,\varphi,x,y,z)e^{-im\varphi}d\varphi, \tag{4.19}$$

$$b_m(\mu,x,y,z) = \frac{1}{2\pi}\int_{-\pi}^{\pi}\psi_1(\mu,\varphi,x,y,z)e^{-im\varphi}d\varphi. \tag{4.20}$$

It is important to note here that we seek to compute diffuse reflectance, which is computed through

$$R(x,y) = \int_{-\pi}^{\pi}\int_{-1}^{1} I(\mu,\varphi,x,y,0)t(\mu)\mu d\mu d\varphi. \tag{4.21}$$

Consequently, the contribution of the boundary layer solution to $R(x,y)$ is solely due to $a_0(\mu,x,y,z)$ and $b_0(\mu,x,y,z)$. Thus, we need only compute a_0 and b_0 below. However, we show that a_0 and b_0 are coupled to $a_{\pm1}$ in the analysis which follows.

We solve for coefficients a_m and b_m through substituting equations (4.17) and (4.18) into (4.15) and (4.16), respectively, multiplying through by $e^{-im\varphi}$, and integrating with

respect to φ. By doing so, we obtain

$$a_m(\mu,x,y,0)-r(\mu)a_m(-\mu,x,y,0)=\frac{1}{2\pi}\delta(\mu-\mu_0)f^o(x,y)e^{-im\varphi_0} - \delta_{m,0}[1-r(\mu)]\phi(x,y,0), \quad \text{on } 0<\mu\leq 1, \quad (4.22)$$

and

$$b_m(\mu,x,y,0)-r(\mu)b_m(-\mu,x,y,0)=\frac{1}{2\pi}\int_{-\pi}^{\pi}e^{-im\varphi}3\kappa\Big([1+r(\mu)]\mu\partial_z\phi(x,y,0) + [1-r(\mu)]\sqrt{1-\mu^2}(\cos\varphi\partial_x\phi(x,y,0)+\sin\varphi\partial_y\phi(x,y,0))\Big)d\varphi. \quad (4.23)$$

We simplify (4.23) using $\cos\varphi=(1/2)\left(e^{i\varphi}+e^{-i\varphi}\right)$ and $\sin\varphi=(1/(2i))\left(e^{i\varphi}-e^{-i\varphi}\right)$ yielding

$$b_m(\mu,x,y,0)-r(\mu)b_m(-\mu,x,y,z)=3\kappa\delta_{m,0}[1+r(\mu)]\mu\partial_z\phi(x,y,0) + 3\kappa[1-r(\mu)]\sqrt{1-\mu^2}\left(\frac{1}{2}\left(\delta_{m,1}+\delta_{m,-1}\right)\partial_x\phi(x,y,0)+\frac{1}{2i}\left(\delta_{m,1}-\delta_{m,-1}\right)\partial_y\phi(x,y,0)\right). \quad (4.24)$$

By substituting (4.17) into (4.13) and integrating with respect to φ, we find that

$$\mu\partial_z a_m(\mu,x,y,z)+\mu_s\bar{L}_m a_m(\mu,x,y,z)=0, \quad (4.25)$$

where

$$\bar{L}_m a_m(\mu,x,y,z)=a_m(\mu,x,y,z)-\int_{-1}^{1}p_m(\mu,\mu')a_m(\mu',x,y,z)d\mu'. \quad (4.26)$$

Here, $p_m(\mu,\mu')$ is defined as

$$p_m(\mu,\mu')=\frac{1}{2\pi}\int_{-\pi}^{\pi}p(\mu,\mu',\varphi-\varphi')e^{-im(\varphi-\varphi')}d(\varphi-\varphi'). \quad (4.27)$$

By substituting (4.17) and (4.18) into (4.14), we obtain

$$\mu\partial_z b_m(\mu,x,y,z)+\mu_s\bar{L}_m b_m(\mu,x,y,z)= \frac{1}{2\pi}\int_{-\pi}^{\pi}e^{-im\varphi}\sqrt{1-\mu^2}\Big(\cos\varphi\partial_x\sum_{m'=-\infty}^{\infty}a_{m'}(\mu,x,y,z)e^{im'\varphi} + \sin\varphi\partial_y\sum_{m'=-\infty}^{\infty}a_{m'}(\mu,x,y,z)e^{im'\varphi}\Big)d\varphi, \quad (4.28)$$

We simplify (4.28) by replacing $\cos\varphi=(1/2)\left(e^{i\varphi}+e^{-i\varphi}\right)$ and $\sin\varphi=(1/(2i))\left(e^{i\varphi}-e^{-i\varphi}\right)$

yielding

$$\mu\partial_z b_m(\mu,x,y,z)+\mu_s\bar{L}_m b_m(\mu,x,y,z)= \\ \sqrt{1-\mu^2}\left(\frac{1}{2}(\partial_x a_{m-1}+\partial_x a_{m+1})+\frac{1}{2i}(\partial_y a_{m-1}-\partial_y a_{m+1})\right). \quad (4.29)$$

To solve for ψ_0 and ψ_1 we use the Green's function which we compute in the same manner as in (B.18) with plane wave solutions. To compute a_0, we solve (4.25) subject to (4.22) with $m=0$. According to (4.29), to compute b_0, we need $a_{\pm1}$. To solve for $a_{\pm1}$, we solve (4.25) subject to (4.22) with $m=\pm1$, respectively. Upon computing $a_{\pm1}$, we compute b_0 by solving (4.29) subject to (4.24) with $m=0$. Consequently, we will need Green's functions for these problems which we discuss below.

4.1.3 Green's Functions

We seek the Green's functions, G_m, satisfying

$$\mu\partial_z G_m+\mu_s\bar{L}_m G_m=\delta(\mu-\mu')\delta(z-z'), \quad (4.30)$$

$$G_m(\mu,0;\mu',z')-r(\mu)G_m(-\mu,0;\mu',z')=0, \quad (4.31)$$

$$\bar{L}_m G_m=G_m-\int_{-1}^{1}p_m(\mu,\mu')G_m(\mu',x,y,z)d\mu' \quad (4.32)$$

for $m=0,\pm1$. We solve for G_m by seeking plane wave solutions resulting in the same form as (B.18) for each m. We then use the respective G_m to compute a_0, a_1, a_{-1}, and b_0 explicitly.

Upon computing G_0, we compute a_0 by evaluating

$$a_0(\mu,x,y,z)=\frac{\mu_0}{2\pi}G_0(\mu,z;\mu_0,0^+)f^o(x,y)-\int_0^1\mu' G_0(\mu,z;\mu',0^+)[1-r(\mu')]\phi(x,y,0)d\mu'. \quad (4.33)$$

Similarly, upon computing $G_{\pm1}$, we compute $a_{\pm1}$ by evaluating

$$a_1(\mu,x,y,z)=\frac{\mu_0}{2\pi}G_1(\mu,z,\mu_0,0^+)f^o(x,y)e^{-i\varphi_0}, \quad (4.34)$$

and

$$a_{-1}(\mu,x,y,z)=\frac{\mu_0}{2\pi}G_{-1}(\mu,z;\mu_0,0^+)f^o(x,y)e^{i\varphi_0}, \quad (4.35)$$

respectively. Note that, given the form of G_m and the φ terms in (4.34) and (4.35), $a_{-1}=a_1^*$. Given G_0 and $a_{\pm1}$, we compute b_0 through evaluation of

$$b_0(\mu,x,y,z)=\int_0^1\mu' G_0(\mu,z;\mu',0^+)[1+r(\mu')]3\kappa\mu'\partial_z\phi(x,y,0)d\mu' \\ +\int_{-1}^1\int_0^\infty G_0(\mu,z;\mu',z')\left(-\sqrt{1-\mu'^2}\frac{1}{2}\left[\left(\frac{\partial a_{-1}}{\partial x}+\frac{\partial a_1}{\partial x}\right)+\frac{1}{i}\left(\frac{\partial a_{-1}}{\partial y}-\frac{\partial a_1}{\partial y}\right)\right]\right)dz'd\mu', \quad (4.36)$$

To compute (4.36) we must evaluate the partial derivatives of a_1 and a_{-1}.

$$\partial_x a_1 = \partial_x f^o(x,y)\frac{\mu_0}{2\pi}G_1(\mu,z;\mu_0,0^+)e^{-i\varphi_0}, \tag{4.37}$$

$$\partial_y a_1 = \partial_y f^o(x,y)\frac{\mu_0}{2\pi}G_1(\mu,z;\mu_0,0^+)e^{-i\varphi_0}, \tag{4.38}$$

Note that $\partial_x a_{-1} = \partial_x a_1^*$, and $\partial_y a_{-1} = \partial_y a_1^*$. We simplify the forms of $\partial_x a_1$ and $\partial_y a_1$ in (4.36) by expanding $e^{i\varphi_0} = \cos\varphi_0 + i\sin\varphi_0$, and using the fact that $G_{-1} = G_1^*$ through the representation of $G_1 = \mathrm{Re}[G_1] + i\mathrm{Im}[G_1]$. In doing so, we find that

$$\partial_x a_{-1} + \partial_x a_1 = \partial_x f^o(x,y)\frac{\mu_0}{2\pi}(2\mathrm{Re}[G_1]\cos\varphi_0 + 2\mathrm{Im}[G_1]\sin\varphi_0). \tag{4.39}$$

Similarly, we find that

$$\partial_y a_{-1} - \partial_y a_1 = \partial_y f^o(x,y)\frac{\mu_0}{2\pi}(-2i\cos\varphi_0\mathrm{Im}[G_1] + 2i\sin\varphi_0\mathrm{Re}[G_1]). \tag{4.40}$$

Note that (4.39) is purely real, and (4.40) is purely imaginary. Thus, when substituted back into (4.36), we find that all terms are real. It follows that b_0 is given by

$$\begin{aligned} b_0(\mu,x,y,z) = &\int_0^1 \mu' G_0(\mu,z;\mu',0^+)[1+r(\mu')]3\kappa\mu'\partial_z\phi(x,y,0)d\mu' \\ &- \frac{\mu_0}{2\pi}\int_{-1}^1\int_0^\infty G_0(\mu,z;\mu',z')\sqrt{1-\mu'^2}[(\cos\varphi_0\mathrm{Re}[G_1] + \sin\varphi_0\mathrm{Im}[G_1])\,\partial_x f^o(x,y) \\ &+ (\sin\varphi_0\mathrm{Re}[G_1] - \cos\varphi_0\mathrm{Im}[G_1])\,\partial_y f^o(x,y)]dz'd\mu'. \end{aligned} \tag{4.41}$$

4.1.4 Diffuse Reflectance

We now have a_0 and b_0 which are needed to compute the boundary layer solution's contribution to the diffuse reflectance. To compute a boundary condition for ϕ, we impose the asymptotic matching condition that Ψ must vanish outside the boundary layer. For boundary condition (4.22) with $m = 0$, we apply the projection operator defined in (2.23) to (4.22) and set that result equal to zero. Doing so is sufficient to ensure $a_0 \to 0$ as $z \to \infty$, and yields

$$a\phi(x,y,0) - cf^o(x,y) = 0, \tag{4.42}$$

where

$$a = P[1 - r(\mu)], \tag{4.43}$$

$$c = \frac{\mu_0}{2\pi}G_0(\mu,0;\mu_0,0). \tag{4.44}$$

For b_0, we must also consider terms in (4.41) involving $\mathrm{Re}[G_1]$ and $\mathrm{Im}[G_1]$. Specifically, we must ensure that those terms vanish as $z \to \infty$. Hence, we introduce the operator P_f which maps an interior source to the constant solution. In terms of the plane wave solutions, P_f is defined as

$$P_f[Q(\mu,z)] = \int_{-1}^1 [U_1(\mu') + \sum_{k>0} c_{1k}V_k(\mu')]\int_0^\infty e^{-\lambda_1 z'}Q(\mu',z')dz'd\mu', \tag{4.45}$$

Thus, to ensure that $b_0 \to 0$ as $z \to \infty$, we set

$$b\partial_z\phi(x,y,0) + d_1\partial_x f^o(x,y) + d_2\partial_y f^o(x,y) = 0, \tag{4.46}$$

where

$$b = P[3\kappa\mu(1+r(\mu))], \tag{4.47}$$

$$d_1 = -\frac{\mu_0}{2\pi}P_f[(\cos\varphi_0\sqrt{1-\mu^2}\mathrm{Re}[G_1(\mu,0;\mu_0,z] + \sin\varphi_0\sqrt{1-\mu^2}\mathrm{Im}[G_1(\mu,0;\mu_0,z)])], \tag{4.48}$$

$$d_2 = -\frac{\mu_0}{2\pi}P_f[(\sin\varphi_0\sqrt{1-\mu^2}\mathrm{Re}[G_1(\mu,0;\mu_0,z)] - \cos\varphi_0\sqrt{1-\mu^2}\mathrm{Im}[G_1(\mu,0;\mu_0,z)])]. \tag{4.49}$$

Combining our results for a_0 and b_0, we arrive at our boundary condition for ϕ:

$$a\phi - b\partial_z\phi = cf^o(x,y) + d_1\partial_x f^o(x,y) + d_2\partial_y f^o(x,y), \quad \text{at } z = 0. \tag{4.50}$$

We solve the diffusion equation in (4.12) for ϕ by taking Fourier transforms $(x,y) \to (\xi,\eta)$.

$$\kappa(-\xi^2-\eta^2)\hat{\phi} + \kappa\partial_z^2\hat{\phi} - \mu_a\hat{\phi} = 0, \tag{4.51}$$

We apply the same form of exponential decay in z as before, which when substituted into (4.51) determines the decay rate, k_z, to be

$$k_z = \sqrt{\frac{\mu_a}{\kappa} + \xi^2 + \eta^2}, \tag{4.52}$$

We apply same Fourier transforms $(x,y) \to (\xi,\eta)$, and substitute ∂_z with k_z into the boundary condition (4.50) resulting in

$$a\hat{\phi} + bk_z\hat{\phi} = c\hat{f}^o(\xi,\eta) + i\xi d_1\hat{f}^o(\xi,\eta) + i\eta d_2\hat{f}^o(\xi,\eta), \tag{4.53}$$

We solve (4.53) for $\hat{\phi}$ algebraically, and then take inverse Fourier transforms $(\xi,\eta) \to (x,y)$ to determine the interior solution

$$\phi(x,y,z) = \iint \frac{c\hat{f}^o(\xi,\eta) + i\xi d_1\hat{f}^o(\xi,\eta) + i\eta d_2\hat{f}^o(\xi,\eta)}{a+bk_z}e^{i\xi x + i\eta y}d\xi d\eta, \tag{4.54}$$

Similarly, we determine that

$$\partial_z\phi(x,y,z) = \iint \frac{-k_z(c\hat{f}^o(\xi,\eta) + i\xi d_1\hat{f}^o(\xi,\eta) + i\eta d_2\hat{f}^o(\xi,\eta))}{a+bk_z}e^{i\xi x + i\eta y}d\xi d\eta. \tag{4.55}$$

We compute the boundary layer solution through evaluation of Ψ. Due to the form of each a_m and b_m, we can write Ψ on $z = 0$ in terms of ϕ and $f^o(x,y)$,

$$\bar{\Psi}(\mu,x,y,0) = H_1 f^o(x,y) - H_2\phi(x,y,0) + H_3\partial_z\phi(x,y,0) + H_4\partial_x f^o(x,y) + H_5\partial_y f^o(x,y), \tag{4.56}$$

In the computation of the radiance H_1, H_4, and H_5 have nontrivial dependence on φ; however, as we are computing the reflectance we need only compute the $m = 0$ terms of Ψ. Thus H_1, H_4, and H_5 are written as functions which contain no φ dependence,

and thus $\bar{\Psi}$ in (4.56) is the azimuthally averaged Ψ. We find that

$$H_1(\mu) = \frac{\mu_0}{2\pi} G_0(\mu, 0; \mu_0, 0), \tag{4.57}$$

$$H_2(\mu) = \int_0^1 \mu' G_0(\mu, 0; \mu', 0^+)[1 - r(\mu')]d\mu', \tag{4.58}$$

$$H_3(\mu) = 3\kappa \int_0^1 \mu'^2 G_0(\mu, 0; \mu', 0^+)[1 + r(\mu')]d\mu', \tag{4.59}$$

$$H_4(\mu) = -\frac{\mu_0}{2\pi} \int_{-1}^1 \int_0^\infty G_0(\mu, 0; \mu', z')\sqrt{1-\mu'^2}\Bigg(\frac{\mu_0}{4\pi}\Big(G_{-1}(\mu', z'; \mu_0, 0^+)e^{i\varphi_0} + G_1(\mu', z'; \mu_0, 0)e^{-i\varphi_0}\Big)\Bigg)dz'd\mu', \tag{4.60}$$

$$H_5(\mu) = -\frac{\mu_0}{2\pi} \int_{-1}^1 \int_0^\infty G_0(\mu, 0; \mu', z')\sqrt{1-\mu'^2}\Bigg(\frac{\mu_0}{4\pi i}\Big(G_{-1}(\mu', z'; \mu_0, 0^+)e^{i\varphi_0} - G_1(\mu', z'; \mu_0, 0^+)e^{-i\varphi_0}\Big)\Bigg)dz'd\mu'. \tag{4.61}$$

Combining the results for $\bar{\Psi}$ and Φ, $\bar{I} = \bar{\Psi} + \Phi$ at the boundary $z = 0$ is given by

$$\bar{I}(\mu, x, y, 0) = H_1 f^o(x, y) + [1 - H_2]\phi(x, y, 0) + [H_3 - 3\kappa\mu]\partial_z\phi(x, y, 0) + H_4\partial_x f^o(x, y) + H_5\partial_y f^o(x, y), \tag{4.62}$$

Integration to determine reflectance yields

$$R(x, y) = R_1 f^o(x, y) + R_2\phi(x, y, 0) + R_3\partial_z\phi(x, y, 0) + R_4\partial_x f^o(x, y) + R_5\partial_y f^o(x, y), \tag{4.63}$$

$$R_1 = -2\pi \int_{-1}^{-\mu_{NA}} t(\mu)H_1(\mu)\mu d\mu, \tag{4.64}$$

$$R_2 = -2\pi \int_{-1}^{-\mu_{NA}} t(\mu)[1 - H_2(\mu)]\mu d\mu, \tag{4.65}$$

$$R_3 = -2\pi \int_{-1}^{-\mu_{NA}} t(\mu)[H_3(\mu) - 3\kappa\mu]\mu d\mu, \tag{4.66}$$

$$R_4 = -2\pi \int_{-1}^{-\mu_{NA}} t(\mu)H_4(\mu)\mu d\mu, \tag{4.67}$$

$$R_5 = -2\pi \int_{-1}^{-\mu_{NA}} t(\mu)H_5(\mu)\mu d\mu. \tag{4.68}$$

In these, $t(\mu)$ is the transmission coefficient due to the relative refractive index exiting the medium. Again, we can represent this reflectance as a convolution of an explicit kernel with the incident beam profile,

$$R = K * f^o, \tag{4.69}$$

$$\hat{K} = R_1 + R_2\left(\frac{c + i\xi d_1 + i\eta d_2}{a + bk_z}\right) + R_3\left(\frac{-k_z(c + i\xi d_1 + i\eta d_2)}{a + bk_z}\right) + i\xi R_4 + i\eta R_5, \quad (4.70)$$

4.2 Extension to Layered Tissue System

We must extend this analysis to a layered tissue system to study the diffuse reflectance due to epithelial tissues. Thus we perform the same analysis as above for the system:

$$\mu\partial_z I_1 + \sqrt{1-\mu^2}(\cos\varphi\partial_x I_1 + \sin\varphi\partial_y I_1) + \mu_{a1} I_1 + \mu_{s1} L_1 I_1 = 0, \quad \text{in } 0 < z < z_0, \quad (4.71)$$

$$\mu\partial_z I_2 + \sqrt{1-\mu^2}(\cos\varphi\partial_x I_2 + \sin\varphi\partial_y I_2) + \mu_{a2} I_2 + \mu_{s2} L_2 I_2 = 0, \quad \text{in } z_0 < z, \quad (4.72)$$

$$I_1(\mu,\varphi,x,y,0) - r(\mu) I_1(-\mu,\varphi,x,y,0) = \delta(\mu-\mu_0)\delta(\varphi-\varphi_0) f^o(x,y), \quad \text{on } 0 < \mu \le 1, \quad (4.73)$$

$$I_1(\mu,\varphi,x,y,z_0) = I_2(\mu,\varphi,x,y,z_0), \quad \text{on } -1 \le \mu \le 1, \ -\pi \le \varphi \le \pi, \quad (4.74)$$

$$I_2(\mu,\varphi,x,y,z) \to 0, \quad \text{as } z \to \infty. \quad (4.75)$$

As discussed in the half space analysis, the boundary layer solution is designed to decay to zero outside the boundary layer, which when redimensionalized is $z = \ell_{s1} = 1/(\mu_{s1})$. This provides two cases, the first of which we used in Chapter 3 where we assumed that the top layer thickness $z_0 > \ell_{s1}$. The second is for the case where $z_0 < \ell_{s1}$ which is possible for tissues with small scattering. However, we found in the previous Chapter that the first case is still rather accurate even for small scattering. Thus, we will continue to use the first case in which we assume that the boundary layer solution has decayed within the top layer. We apply the same analysis as above in (4.4), by rescaling with respect to the beam width and seeking the interior solutions as power series in β. We write $\bar{\Phi} \sim \sum_{n=0}^{\infty} \beta^n \bar{\phi}_n$, and $\bar{I}_2 \sim \sum_{n=0}^{\infty} \beta^n \bar{\mathscr{I}}_n$, in the limit as $\beta \to 0^+$. Following the same analysis used to derive (4.6) - (4.11), we find that the redimensionalized results for Φ and I_2 are

$$\Phi \approx \phi - 3\kappa_1 \hat{\mathbf{s}} \cdot \nabla\phi, \quad (4.76)$$

$$I_2 \approx \mathscr{I} - 3\kappa_2 \hat{\mathbf{s}} \cdot \nabla\mathscr{I}, \quad (4.77)$$

where Φ and $\mathscr{I}$ satisfy

$$\nabla \cdot [\kappa_1 \nabla\phi(\mathbf{r})] - \mu_{a1}\phi(\mathbf{r}) = 0, \quad 0 < z < z_0, \quad (4.78)$$

$$\nabla \cdot [\kappa_2 \nabla\mathscr{I}(\mathbf{r})] - \mu_{a2}\mathscr{I}(\mathbf{r}) = 0, \quad z_0 < z, \quad (4.79)$$

respectively. Computing the boundary layer solution follows exactly the same procedure as used for the half space problem. The only modifications are in the notation for the optical properties, each $\mu_s \to \mu_{s1}$, $\mu_a \to \mu_{a1}$, $\kappa \to \kappa_1$, and $g \to g_1$. As above, we put the boundary layer solution together as $\Psi = a_0 + b_0$ and apply the projection operator to a_0 and b_0 yielding the same boundary condition on ϕ. Consequently, ϕ satisfies the same boundary condition on $z = 0$ given by (4.50). We also define an "interface condition" at $z = z_0$ such that

$$\phi = \mathscr{I}, \quad (4.80)$$

and

$$3\kappa_1 \hat{\mathbf{s}} \cdot \nabla\phi = 3\kappa_2 \hat{\mathbf{s}} \cdot \nabla\mathscr{I}, \quad (4.81)$$

which ensures consistency of our solution at the interface of the top layer and the semi-infinite half space. We solve for ϕ and $\mathscr{I}$ by taking Fourier transforms $(x, y) \to (\xi, \eta)$ and assuming solutions of the form $\hat{\phi} = A(\xi,\eta)e^{-k_{z1}z} + B(\xi,\eta)e^{k_{z1}(z-z_0)}$ and $\hat{\mathscr{I}} = D(\xi,\eta)e^{-k_{z2}(z-z_0)}$. By substituting these forms into equations (4.78) and (4.79) we solve

$$\kappa_1(-\xi^2 - \eta^2 + k_{z1}^2)\hat{\phi} - \mu_{a1}\hat{\phi} = 0, \tag{4.82}$$

and

$$\kappa_2(-\xi^2 - \eta^2 + k_{z2}^2)\hat{\mathscr{I}} - \mu_{a2}\hat{\mathscr{I}} = 0, \tag{4.83}$$

respectively. We solve equations (4.82) and (4.83) for their decay rates in z,

$$k_{z1}^2 = \frac{\mu_{a1}}{\kappa_1} + \xi^2 + \eta^2, \tag{4.84}$$

and

$$k_{z2}^2 = \frac{\mu_{a2}}{\kappa_2} + \xi^2 + \eta^2, \tag{4.85}$$

respectively. We then substitute the forms of $\hat{\phi}$ and $\hat{\mathscr{I}}$ into the interface condition and collect like-powers of β, which we then use to solve for $A(\xi,\eta)$ and $B(\xi,\eta)$. Substituting these forms into (4.80) yields

$$A(\xi,\eta)e^{-k_{z1}z_0} + B(\xi,\eta) = D(\xi,\eta), \tag{4.86}$$

and similarly for (4.81) we have

$$\kappa_1(-k_{z1}A(\xi,\eta)e^{k_{z1}z_0} + k_{z1}B(\xi,\eta)) = -\kappa_2 k_{z2}D(\xi,\eta). \tag{4.87}$$

Solving (4.87) for $D(\xi,\eta)$ and setting it equal to the left side of (4.86) we find

$$B(\xi,\eta) = \chi A(\xi,\eta)e^{k_{z1}z_0}, \tag{4.88}$$

where

$$\chi = \frac{\kappa_1 k_{z1} - \kappa_2 k_{z2}}{\kappa_1 k_{z1} + \kappa_2 k_{z2}} e^{-2k_{z1}z_0}. \tag{4.89}$$

We substitute the form of $\hat{\phi}$ into the boundary condition at $z = 0$ yielding

$$A(\xi,\eta)(a + bk_{z1}) + B(\xi,\eta)e^{-k_{z1}z_0}(a - bk_{z1}) = c\hat{f}^o(\xi,\eta) + i\xi d_1\hat{f}^o(\xi,\eta) + i\eta d_2\hat{f}^o(\xi,\eta). \tag{4.90}$$

Substituting (4.88) into (4.90) yields

$$A(\xi,\eta)(a + bk_{z1}) + \chi A(\xi,\eta)(a - bk_{z1}) = c\hat{f}^o(\xi,\eta) + i\xi d_1\hat{f}^o(\xi,\eta) + i\eta d_2\hat{f}^o(\xi,\eta), \tag{4.91}$$

which can be solved explicitly for $A(\xi,\eta)$,

$$A(\xi,\eta) = \frac{c\hat{f}^o(\xi,\eta) + i\xi d_1\hat{f}^o(\xi,\eta) + i\eta d_2\hat{f}^o(\xi,\eta)}{a(1+\chi) + bk_{z1}(1-\chi)}. \tag{4.92}$$

We substitute (4.92) into the form of $\hat{\phi}$ and take inverse Fourier transforms $(\xi, \eta) \to (x, y)$ to solve for ϕ,

$$\phi(x, y, z) = \iint (A(\xi, \eta)e^{-k_{z1}z} + \chi A(\xi, \eta)e^{k_{z1}z})e^{i\xi x + i\eta y} d\xi d\eta. \tag{4.93}$$

Similarly, we solve for $\partial_z \phi$ to determine the diffuse reflectance of Φ,

$$\partial_z \phi(x, y, z) = \iint (-k_{z1}A(\xi, \eta)e^{-k_{z1}z} + k_{z1}\chi A(\xi, \eta)e^{k_{z1}z})e^{i\xi x + i\eta y} d\xi d\eta. \tag{4.94}$$

To compute diffuse reflectance at the boundary, we combine $\Psi \approx a_0 + b_0$ and $\Phi \approx \phi - 3\kappa_1 \mu \partial_z \phi$. We rewrite Ψ in terms of ϕ and $f^o(x, y)$ as in (4.56),

$$\begin{aligned}\Psi(\mu, x, y, 0) = H_1(\mu)f^o(x, y) - H_2(\mu)\phi(x, y, 0) + H_3(\mu)\partial_z \phi(x, y, 0) + H_4(\mu)\partial_x f^o(x, y) \\ + H_5(\mu)\partial_y f^o(x, y),\end{aligned} \tag{4.95}$$

where H_1-H_5 are given by (4.57)-(4.61).

We then combine Ψ and Φ to form the irradiance at $z = 0$, which is exactly the same as in (4.62) Integrating over the range of angles exiting the medium yields computation of the reflectance given by (4.63)-(4.68). As before, we can rewrite the reflectance as a convolution of an explicit kernel with the incident beam profile.

$$R(x, y) = K * f^o(x, y), \tag{4.96}$$

We take Fourier transforms $(x, y) \to (\xi, \eta)$ and write

$$\hat{K} = R_1 + R_2 \frac{(1+\chi)(c + i\xi d_1 + i\eta d_2)}{a(1+\chi) + b(1-\chi)k_{z1}} + R_3 \frac{-k_{z1}(1-\chi)(c + i\xi d_1 + i\eta d_2)}{a(1+\chi) + b(1-\chi)k_{z1}} + i\xi R_4 + i\eta R_5. \tag{4.97}$$

Using this kernel, we write the diffuse reflectance as

$$\begin{aligned}R(x, y) = \int\int \Big[R_1 + R_2 \frac{(1+\chi)(c + i\xi d_1 + i\eta d_2)}{a(1+\chi) + b(1-\chi)k_{z1}} + R_3 \frac{-k_{z1}(1-\chi)(c + i\xi d_1 + i\eta d_2)}{a(1+\chi) + b(1-\chi)k_{z1}} \\ + i\xi R_4 + i\eta R_5\Big] \hat{f}^o(\xi, \eta)e^{i\xi x + i\eta y} d\xi d\eta.\end{aligned} \tag{4.98}$$

4.3 Comparison with Monte Carlo Simulations

For validation purposes, we compare this model of the diffuse reflectance due to an obliquely incident beam with Monte Carlo simulations for the same conditions. We consider the same optical properties used in the previous Chapter for the convolution model. Specifically, we have taken values for the optical properties from the paper by Kienle *et al.* [30]. In particular, the optical properties of the top, epithelial layer are $\mu_{a1} = 0.02\,\text{mm}^{-1}$, $\mu_{s1} = 6.5\,\text{mm}^{-1}$, and $g_1 = 0.80$. The optical properties of the bottom, stromal layer are $\mu_{a2} = 0.01\,\text{mm}^{-1}$, $\mu_{s2} = 6\,\text{mm}^{-1}$, and $g_2 = 0.80$. The layer thickness is $z_0 = 0.25\,\text{mm}$, and the air-tissue refractive index is set to $n_{rel} = 1.4$. The numerical aperture (NA) is set to NA $= 1$, which corresponds to the full range of μ exiting the medium, $\mu_{NA} = 0$. These properties require us to choose a beam width with

FWHM = 5 mm, denoting the full width at half maximum of the beam, to be consistent with the CDA assumptions.

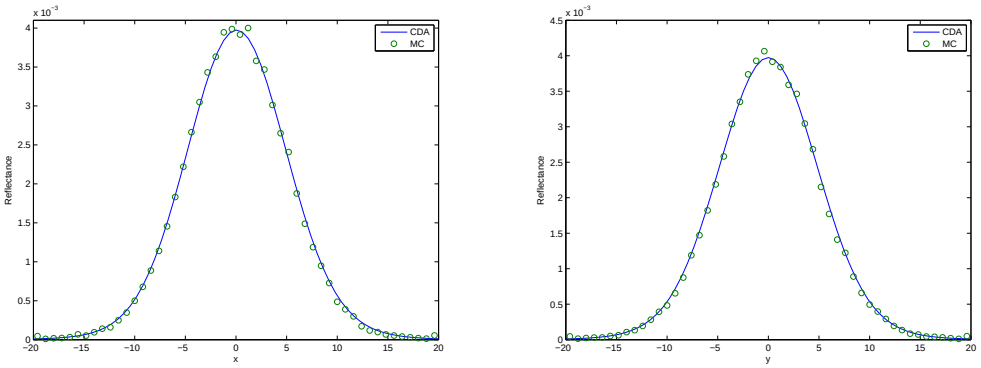

Figure 4.1: Comparison of reflectance measurements due to an obliquely incident beam using the convolution CDA model (solid curve) with Monte Carlo simulations (circle symbols). The plot on the left shows the cross-section of reflectance measured at $y = 0$ for all x, while the right plot shows the reflectance measured at $x = 0$ for all y. The angle of incidence corresponds with $\theta \approx 4.9035$ degrees. The optical properties, taken from Kienle *et al.* [30], for the top layer are $\mu_{a1} = 0.02\,\mathrm{mm}^{-1}$, $\mu_{s1} = 6.5\,\mathrm{mm}^{-1}$, and $g_1 = 0.80$, and the optical properties for the bottom layer are $\mu_{a2} = 0.01\,\mathrm{mm}^{-1}$, $\mu_{s2} = 6\,\mathrm{mm}^{-1}$, and $g_2 = 0.80$. The layer thickness is $z_0 = 0.25\,\mathrm{mm}$, the refractive index is $n_{rel} = 1.4$, and NA = 1.

A comparison of our convolution CDA model for an obliquely incident beam and Monte Carlo simulations for the same are shown in Figures 4.1-4.3. We show the convolution CDA as a solid curve and the Monte Carlo data as circle symbols in each plot. For the Monte Carlo simulations, we used the command line Monte Carlo software available at http://www.virtualphotonics.org with 10^7 photons. As can be seen in Figures 4.1-4.3, the Monte Carlo data agrees well with the convolution model of the diffuse reflectance for small angles. The results agree across the entire domain along both axes, and the only deviation appears at the top of the peak where even Monte Carlo simulations are less accurate[26]. At larger angles, there is deviation in the spread along the x-axis due to the break in axisymmetry. This break in axisymmetry should show a shift along the x-axis in addition to spread in the width of the beam corresponding with the $\sin\theta_0$. This spread is not expressed in the MC data, which is visible through comparison of the two plots along the x and y axes. Thus, for smaller angles where these deviations are minimal we can use MC data to approximate optical properties accurately.

4.4 Computation of Optical Properties

To detect early stage cancer cells, we seek to recover the optical properties of the epithelial layer. In the previous Chapter, we determined optical properties of the epithelial layer by assuming the lower layer is known and matching reflectance data with *lsqnonlin* implemented in MATLAB (Mathworks Inc., Natick, Massachusetts). Here, we investi-

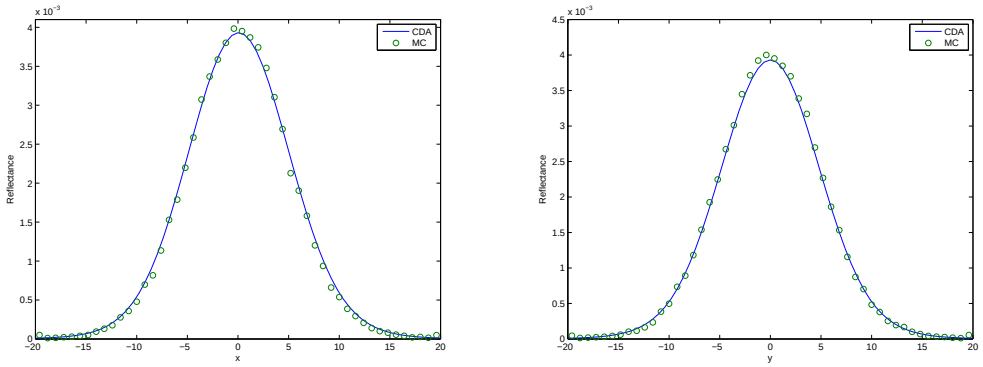

Figure 4.2: The same comparison of reflectance measurements due to an obliquely incident beam using the convolution CDA model (solid curve) with Monte Carlo simulations (circle symbols) as in Fig 4.1. The angle of incidence corresponds with $\theta \approx 13.2631$ degrees. The optical properties, taken from Kienle *et al.* [30], for the top layer are $\mu_{a1} = 0.02\,\mathrm{mm}^{-1}$, $\mu_{s1} = 6.5\,\mathrm{mm}^{-1}$, and $g_1 = 0.80$, and the optical properties for the bottom layer are $\mu_{a2} = 0.01\,\mathrm{mm}^{-1}$, $\mu_{s2} = 6\,\mathrm{mm}^{-1}$, and $g_2 = 0.80$. The layer thickness is $z_0 = 0.25\,\mathrm{mm}$, the refractive index is $n_{rel} = 1.4$, and NA $= 1$.

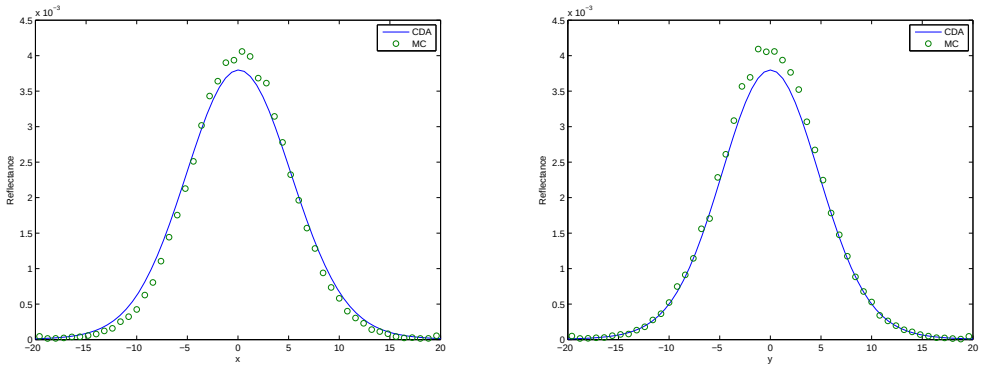

Figure 4.3: The same comparison of reflectance measurements due to an obliquely incident beam using the convolution CDA model (solid curve) with Monte Carlo simulations (circle symbols) as in Fig 4.1. The angle of incidence corresponds with $\theta \approx 24.4224$ degrees. The optical properties, taken from Kienle *et al.* [30], for the top layer are $\mu_{a1} = 0.02\,\mathrm{mm}^{-1}$, $\mu_{s1} = 6.5\,\mathrm{mm}^{-1}$, and $g_1 = 0.80$, and the optical properties for the bottom layer are $\mu_{a2} = 0.01\,\mathrm{mm}^{-1}$, $\mu_{s2} = 6\,\mathrm{mm}^{-1}$, and $g_2 = 0.80$. The layer thickness is $z_0 = 0.25\,\mathrm{mm}$, the refractive index is $n_{rel} = 1.4$, and NA $= 1$.

gate the use of an obliquely incident beam to provide additional information useful in recovering the optical properties of epithelial tissues. As can be seen in Figures 4.1-4.3, applying CDA for an obliquely incident beam matches very well with Monte Carlo simulations. Therefore, we will use CDA to show that using multiple illumination angles may improve the recovery of the optical properties of the epithelium.

As before, we assume *a priori* knowledge of the layer thickness, z_0, relative refractive index, n_{rel}, and the optical properties of the lower layer: μ_{a2}, μ_{s2}, and g_2. The xz-plane is the plane of incidence. For data, we sample the diffuse reflectance along the positive x-axis. In other words, the reflected light which corresponds to the right side of the peaks in Figures 4.1-4.3. The data computed from Monte Carlo simulations is denoted by $R_i = R(x_i, 0)$ for $i = 1, \cdots, N$. Let $\mathbf{d} = (R_1, \cdots, R_N)$ denote a data vector whose entries are these individual diffuse reflectance measurements. Specifically, for the data used in Table 4.1, we used the reflectance data from Monte Carlo simulations at distances $\mathbf{x} = [2\text{mm}, 4.4\text{mm}, 6.8\text{mm}, 9.2\text{mm}, 11.6\text{mm}, 14\text{mm}]$. Given the optical properties of the top layer: μ_{a1}, μ_{s1}, and g_1, we can compute the model vector $\mathbf{m} = (M_1, \cdots, M_N)$ whose entries are evaluations of the convolution model given by (4.98). We seek to estimate the optical properties of the top layer through solution of the nonlinear least-squares problem:

$$\min_{\mu_{a1}, \mu_{s1}, g_1} \frac{1}{2} ||\mathbf{d} - \mathbf{m}||_2^2. \tag{4.99}$$

We apply upper and lower bounds on the epithelial optical properties as in the normally incident case: $10^{-4} \leq \mu_{a1} \leq 1\text{mm}^{-1}$, $10^{-1} \leq \mu_{s1} \leq 10\text{mm}^{-1}$, and $0.70 \leq g_1 \leq 0.99$. This problem is sensitive to the initial guess for these optical properties due to the presence of many local minima. Thus, our initial guess of the epithelial optical properties was selected to be $\tilde{\mu}_{a1}^0 = 0.05\text{mm}^{-1}$, $\tilde{\mu}_{s1}^0 = 2.0\text{mm}^-1$, and $\tilde{g}_1^0 = 0.72$.

Table 4.1: Table of recovered optical properties from Monte Carlo data for a range of small angles and their errors with respect to the actual values. The row labeled 'Average' is taken as the average of values recovered using the three previous oblique angles. The row labeled 'Combined' is found through solving the least-squares system for those same three angles simultaneously.

Angle (degrees)	$\tilde{\mu}_{a1}$	% error	$\tilde{\mu}_{s1}$	% error	$\tilde{g}_1$	% error
0	0.0164	-18.00%	7.7687	19.52%	.7026	-12.17%
7.6871	0.0230	15.00%	6.1088	-6.02%	0.7047	-11.91%
13.2631	0.0268	34.00%	4.5187	-30.48%	0.7082	-11.47%
18.8422	0.0186	-7.00%	7.2611	11.71%	0.7046	-11.92%
Average	0.0228	14.00%	5.9629	-8.26%	0.7058	-11.77%
Combined	0.0286	43.00%	6.5308	0.40%	0.7054	-11.83%
24.4224	0.0479	139.50%	4.4343	-31.78%	0.7109	-11.14%

We compare these results with the computation for the same layered tissue system due to a normally incident beam. For small angles, we compute the optical properties using data along the x-axis and for the first three angles we have good agreement for our computation of all three properties μ_{a1}, μ_{s1}, and g_1. However, we exhibit even better computation of the optical properties by taking the average of these three angles, shown in the row labeled 'Average'. We found that by solving for the properties which satisfy

all three angles simultaneously the value of the absorption coefficient is poor, however there is significant improvement in the computation of the scattering coefficient. The absorption coefficient is not easily recovered from the epithelial layer due to the thickness of the epithelial layer; it is not possible for the light to travel multiple absorption lengths within the top layer and is thus minimally affected by the absorption coefficient and causes its recovery to be inefficient. Additionally, we lose accuracy at larger angles where the MC simulations begin to deviate from our model. For the normally incident case, our error was less than 20% overall. However, by using multiple measurements with small oblique angles we have decreased our overall error to under 15%. This is a significant improvement which provides promising application of oblique angles to determine optical properties of epithelial tissues.

4.5 Comparison of Oblique Shift

In computing reflectance due to an obliquely incident beam, it is important to take note of the work by Wang and Jacques [66]. They developed a model for determining the reduced scattering coefficient and the absorption coefficient of tissues through a relationship between the shift in the reflectance data and the angle of incidence. Their model uses a line source to model a pencil beam, whereas our CDA model uses a Gaussian beam which is necessary to be relatively large to ensure our parameter β is sufficiently small. As a result, it is difficult to make a direct comparison with their results due to the beam differences. Additionally, we have studied small angles whereas their work was used for large angles, around 45 degrees. In their paper they state that the size of the beam is unrestricted for validity of their model, but they do require that the measurements are taken over 1-2 scattering mean free paths outside the beam - thus for a larger beam, these measurements are quite small. Since we cannot directly compare our model of the diffuse reflectance, we will examine this same shift for our beam using CDA due to its agreement with Monte Carlo simulations.

We can extend our analysis of this Δx measurement by varying our optical properties in the top layer and examining the changes in this value. We found that there was minimal change with μ_{a1} and g_1, but when we vary the value of μ_{s1} there is an obvious change in Δx. Additionally, we considered changes in μ_{s2} to ensure that variation due to the scattering coefficients was most heavily dependent on the top layer. In Figures 4.4-4.6 we see a shift in the value of Δx while the general shape of the curve remains the same across angles. These plots show that there is a clear relationship between the scattering coefficient of the top layer and the shift in the peak of the reflectance data. Specifically, as scattering increases the shift, Δx, monotonically decreases. Given the shape of the curves in Figures 4.4-4.6, we can gain insight through fitting these curves on a *log* scale. However, if the scattering coefficient of the lower layer is significantly different from that of the top layer, there is deviation in this value which could become significant. For tissues there is usually a relatively small variation between layers. Thus, there is information which can be extracted from this shift which requires further analysis.

The smoothness and shape of the curve for Δx using the convolution CDA allows us to write a linear fit for the values on a *log* scale. This linear fit defines a relationship between the scattering coefficient, the angle of incidence, and the shift, Δx. The slope and intercept change monotonically with respect to the angle of incidence and the value

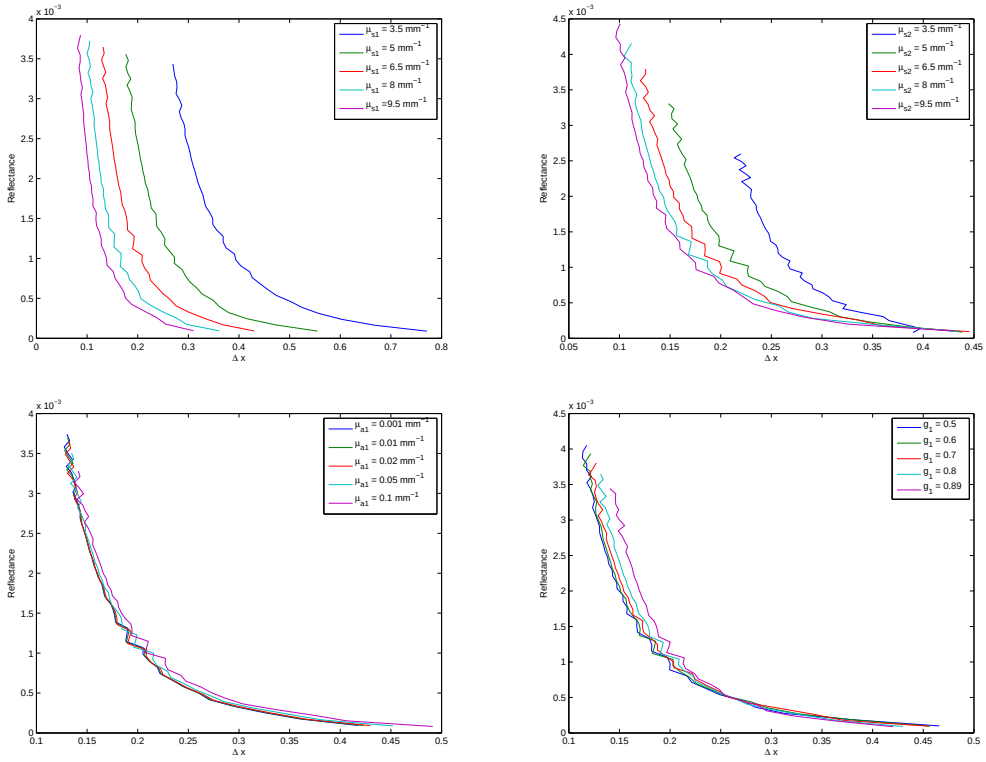

Figure 4.4: The plot on the top left shows the shift, Δx, with respect to the value of the reflectance measured for a range of values of μ_{s1} with all other properties fixed. Specifically $\mu_{a1} = 0.02\text{mm}^{-1}$, $g_1 = 0.8$, $\mu_{a2} = 0.01\text{mm}^{-1}$, $\mu_{s2} = 6.0\text{mm}^{-1}$, and $g_2 = 0.8$. Note the clear shift in Δx as μ_{s1} is increased. The plot on the top right shows the shift, Δx, with respect to the value of the reflectance measured for a range of values of μ_{s2} with all other properties fixed. Specifically, $\mu_{a1} = 0.02\text{mm}^{-1}$, $\mu_{s1} = 6.5\text{mm}^{-1}$, $g_1 = 0.8$, $\mu_{a2} = 0.01\text{mm}^{-1}$, and $g_2 = 0.8$. Note that there is not a clear shift for these modifications, however the max and min for Δx remains quite similar for all values of μ_{s2}. The plot on the bottom left shows the shift, Δx, with respect to the value of the reflectance measured for a range of values of μ_{a1} with all other properties fixed. Specifically, $\mu_{s1} = 6.5\text{mm}^{-1}$, $g_1 = 0.8$, $\mu_{a2} = 0.01\text{mm}^{-1}$, $\mu_{s2} = 6\text{mm}^{-1}$, and $g_2 = 0.8$. Note that there is minimal change in Δx for the range of μ_{a1}. The bottom right plot shows the same for a range of values of g_1 with all other properties fixed. Specifically, $\mu_{a1} = 0.02\text{mm}^{-1}$, $\mu_{s1} = 6.5\text{mm}^{-1}$, $\mu_{a2} = 0.01\text{mm}^{-1}$, $\mu_{s2} = 6\text{mm}^{-1}$, and $g_2 = 0.8$. Again, there is only small modifications to the shift for the range of values. Thus, we can conclude that the shift is most heavily dependent on the value of μ_{s1}. All plots are shown for the oblique angle of $\theta \approx 7.6871$ degrees off normal.

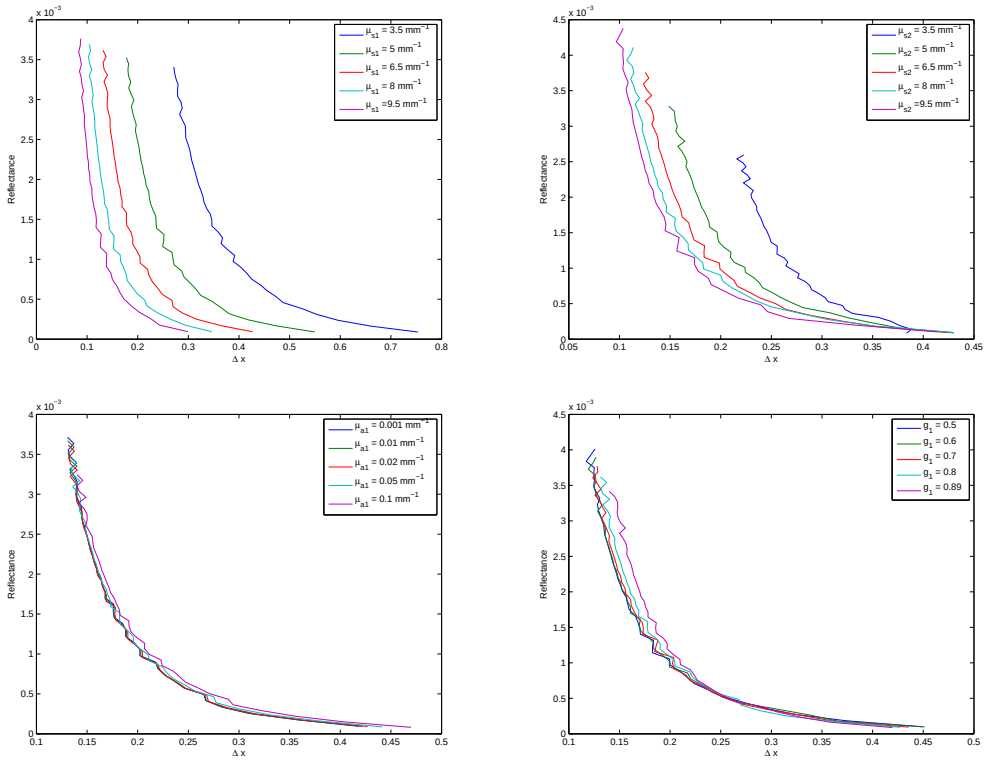

Figure 4.5: These plots are the same as in Figure 4.4, however all plots are shown for the oblique angle of $\theta \approx 13.2631$ degrees off normal. Note that, again there is a clear shift in Δx as μ_{s1} is increased, but not a clear shift for changes in μ_{s2}, μ_{a1}, nor g_1. Thus, we can conclude that the shift is most heavily dependent on the value of μ_{s1}.

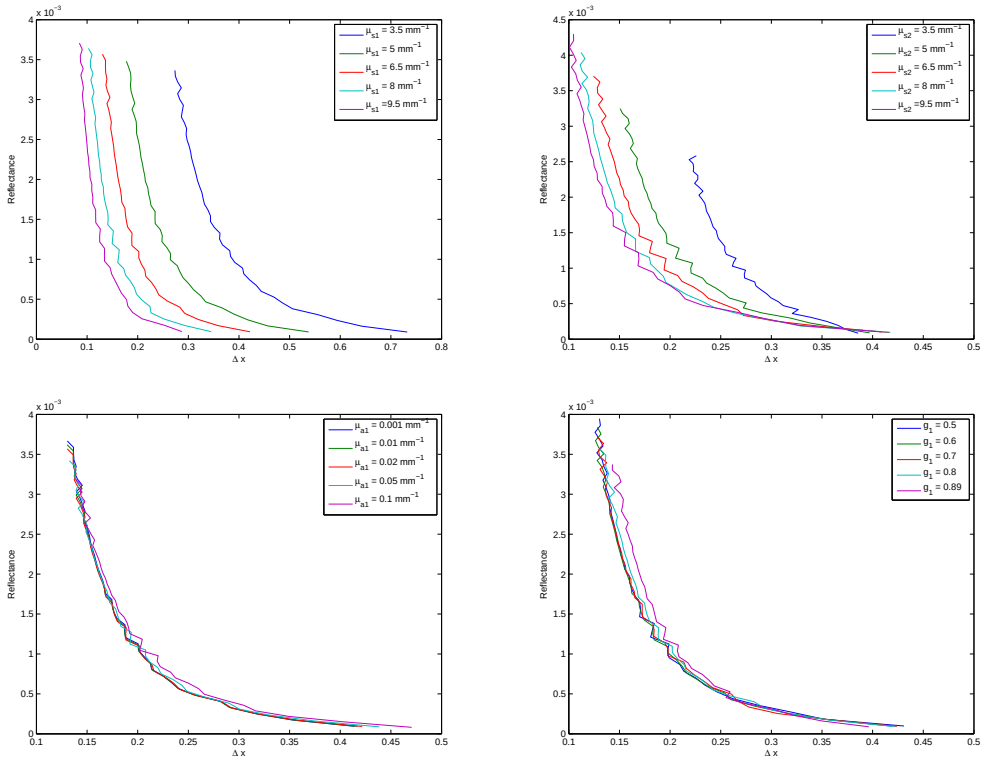

Figure 4.6: These plots are the same as in Figure 4.4, however all plots are shown for the oblique angle of $\theta \approx 18.8422$ degrees off normal. Note that, again there is a clear shift in Δx as μ_{s1} is increased, but not a clear shift for changes in μ_{s2}, μ_{a1}, nor g_1. Thus, we can conclude that the shift is most heavily dependent on the value of μ_{s1}.

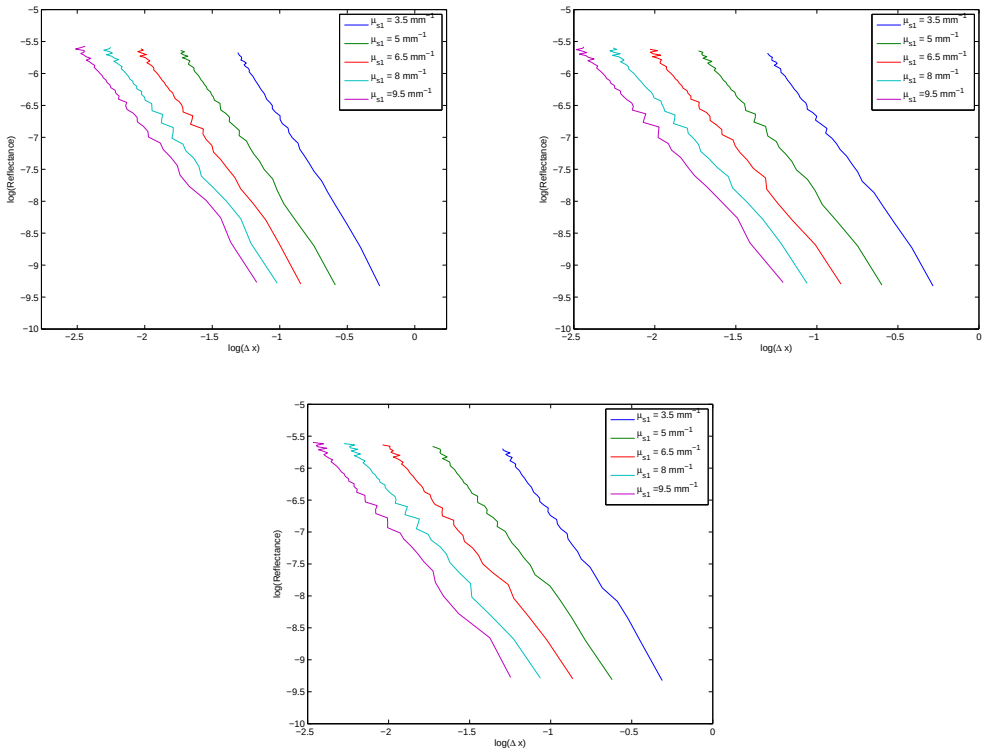

Figure 4.7: Here we show the same comparison as in the top left plots in Figures 4.4 - 4.6, on a *log* scale. Converting to a *log* scale presents us with a linear relationship between the reflectance value and the shift in the peak, Δx. Additionally, this linear relationship changes monotonically with the choice of epithelial scattering coefficient for each angle. This plot is shown for an incident beam at angles of $\theta \approx 7.6871$, 13.2631, and 18.8422 degrees off of normal for top left, top right, and bottom, respectively.

of the scattering coefficient in the top layer. Thus, we can approximate the relationship between these three properties by fitting the slope, $m(\sin\theta_0, \mu_{s1})$, and the intercept, $b(\sin\theta_0, \mu_{s1})$, as planes. We then use the shift in the reflectance for specified angles of incidence to approximate the optical properties of the epithelial layer from these planes. Using the same optical properties and angles shown in 4.7, we formed a planar fit for $m(\sin\theta_0, \mu_{s1})$ and $b(\sin\theta_0, \mu_{s1})$. From these planes we recovered the scattering coefficient of the top layer from the curve for different values of θ_0 and μ_{s1}.

Table 4.2: Table of recovered scattering coefficients from CDA reflectance and shift data for a range of angles and their errors with respect to the actual values. The first three rows correspond to $\mu_{s1} = 7\text{mm}^{-1}$, and the bottom three rows correspond to $\mu_{s1} = 12\text{mm}^{-1}$.

Angle (degrees)	$m : \tilde{\mu}_{s1}$	% error	$b : \tilde{\mu}_{s1}$	% error
7.6871	7.3298	4.71%	7.4498	6.43%
13.2631	7.2621	3.74%	7.4990	7.13%
18.8422	7.5625	8.04%	7.3710	5.30%
7.6871	10.5911	-11.74%	9.7208	-18.99%
13.2631	10.5048	-12.46%	9.9312	-17.24%
18.8422	9.7793	-18.51%	10.5749	-11.88%

The results listed in Table 4.2 show promising accuracy. For the first three rows we recovered scattering coefficients within the same range of the original data which built the planes used, and the error of all approximations was less than 10%. In the bottom three rows we recovered scattering coefficients outside the original range used, thus there is error due to the extrapolation outside the original range which increases the error of our recovery. However, the error of properties recovered is still under 20% which is promising for application and does encourage additional study.

Chapter 5

Concluding remarks and future work

This dissertation work developed, implemented, and extended the corrected diffusion model for diffuse reflectance measurements to study methods for the early detection of cancer in epithelial tissues. The ultimate goal of this work is to improve the accuracy and efficiency of optical imaging techniques through an asymptotic analysis of light propagation in tissues. The corrected diffusion approximation was derived systematically from the radiative transport equation to provide an alternative model which improves upon the diffusion approximation, and is more efficient than the radiative transport equation. We have verified that the corrected diffusion approximation is accurate close to the source, which is relevant due to the connection between reflectance data close to the source and the optical properties of epithelial tissues [30, 1, 60]. This aspect of the corrected diffusion approximation allowed us to recover the optical properties of the epithelial layer from diffuse reflectance measurements.

We determined the scattering coefficient, the anisotropy factor, and the absorption coefficient of the epithelial layer through a least-squares fit to Monte Carlo simulation data governed by the radiative transport equation. In contrast to the diffusion approximation, the corrected diffusion approximation allows for the recovery of the scattering coefficient and the anisotropy factor independently. Additionally, this is distinctive because the corrected diffusion approximation is written as a convolution of an explicit kernel and the incident beam profile, which is substantially more efficient than using the radiative transport equation. Thus, the corrected diffusion approximation has promising applications for determining optical properties of superficial tissues to detect early stage cancer cells.

Additionally, in this dissertation we extended the corrected diffusion approximation to include analysis for an obliquely incident beam. The break in axisymmetry is not entirely accountable in the diffusion approximation. This additional variable allows us to compute optical properties of the epithelial layer for multiple angles with increased accuracy and efficiency. This break in axisymmetry was examined by Jacques and Wang [66], and they introduced a shift which could be traced back to the reduced scattering coefficient of the medium. However, we found that this conclusion was inconsistent with the Monte Carlo simulations run for smaller oblique angles and our relatively large beam width. Their model required that data be used several mean scattering lengths away from the source and outside the beam. Additionally, this was

inconsistent with the corrected diffusion approximation due to the same requirements. However, the corrected diffusion approximation agrees very well with the Monte Carlo simulations for these angles. Thus, we examined this same shift and determined a relationship between the shift and the scattering coefficient of the epithelial layer. This yielded an accurate and efficient means to determine the scattering coefficient directly.

The limitations of this work come from the scaling used in the asymptotic analysis. Due to the small parameter used, $\beta = 1/(w\mu_s)$, it requires that the beam width, w, be sufficiently large to ensure $\beta \ll 1$. Thus, when the scattering coefficient of the medium, μ_s, is small we must increase w sufficiently to ensure consistency of the corrected diffusion approximation. To address this concern, future work will evaluate asymptotic analysis of the radiative transport for a different scaling which ensures that w is also small. However, a large beam is not an invalid source - the analysis completed is experimentally valid. To apply a similar analysis for fiber optic sources we will evaluate the system where w is on the order of the scattering mean-free path, ℓ_s.

Additionally, we examined the analysis of Wang and Jacques [66] for diffusion due to an obliquely incident beam. Their analysis could not be directly compared with our model due to the nature of the beams chosen. However, completing a full analysis of their work is an extremely relevant case for our corrected diffusion approximation because their work is widely accepted and used for the diffusion approximation with an obliquely incident beam. Thus, future work will evaluate the shift found in their work for the same circumstances using the corrected diffusion approximation.

Appendix A

Plane Wave Solutions

We solve the 1-D RTE

$$\mu\partial_\zeta\bar{\psi} + L\bar{\psi} = 0, \tag{A.1}$$

numerically using plane wave solutions of the form

$$\bar{\psi}_n(\mu,\zeta) = e^{\lambda\zeta}V(\mu). \tag{A.2}$$

Upon substituting (A.2) into (A.1), we obtain

$$\lambda\mu V + LV = 0. \tag{A.3}$$

We solve this as a generalized eigenvalue problem numerically. To do this we apply the Discrete Ordinates method [23, 6] using a numerical quadrature for our approximation of the integral in μ contained in L:

$$\int_{-1}^{1} h(\mu,\mu')V(\mu')d\mu' \approx \sum_{m'=1}^{M} h(\mu,\mu_{m'})V(\mu_{m'})w_{m'}. \tag{A.4}$$

In this, $\mu_{m'}$ are the quadrature abscissas, and $w_{m'}$ are the quadrature weights. We use Gauss-Legendre quadrature because it is naturally defined over the interval $[-1,1]$, and when the number of points used is even it excludes the midpoint at $\mu = 0$, which is ill-defined for this problem. Thus, it is a very compatible quadrature rule for this problem. It is also a rather nice rule to implement for this problem because it contains symmetry in its assignments for the quadrature weights and abscissas. This correlates well with the symmetry of the eigenvalue problem, where given the pair $[\lambda, V(\mu)]$ we find that $[-\lambda, V(-\mu)]$ is also a solution to (A.3).

We find an orthogonality relation for our eigenfunctions. Given two plane wave modes which satisfy (A.3), $[\lambda_1, V_1(\mu)]$ and $[\lambda_2, V_2(\mu)]$ we have

$$\lambda_1\mu V_1 + \left(V_1 - \int_{-1}^{1} h(\mu,\mu')V_1(\mu')d\mu'\right) = 0, \tag{A.5}$$

$$\lambda_2\mu V_2 + \left(V_2 - \int_{-1}^{1} h(\mu,\mu')V_2(\mu')d\mu'\right) = 0. \tag{A.6}$$

By multiplying (A.5) by V_2, and (A.6) by V_1, then subtracting the latter from the former

and integrating with respect to μ we obtain the relation

$$(\lambda_1 - \lambda_2)\int_{-1}^{1} \mu V_1(\mu)V_2(\mu)d\mu = \\ \mu_s \int_{-1}^{1}[V_2(\mu)\int_{-1}^{1} h(\mu,\mu')V_1(\mu')d\mu' - V_1(\mu)\int_{-1}^{1} h(\mu,\mu')V_2(\mu')d\mu']d\mu. \quad \text{(A.7)}$$

The right-hand side of (A.7) is identically zero due to the spherical symmetry of our scattering phase function, $h(\mu,\mu') = h(\mu',\mu)$. Thus we arrive at an orthogonality relation for our eigenfunctions, given two distinct eigenvalues λ_1 and λ_2

$$(\lambda_1 - \lambda_2)\int_{-1}^{1} V_1(\mu)V_2(\mu)\mu d\mu = 0. \quad \text{(A.8)}$$

We solve for our plane wave modes evaluated at each quadrature abscissa by substituting the approximation to the integral for L into (A.3). The resulting equation with respect to $V_j(\mu_m) = V_{j,m}$, where j corresponds to the plane wave mode, is

$$\lambda_j \mu_m V_{j,m} + \mu_s V_{j,m} - \mu_s \sum_{m'=1}^{M} h(\mu_m,\mu_{m'})V_{j,m'}w_{m'} = 0. \quad \text{(A.9)}$$

Thus we represent each $V_j(\mu)$ as a vector evaluated at each abscissa in μ. This results in the form

$$\lambda_j V_{j,m} = \mathbf{A}V_{j,m}, \quad \mathbf{A} = \frac{1}{\mu_m}\mu_s\left(\sum_{m'=1}^{M} h(\mu_m,\mu_{m'})V_{j,m'}w_{m'} - 1\right). \quad \text{(A.10)}$$

We solve (A.10) numerically in Matlab. We then order and index the eigenvalues such that

$$\ldots < \lambda_{-j} < \ldots < \lambda_{-1} < \lambda_1 < \ldots < \lambda_j < \ldots \quad \text{(A.11)}$$

This allows us to apply the symmetry mentioned above through

$$\lambda_{-j} = -\lambda_j, \quad V_{-j}(\mu) = V_j(-\mu), \quad \text{for } j = 1, 2, \ldots. \quad \text{(A.12)}$$

Then we normalize our eigenfunctions to ensure the solution is consistent by

$$\int_{-1}^{1} V_j^2(\mu)\mu d\mu = -sgn(j). \quad \text{(A.13)}$$

In terms of plane wave solutions, the solution of (A.1) is given by

$$\bar{\Psi}(\mu_m,\zeta) = \bar{\psi}_m(\zeta) = \sum_{j<0} V_{j,m}a_j e^{\lambda_j\zeta} + \sum_{j>0} V_{j,m}b_j e^{\lambda_j\zeta}, \quad \text{(A.14)}$$

where we solve for the a_j's and b_j's through the boundary conditions. Note the form consistency with [33].

Appendix B

Green's Function Computation

To solve for the Green's function we follow the analysis outlined in [33] and seek solution of

$$\mu\partial_\zeta G + G - \int_{-1}^{1} h(\mu,\mu')G(\mu')d\mu' = \delta(\mu-\mu_0)\delta(\zeta-\zeta'), \tag{B.1}$$

subject to the jump condition at $\zeta = \zeta'$

$$\mu G(\mu,\zeta'+0;\mu',\zeta') - \mu G(\mu,\zeta'-0;\mu',\zeta') = \delta(\mu-\mu'). \tag{B.2}$$

We represent the numerical approximation of $G(\mu,\zeta;\mu',\zeta')$ by $G_{m,m'}(\zeta,\zeta') \approx G(\mu_m,\zeta;\mu_{m'},\zeta')$. We write the jump condition numerically as

$$\mu_n G_{n,n'}(\zeta'+0,\zeta') - \mu_n G_{n,n'}(\zeta'-0,\zeta') = \delta_{n,n'}/w_{n'}, \tag{B.3}$$

Here, we define the delta function $\delta(\mu_n - \mu_{n'})$, numerically as $W_{n,n'} = \delta_{n,n'}/w_{n'}$ to be used in the computations below. Using this notation, we seek solutions of (B.1) and (B.3) using plane wave solutions, as in Appendix A. Recall that $V_{j,m}$ corresponds to the jth eigenvector evaluated at μ_m, we also define $U_{j,m} = V_{-j,m}$. Similar to the form determined in (A.14), we seek solution of the form:

$$G_{m,m'}(\zeta,\zeta') = \sum_{j=1}^{N/2} v_{j,m}e^{\lambda_j(\zeta-\zeta')}a_j = V_m\mathbf{A}e^{\Lambda(\zeta-\zeta')} \quad \zeta<\zeta', \tag{B.4}$$

$$G_{m,m'}(\zeta,\zeta') = \sum_{j=1}^{N/2} u_{j,m}e^{-\lambda_j(\zeta-\zeta')}b_j = U_m e^{-\Lambda(\zeta-\zeta')}\mathbf{B} \quad \zeta>\zeta', \tag{B.5}$$

in these $\Lambda = diag(\lambda)$, which is a diagonal matrix of the eigenvalues for the range $j > 0$. In these, matrices $\mathbf{A}$ and $\mathbf{B}$ are composed of the coefficients to be determined. Note the correlation with the plane wave modes described in Appendix A,We represent the delta function in μ numerically through the respective weight associated with the appropriate abscissa. Thus, $\delta(\mu_n - \mu'_n)$ is rewritten as $\mathbf{W}^{-1}_{n,n'} = \delta_{n,n'}/w_{n'}$ which results in

$$\int_{-1}^{1} f(\mu')\delta(\mu'-\mu_n)d\mu' \approx \sum_{n=1}^{N} f(\mu_{n'})\frac{\delta_{n,n'}}{w_{n'}}w_n = f(\mu_n). \tag{B.6}$$

Upon substituting (B.4) and (B.5) into the jump condition (B.2) we obtain

$$\mathbf{M}U\mathbf{B} - \mathbf{M}V\mathbf{A} = \mathbf{W}^{-1}, \tag{B.7}$$

where $\mathbf{M} = diag(\mu)$. To solve for $\mathbf{A}$ and $\mathbf{B}$ we must simplify using the orthogonality of our eigenvectors as shown in (A.8) and (A.13). Those result in

$$U^T\mathbf{M}\mathbf{W}V = V^T\mathbf{M}\mathbf{W}U = 0, \tag{B.8}$$

and

$$V^T\mathbf{W}\mathbf{M}V = -\mathbf{I}, \quad \text{and } U^T\mathbf{W}\mathbf{M}U = I. \tag{B.9}$$

Thus, multiplying (B.7) through by $U^T\mathbf{W}$ allows us to use these relations to simplify to

$$\mathbf{B} = U^T. \tag{B.10}$$

Multiplying (B.7) through by V^TW simplifies to

$$\mathbf{A} = V^T. \tag{B.11}$$

Thus, the full Green's function is written

$$G(\zeta, \zeta') = \begin{cases} Ve^{\Lambda(\zeta-\zeta')}V^T & \zeta < \zeta', \\ Ue^{-\Lambda(\zeta-\zeta')}U^T & \zeta > \zeta'. \end{cases} \tag{B.12}$$

The half space Green's function imposes the additional boundary condition

$$G^H(\mu, 0; \mu', \zeta') = 0 \quad \text{on } 0 < \mu \leq 1. \tag{B.13}$$

We represent $G^H = G - Y$ where Y satisfies the equation

$$\mu\partial_\zeta Y + Y - \int_{-1}^{1} h(\mu, \mu')Y(\mu')d\mu' = 0, \quad \zeta > 0. \tag{B.14}$$

Subject to the boundary condition

$$Y_+(0, \zeta') - r(\mu)Y_-(0, \zeta') = G_+(0, \zeta') - r(\mu)G_-(0, \zeta') = (V_+ - r(\mu)U_+)e^{-\Lambda\zeta'}V^T. \tag{B.15}$$

In (B.15), the subscript + corresponds to the positive μ values $(0, 1]$, similarly the subscript $-$ corresponds to the negative μ values $[-1, 0)$. Using the boundary condition, we seek solutions of the form

$$Y(\zeta, \zeta') = Ue^{-\Lambda\zeta}Ce^{-\Lambda\zeta'}V^T. \tag{B.16}$$

Substituting (B.16) into (B.15) yields

$$(U_+ - r(\mu)V_+)Ce^{-\Lambda\zeta'}V^T = (V_+ - r(\mu)U_+)e^{-\Lambda\zeta'}V^T. \tag{B.17}$$

This simplifies to the relation $(U_+ - r(\mu)V_+)C = V_+ - r(\mu)U_+$ which is used to compute the coefficients in C to compute the half space Green's function

$$G^H(\zeta, \zeta') = G(\zeta, \zeta') - Ue^{-\Lambda\zeta}Ce^{-\Lambda\zeta'}V^T. \tag{B.18}$$

Note that this set of coefficients in C correspond with the c_{jk}s mentioned in (2.23). Also note the consistency with the Green's function in [33].

Bibliography

[1] George Alexandrakis, Thomas J. Farrell, and Michael S. Patterson, Accuracy of the diffusion approximation in determining the optical properties of a two-layer turbid medium, Appl. Opt., 37 (1998), pp. 7401–7409.

[2] M. Asadzadeh, The fokker-planck operator as an asymptotic limit in anisotropic media, Mathematical and Computer Modelling, 35 (2002), pp. 1119 – 1133.

[3] Andrea Bassi, Alwin Kienle, Corinna Wetzel, Daniela Comelli, Paola Taroni, and Antonio Pifferi, Determination of the optical properties of anisotropic biological media using an isotropic diffusion model, Journal of Biomedical Optics, 12 (2007), pp. 014026–014026–9.

[4] David A Boas, Dana H Brooks, Eric L Miller, Charles A DiMarzio, Misha Kilmer, Richard J Gaudette, and Quan Zhang, Imaging the body with diffuse optical tomography, Signal Processing Magazine, IEEE, 18 (2001), pp. 57–75.

[5] Stefan A. Carp, Scott A. Prahl, and Vasan Venugopalan, Radiative transport in the delta-p1 approximation: accuracy of fluence rate and optical penetration depth predictions in turbid semi-infinite media, Journal of Biomedical Optics, 9 (2004), pp. 632–647.

[6] S. Chandrasekhar, Radiative Transfer, Dover Books on Intermediate and Advanced Mathematics, Dover Publications, 1960.

[7] Hung-Wen Chang and Akira Ishimaru, Beam wave propagation and scattering in random media based on the radiative transfer theory, Journal of Wave-Material Interaction, 2(1) (1987), pp. 41–69.

[8] Wai-Fung Cheong, Scott A Prahl, Ashley J Welch, et al., A review of the optical properties of biological tissues, IEEE journal of quantum electronics, 26 (1990), pp. 2166–2185.

[9] T. Collier, D. Arifler, A. Malpica, M. Follen, and R. Richards-Kortum, Determination of epithelial tissue scattering coefficient using confocal microscopy, Selected Topics in Quantum Electronics, IEEE Journal of, 9 (2003), pp. 307–313.

[10] Ramzi S. Cotran, Stanley L. Robbins, and Vinay Kumar, Robbins Pathological Basis of Disease, Philadelphia, PA: W. B. Saunders, 1994.

[11] Andrew Dunn and David Boas, Transport-based image reconstruction in turbid media with small source—detector separations, Opt. Lett., 25 (2000), pp. 1777–1779.

[12] Rachid Elaloufi, Simon Arridge, Romain Pierrat, and Rémi Carminati, Light propagation in multilayered scattering media beyond the diffusive regime, Appl. Opt., 46 (2007), pp. 2528–2539.

[13] Thomas J. Farrell, Michael S. Patterson, and Brian Wilson, A diffusion theory model of spatially resolved, steadystate diffuse reflectance for the noninvasive determination of tissue optical properties invivo, Medical Physics, 19 (1992), pp. 879–888.

[14] Maria Angela Franceschini, Sergio Fantini, L. Adelina Paunescu, John S. Maier, and Enrico Gratton, Influence of a superficial layer in the quantitative spectroscopic study of strongly scattering media, Appl. Opt., 37 (1998), pp. 7447–7458.

[15] Adam R. Gardner, Arnold D. Kim, and Vasan Venugopalan, Radiative transport produced by oblique illumination of turbid media with collimated beams, Phys. Rev. E, 87 (2013), p. 063308.

[16] Pedro González-Rodríguez and Arnold D. Kim, Light propagation in tissues with forward-peaked and large-angle scattering, Appl. Opt., 47 (2008), pp. 2599–2609.

[17] ——, Comparison of light scattering models for diffuse optical tomography, Opt. Express, 17 (2009), pp. 8756–8774.

[18] Pedro González-Rodríguez and Arnold D Kim, Reflectance optical tomography in epithelial tissues, Inverse problems, 25 (2009), p. 015001.

[19] R. A. J. Groenhuis, H. A. Ferwerda, and J. J. Ten Bosch, Scattering and absorption of turbid materials determined from reflection measurements. 1: Theory, Appl. Opt., 22 (1983), pp. 2456–2462.

[20] Carole K. Hayakawa, Brian Y. Hill, Joon S. You, Frédéric Bevilacqua, Jerome Spanier, and Vasan Venugopalan, Use of the δ-p1 approximation for recovery of optical absorption, scattering, and asymmetry coefficients in turbid media, Appl. Opt., 43 (2004), pp. 4677–4684.

[21] Jenni Heino, Simon Arridge, Jan Sikora, and Erkki Somersalo, Anisotropic effects in highly scattering media, Phys. Rev. E, 68 (2003), p. 031908.

[22] R. Hornung, T.H. Pham, K.A. Keefe, M.W. Berns, Y. Tadir, and B.J. Tromberg, Quantitative near-infrared spectroscopy of cervical dysplasia in vivo, Human Reproduction, 14 (1999), pp. 2908–2916.

[23] A. Ishimaru, Wave Propagation and Scattering in Random Media, An IEEE OUP classic reissue, Wiley, 1999.

[24] Steven L Jacques, Optical properties of biological tissues: a review, Physics in Medicine and Biology, 58 (2013), p. R37.

[25] J H_ Joseph, WJ Wiscombe, and JA Weinman, The delta-eddington approximation for radiative flux transfer, Journal of the Atmospheric Sciences, 33 (1976), pp. 2452–2459.

[26] Alwin Kienle, Lothar Lilge, Michael S. Patterson, Raimund Hibst, Rudolf Steiner, and Brian C. Wilson, Spatially resolved absolute diffuse reflectance measurements fornoninvasive determination of the optical scattering and absorption coefficientsof biological tissue, Appl. Opt., 35 (1996), pp. 2304–2314.

[27] Alwin Kienle and Michael S Patterson, Determination of the optical properties of turbid media from a single monte carlo simulation, Physics in Medicine and Biology, 41 (1996), p. 2221.

[28] ——, Determination of the optical properties of semi-infinite turbid media from frequency-domain reflectance close to the source, Physics in Medicine and Biology, 42 (1997), p. 1801.

[29] Alwin Kienle and Michael S. Patterson, Improved solutions of the steady-state and the time-resolved diffusion equations for reflectance from a semi-infinite turbid medium, J. Opt. Soc. Am. A, 14 (1997), pp. 246–254.

[30] Alwin Kienle, Michael S. Patterson, Nora Dögnitz, Roland Bays, Georges Wagnieres, and Hubert van den Bergh, Noninvasive determination of the optical properties of two-layered turbid media, Appl. Opt., 37 (1998), pp. 779–791.

[31] A. Kim, A boundary integral method to compute green's functions for the radiative transport equation, Waves in Random and Complex Media, 15 (2005), pp. 17–42.

[32] Arnold D. Kim, Transport theory for light propagation in biological tissue, J. Opt. Soc. Am. A, 21 (2004), pp. 820–827.

[33] ——, Correcting the diffusion approximation at the boundary, J. Opt. Soc. Am. A, 28 (2011), pp. 1007–1015.

[34] Arnold D. Kim, Carole Hayakawa, and Vasan Venugopalan, Estimating optical properties in layered tissues by use of the born approximation of the radiative transport equation, Opt. Lett., 31 (2006), pp. 1088–1090.

[35] Arnold D. Kim and Joseph B. Keller, Light propagation in biological tissue, J. Opt. Soc. Am. A, 20 (2003), pp. 92–98.

[36] Arnold D. Kim and Miguel Moscoso, Radiative transfer computations for optical beams, Journal of Computational Physics, 185 (2003), pp. 50 – 60.

[37] ——, Backscattering of beams by forward-peaked scattering media, Opt. Lett., 29 (2004), pp. 74–76.

[38] ——, Beam propagation in sharply peaked forward scattering media, J. Opt. Soc. Am. A, 21 (2004), pp. 797–803.

[39] Arnold D. Kim and Miguel Moscoso, Light transport in two-layer tissues, Journal of Biomedical Optics, 10 (2005), pp. 034015–034015–10.

[40] Arnold D. Kim and John C. Schotland, Self-consistent scattering theory for the radiative transport equation, J. Opt. Soc. Am. A, 23 (2006), pp. 596–602.

[41] Young L. Kim, Yang Liu, R.K. Wali, Hemant K. Roy, M.J. Goldberg, A.K. Kromin, Kun Chen, and Vadim Backman, Simultaneous measurement of angular and spectral properties of light scattering for characterization of tissue microarchitecture and its alteration in early precancer, Selected Topics in Quantum Electronics, IEEE Journal of, 9 (2003), pp. 243–256.

[42] Cemre Kortun, Yasser R. Hijazi, and Dizem Arifler, Combined monte carlo and finite-difference time-domain modeling for biophotonic analysis: implications on reflectance-based diagnosis of epithelial precancer, Journal of Biomedical Optics, 13 (2008), pp. 034014–034014–14.

[43] Ossi Lehtikangas, Tanja Tarvainen, and Arnold D. Kim, Modeling boundary measurements of scattered light using the corrected diffusion approximation, Biomed. Opt. Express, 3 (2012), pp. 552–571.

[44] Shao-Pow Lin, Lihong Wang, Steven L. Jacques, and Frank K. Tittel, Measurement of tissue optical properties by the use of oblique-incidence optical fiber reflectometry, Appl. Opt., 36 (1997), pp. 136–143.

[45] Guillermo Marquez and Lihong V. Wang, White light oblique incidence reflectometer for measuring absorption and reduced scattering spectra of tissue-like turbid media, in Biomedical Optical Spectroscopy and Diagnostics / Therapeutic Laser Applications, Optical Society of America, 1998, p. BMA3.

[46] Michele Martinelli, Adam Gardner, David Cuccia, Carole Hayakawa, Jerome Spanier, and Vasan Venugopalan, Analysis of single monte carlo methods for prediction of reflectance from turbid media, Opt. Express, 19 (2011), pp. 19627–19642.

[47] Cornelis J. Van Noorden, Linda Meade-Tollin, and Fred Bosman, Metastasis, American Scientist, 86(2) (1998), p. 130.

[48] G.C. Pomraning, Near-infinite-medium solutions of the equation of transfer, Journal of Quantitative Spectroscopy and Radiative Transfer, 44 (1990), pp. 317 – 338.

[49] Scott A. Prahl, Martin J. C. van Gemert, and Ashley J. Welch, Determining the optical properties of turbid media by using the adding–doubling method, Appl. Opt., 32 (1993), pp. 559–568.

[50] L. O. Reynolds and N. J. McCormick, Approximate two-parameter phase function for light scattering, J. Opt. Soc. Am., 70 (1980), pp. 1206–1212.

[51] Jorge Ripoll, Derivation of the scalar radiative transfer equation from energy conservation of maxwell's equations in the far field, J. Opt. Soc. Am. A, 28 (2011), pp. 1765–1775.

[52] Shelley B. Rohde and Arnold D. Kim, Modeling the diffuse reflectance due to a narrow beam incident on a turbid medium, J. Opt. Soc. Am. A, 29 (2012), pp. 231–238.

[53] S. B. Rohde and A. D. Kim, Convolution model of the diffuse reflectance for layered tissues, Opt. Lett., 39 (2014), pp. 154–157.

[54] J. M. Schmitt, R. T. Wall, G. X. Zhou, and E. C. Walker, Multilayer model of photon diffusion in skin, J. Opt. Soc. Am. A, 7 (1990), pp. 2141–2153.

[55] InSeok Seo, Carole K. Hayakawa, and Vasan Venugopalan, Radiative transport in the delta-p1 approximation for semi-infinite turbid media, Medical Physics, 35 (2008), pp. 681–693.

[56] A. E. Siegman, Quasi fast hankel transform, Opt. Lett., 1 (1977), pp. 13–15.

[57] American Cancer Society, Imaging (radiology) tests. ACS website article on Imaging Radiology Tests.

[58] ——, Cancer facts & figures 2013, Atlanta: American Cancer Society, 2013.

[59] T. Tarvainen, M. Vauhkonen, V. Kolehmainen, and J. P. Kaipio, Finite element model for the coupled radiative transfer equation and diffusion approximation, International Journal for Numerical Methods in Engineering, 65 (2006), pp. 383–405.

[60] Sheng-Hao Tseng, C.K. Hayakawa, H. Spanier, and Anthony J. Durkin, Determination of optical properties of superficial volumes of layered tissue phantoms, Biomedical Engineering, IEEE Transactions on, 55 (2008), pp. 335–339.

[61] H. C. van de Hulst, Light Scattering by Small Particles, Dover Publications, Inc., 1st ed., 1981.

[62] M. C. W. van Rossum and Th. M. Nieuwenhuizen, Multiple scattering of classical waves: microscopy, mesoscopy, and diffusion, Rev. Mod. Phys., 71 (1999), pp. 313–371.

[63] V. Venugopalan, J. S. You, and B. J. Tromberg, Radiative transport in the diffusion approximation: An extension for highly absorbing media and small source-detector separations, Phys. Rev. E, 58 (1998), pp. 2395–2407.

[64] Edward Vitkin, Vladimir Turzhitsky, Le Qiu, Lianyu Guo, Irving Itzkan, Eugene B. Hanlon, and Lev T. Perelman, Photon diffusion near the point–of–entry in anisotropically scattering turbid media, Nat. Commun., 2 (2011), p. 587.

[65] Lihong Wang and Steven L. Jacques, Hybrid model of monte carlo simulation and diffusion theory for light reflectance by turbid media, J. Opt. Soc. Am. A, 10 (1993), pp. 1746–1752.

[66] ——, Use of a laser beam with an oblique angle of incidence to measure the reduced scattering coefficient of a turbid medium, Appl. Opt., 34 (1995), pp. 2362–2366.

[67] Lihong V. Wang, Rapid modeling of diffuse reflectance of light in turbid slabs, J. Opt. Soc. Am. A, 15 (1998), pp. 936–944.

[68] Lihong V. Wang and Hsin-I Wu, Biomedical Optics: Principles and Imaging, Wiley, 2007.

[69] Scott A. Prahl; A. J. Welch and M. J. C. van Gemert, Optical-Thermal Response of Laser-Irradiated Tissue: The diffusion approximation in three dimensions, Plenum, New York, 1995, ch. 5, pp. 207–231.

[70] S. A. Prahl; A. J. Welch and M. J. C. van Gemert, Optical-Thermal Response of Laser-Irradiated Tissue: The diffusion approximation in three dimensions, Plenum, New York, 1995, ch. 7, pp. 207–231.

[71] Willem M. Star; A. J. Welch and M. J. C. van Gemert, Optical-Thermal Response of Laser-Irradiated Tissue: The diffusion approximation in three dimensions, Plenum, New York, 1995, ch. 6, pp. 145–201.

[72] Gilwon Yoon, Scott A. Prahl, and Ashley J. Welch, Accuracies of the diffusion approximation and its similarity relations for laser irradiated biological media, Appl. Opt., 28 (1989), pp. 2250–2255.

[73] J. S. You, C. K. Hayakawa, and V. Venugopalan, Frequency domain photon migration in the $\delta - p1$ approximation: Analysis of ballistic, transport, and diffuse regimes, Phys. Rev. E, 72 (2005), p. 021903.

[74] Roger J. Zemp, Phase-function corrected diffusion model for diffuse reflectance of a pencil beam obliquely incident on a semi-infinite turbid medium, Journal of Biomedical Optics, 18 (2013), pp. 067005–067005.

[75] George Zonios and Aikaterini Dimou, Modeling diffuse reflectance from semi-infinite turbid media: application to the study of skin optical properties, Opt. Express, 14 (2006), pp. 8661–8674.

[76] ——, Modeling diffuse reflectance from homogeneous semi-infinite turbid media for biological tissue applications: a monte carlo study, Biomed. Opt. Express, 2 (2011), pp. 3284–3294.